UC Berkeley
UC Berkeley Electronic Theses and Dissertations

Title

Quantum light-matter interactions in metasurface and two-dimensional materials

Permalink

https://escholarship.org/uc/item/8mg443tf

Author

Li, Quanwei

Publication Date

2019

Peer reviewed|Thesis/dissertation

eScholarship.org Powered by the California Digital Library
University of California

Quantum light-matter interactions in metasurface and two-dimensional materials

By

Quanwei Li

A dissertation submitted in partial satisfaction of the
requirements for the degree of
Doctor of Philosophy
in
Applied Science and Technology
and the
Designated Emphasis
in
Nanoscale Science and Engineering
in the
Graduate Division
of
University of California, Berkeley

Committee in charge:

Professor Xiang Zhang, Chair
Professor Jie Yao
Professor Feng Wang
Professor Jeffrey Neaton

Fall 2019

Quantum light-matter interactions in metasurface and two-dimensional materials

Copyright 2019

by

Quanwei Li

All Rights Reserved

Abstract

Quantum light-matter interactions in metasurface and two-dimensional materials

by

Quanwei Li

Doctor of Philosophy in Applied Science and Technology

with the Designated Emphasis in Nanoscale Science and Engineering

University of California, Berkeley

Professor Xiang Zhang, Chair

Light-matter interactions critically exist in our life, ranging from photosynthesis to the optical high-speed Internet and datacenters. The quantum nature of light and its interactions with matter not only provide us the fundamental understanding of the subject but also enable the revolutionary fields of quantum information science and technologies. In this dissertation, I present our study of quantum light-matter interactions in emergent two-dimensional platforms such as van der Waals materials and nano-structured metasurface. The demonstrated novel physics and unprecedented control capability expand our knowledge on light-matter interactions and promise future applications in quantum communication and quantum computation.

The dissertation consists of three parts. The first part investigates quantum single-photon emission from color centers in van der Waals hexagonal boron nitride. We characterize those superb single-photon emitters and demonstrate the giant Stark effect of photon energy at room temperature. The surprisingly large 31 meV Stark shift is achieved by applying huge in-plane electric fields on scale of 0.1 V/nm. Moreover, we report, for the first time, the angle-resolved Stark effect in solid-state single-photon emitters by rotating the field direction. A permanent electric dipole is uncovered, which unveils that both inversion and three-fold rotation symmetries are broken at the color center. The remarkable giant Stark effect and the significant structural information of the color center pave a way towards the scalable solid-state quantum technologies at room temperature.

The second part focuses on nonlinear optics at excited states of exciton polaritons, the partial-light partial-matter quantum quasiparticles, in microcavity containing monolayer WS_2. We directly probe the excited states of exciton polaritons by utilizing valley sensitive nonlinear selection rules. Specifically, we unravel the valley-dependent dark 2p excited states by resonant two-photon luminescence excitation spectroscopy. Moreover, we look into the dynamically unstable upper polariton band by the instantaneous second harmonic generation spectroscopy. Our study of the excited states of exciton polaritons in two dimensional materials clears the way for room-temperature valley polariton condensation and full control of these polaritons for quantum applications.

The third part is on steering quantum photon-photon interaction mediated by two-dimensional metasurface. We, for the first time, propose and experimentally demonstrate that the rotation of metasurface enables a new degree of freedom in optical quantum interference through its unique anisotropic phase responses. Specifically, we show that the output of two-photon interference can be dynamically tuned to be bunching state, split state, or their arbitrary intermediate state, by simply rotating the metasurface. Consequently, the effective photon-photon interaction at metasurface beam-splitter can be manipulated continuously from attractive to repulsive. Our metasurface opens a door for both fundamental quantum photon-photon interaction and the development of innovative quantum gates, algorithms and computing models.

Dedicated to my family

Table of contents

List of figures

List of tables

Acknowledgement

First of all, I must express my deepest gratitude to my advisor Prof. Xiang Zhang for his full support to my Ph.D. study. His enthusiasm and perseverance to novelty sharpen my vision. His philosophies of thinking, approaching and presenting science show me what a world-top scientist is like. Additionally, Prof. Zhang has founded one of the most vibrant and creative research groups in the world. He brings together top talents with diverse expertise and provides us the energy and resource to freely interact with each other. I am very lucky to join the group. The years here have transformed me from a naive graduate student to a solid experimentalist and mature scholar.

I would like to thank Dr. Yuan Wang and Dr. Sui Yang for their significant help in my research as the group managers. I also appreciate the valuable guidance from all my past research mentors – Dr. Ziliang Ye, Dr. Kevin O'Brien and Dr. Wei Bao. Besides, I am more than grateful to those who I have closely collaborated with in the group – Dr. Wei Bao, Dr. Yang Xia, Dr. Xiaoze Liu, Dr. Ting-Fung Chung – as well as those who I have worked with -- Dr. Cheng Gong, Dr. Jun Yi, Mr. Zhaoyu Nie, Dr. Jeongmin Kim, Dr. Yahui Xue, Dr. King Yan Fong, Dr. Haokun Li, Mr. Renjie Tao, Dr. Peiyao Zhang, Dr. Pasquale Cilibrizzi, Dr. Kevin O'Brien, Dr. Pankaj Jha, Dr. Yu Ye, Dr. Ziliang Ye, Dr. Hanyu Zhu, Dr. Mervin Zhao, Dr. Jun Xiao, Dr. Ying Wang, Dr. Xuexin Ren and Mr. Siqi Wang. What is more, I would like to thank all the current and past members of Xlab for creating the vigorous research environment.

I am also truly thankful to Prof. David Attwood, Prof. Roger Falcone, Prof. Jeffrey Neaton, Prof. Feng Wang and Prof. Jie Yao for their time and advice in my prelim/qualifying/dissertation committee. Their comments and suggestions are really helpful.

Moreover, I would like to thank all my friends at Berkeley for their indispensable company and encouragement.

Last but not least, I must thank my family and my girlfriend for their wholehearted love and support.

1 Introduction

1.1 Introduction and motivation

Light-matter interaction plays an indispensable role in our life. For example, harvesting sun light in photosynthesis produces the ultimate food for most life on the earth, and capturing visible light in our eyes contributes most of the information we perceive. The study of light-matter interaction has been a fruitful journey throughout the history of human civilization. Today, engineering of light-matter interaction has created life-changing technologies such as fluorescent/LED lighting, display devices, digital cameras, solar cells and optical high-speed Internet/datacenter.

Quantum physics reveals that light consists of elementary quantum particles called photons. The quantum interaction between single photon and single atom elucidates the ultimate microscopic mechanism of light-matter interaction (*1*). Significantly, this also empowers the groundbreaking fields of quantum information science and technologies (QISTs) (*2*). Essentially, QISTs store, transmit and process quantum information carried by quantum bits (qubits), which are quantum two-level systems, such as photon polarization and electron spin. QISTs guarantee absolutely secure communication by utilizing the delicate qubits to transport information and promise exponential speedup computation by exploiting the massively parallel quantum superposition of interacting qubits. Qubits made of visible/near-infrared photons have pioneered the early works in QISTs and have been one of the leading platforms ever since. This is because the distinct advantages of photons such as long coherence time, low loss propagation, room-temperature operation, easy single qubit operation and light speed signal transmission.

In quantum communications, photons are the only favorable information carriers (*3*) and single photons are critically required for many important protocols. For example, the seminal BB84 protocol (*4*) encodes information in the non-orthogonal polarization states of single photons, in which absolute security is provable because any attempt to steal information would leave noticeable disturbance in the quantum states of those single photons. However, practical applications of the BB84 protocol has been impeded by the lack of ideal single-photon sources.

In quantum computation involving photons, controlling the quantum light-matter interaction between photon qubits and matter qubits is the central task. Particularly, the interaction usually needs to enter the so-called strong coupling regime for coherent transfer of quantum information, such as in quantum networks (*5*). Achieving strong coupling, however, is challenging because the interaction becomes increasingly weak as photon number or atom number decreases, partially due to the size mismatch between photon and atom.

In optical quantum computation that only uses photon qubits, controlling the interaction between single photons is the key (*6*). Since photons intrinsically do not interact with each other, an effective interaction must be constructed to perform two-qubit operations. As pointed out in the linear optical quantum computing model (*7*), an effective photon-photon interaction can be introduced by quantum interference at a beam-splitter. However, control of such interaction at conventional beam-splitter has been very limited.

To develop those vital ingredients, tremendous efforts have been devoted for decades in three closely related sub-fields: solid-state single-photon emitters (*8*), cavity quantum electrodynamics (*9*) and quantum photonics (*10*). Regardless of the remarkable advantages of photons and all the progress, however, the three severe challenges remain and hinder the applications of optical quantum technologies. They are 1) the lack of perfect single-photon emitters, 2) the generally weak photon-matter interaction and 3) the absence of intrinsic photon-photon interaction.

This dissertation represents our continued endeavor towards tackling those challenges. We report the investigation and manipulation of quantum light-matter interaction in emergent platforms such as two-dimensional insulating and semiconducting van der Waals materials and two-dimensional nano-structured metasurfaces. The demonstrated novel physics and unprecedented control capability deepen our understanding of quantum light-matter interaction and herald future applications in quantum communication and quantum computation.

1.2 Dissertation overview

The dissertation consists of three parts to address the challenges in quantum light-matter interaction for optical QISTs. 1, Single-photon emission from hBN color center and its room-temperature giant Stark effect; 2, Nonlinear optics at the excited states of exciton polariton in monolayer WS_2; and 3, Steering optical quantum interference for effective photon-photon interaction by metasurface beam-splitter.

Chapter 2 is devoted to single-photon emission in hBN. we start with introducing the physics of single photons and present the material preparation and various optical characterizations of the single-photon emitters. We conclude the chapter by comparing hBN emitters to other emitters and discussing the approaches to overcome the limitations of solid-state emitters in general. Following that, we report our achievement on addressing the limitation of inhomogeneous emission by Stark effect in Chapter 3. After introducing the physics and device implementation of Stark effect, we show our results on room-temperature giant Stark effect and its application for single-photon wavelength modulation. We then discuss the dependence of Stark shift on temperature and electrical field direction. From the angle-resolved Stark effect, a permanent electric dipole moment is discovered that tells information on the emitter structure.

Chapter 4 is focused on nonlinear optics of exciton polaritons in microcavity containing monolayer WS_2. We begin with introducing the concepts of exciton polaritons and the valley degree of freedom in single layer transition metal dichalcogenide. Following that are the descriptions of the experiment design and sample fabrication. We verify the strong coupling regime and formation of exciton polariton by linear spectroscopies of reflection and photoluminescence. With that, we proceed to show our results on the nonlinear valley-polarized two-photon excitation fluorescence and its resonance on the excited 2p states. Then the instantaneous second harmonic generation is demonstrated at resonance with the upper polariton band. Experimental results at various temperatures are also discussed along the way.

Chapter 5 is concentrated on the theory and design of metasurface for manipulating quantum photon-photon interaction through two-photon interference. We introduce the underlying physics of two-particle interference at convention beam-splitter and its limitations. After that we show how a uniquely designed metasurface beam-splitter with anisotropic phase response can enable a new degree of freedom in two-photon interference by its mechanical rotation. Our experimental demonstrations are reported in Chapter 6, beginning with describing the fabrication of the metasurface. A versatile interferometer and a two-photon source are designed and built to characterize the metasurface and perform the two-photon interference experiments. We achieve the desirable rotation degree of freedom in optical quantum interference that manipulate the effective photon-photon interaction arbitrarily from attractive to repulsive.

2 Single-photon emitter in hBN

2.1 Introduction

Single photons are quanta of light, a non-classical quantum mechanical state. The concept of light quanta, first introduced by Planck in 1900 in his seminal work explaining the blackbody radiation problem, marked the beginning of the quantum revolution in science and human civilization. Ever since then, photons have been in the central of quantum physics and now the central and frontier of quantum technologies. That is because qubit, quantum bit of information, made of photon has a number of distinct advantages such as long coherence time, room-temperature operation, easy single-qubit control and light speed propagation. As such, single-photon emitters are critical building blocks needed for quantum science and technology (*11*). For practical applications, room-temperature solid-state platforms are required (*3*, *8*).

Despite its vital importance, an ideal single-photon emitter is still missing, which is one of the major challenges for quantum technologies. Two-dimensional van der Waals (vdW) materials are promising candidates to tackle this challenge. vdW materials, ranging from semi-metallic graphene (*12*) and semiconducting transition metal dichalcogenides (*13*) to insulating hexagonal boron nitride (hBN), possess exceptional electronic and optical properties. They have enabled remarkable scientific and technological breakthroughs in the last two decades. Both the single materials and the heterostructures have been exploited to demonstrate appealing device applications (*14*), such as light emitting diodes (*15*), lasers (*16*) and optical modulators (*17*). While most studies and applications deal with classical information, a few experiments have been reported in the quantum regime at liquid helium temperature (*18*–*23*).

Recently, color centers in hBN emerge as superb room-temperature solid-state single photon emitters (SPE) (*24*), which opens up the possibilities of utilizing vdW materials as a platform for room-temperature solid-state quantum information systems. They are capable to work at room temperature, and among the brightest SPEs due to its high internal quantum efficiency, and easy photon extraction as a result of the layered material structure (*24*). Consequently, millions of linearly polarized photons per second can be detected without additional photon extraction structures. Furthermore, such layered vdW materials can be integrated with other photonic and electrical components (*13*, *14*, *25*), highly preferred for integrated on-chip quantum information systems.

In this chapter, we first introduce the concept of single photons and then discuss the single-photon emitters in hBN and their properties. Although among the best, like all the other solid-state emitters, single-photon emitters in hBN have major problems such as inhomogeneous emission wavelength. In next chapter, we will control the emission wavelength via the Stark effect.

2.2 The concept of single photons

A single quantum of light is called a photon. Alike matters are composed of the smallest unit of atoms, light is composed of the smallest unit of photons.

In the standard formulism following Dirac, photons can be obtained by second quantization of classical electromagnetic waves (*1*, *26*). Essentially, this is done by recognizing the energy of single-mode electromagnetic fields in vacuum in the form of

$$H = \frac{1}{2}\int dV\,(\varepsilon_0 E^2 + \frac{1}{\mu_0}B^2), \tag{2.2.1}$$

where H is the energy or Hamiltonian of the classical electromagnetic fields, E (B) the electric (magnetic) fields, ε_0 (μ_0) the vacuum permittivity (permeability) and V the spatial volume, can be mapped to

$$\hat{H} = \frac{1}{2}(\omega^2\hat{q}^2 + \hat{p}^2), \tag{2.2.2}$$

where $\hat{H}$ is the Hamiltonian operator, ω the angular frequency and $\hat{q}$ $(\hat{p})$ the canonical position (momentum) operator, by the correspondence of

$$E \rightarrow \hat{q} = \sqrt{\hbar/(2\omega)}(a^\dagger + a), \tag{2.2.3}$$

and

$$B \rightarrow \hat{p} = i\sqrt{\hbar\omega/2}(a^\dagger - a), \tag{2.2.4}$$

where $\hbar$ is the Planck constant and $a^\dagger$ (a) the creation (annihilation) operator.

Now single mode electromagnetic fields are transformed into a harmonic oscillator with equally spaced energy levels,

$$\hat{H} = \hbar\omega\left(\hat{n} + \frac{1}{2}\right), \tag{2.2.5}$$

where $\hat{n} = a^\dagger a$ is the number operator. The difference between two level is

$$\Delta H = \hbar\omega, \tag{2.2.6}$$

the energy quantum corresponding to a single photon. Thus, the energy levels are also the population of photon number. Figure 2.2.1 below illustrates such transformation.

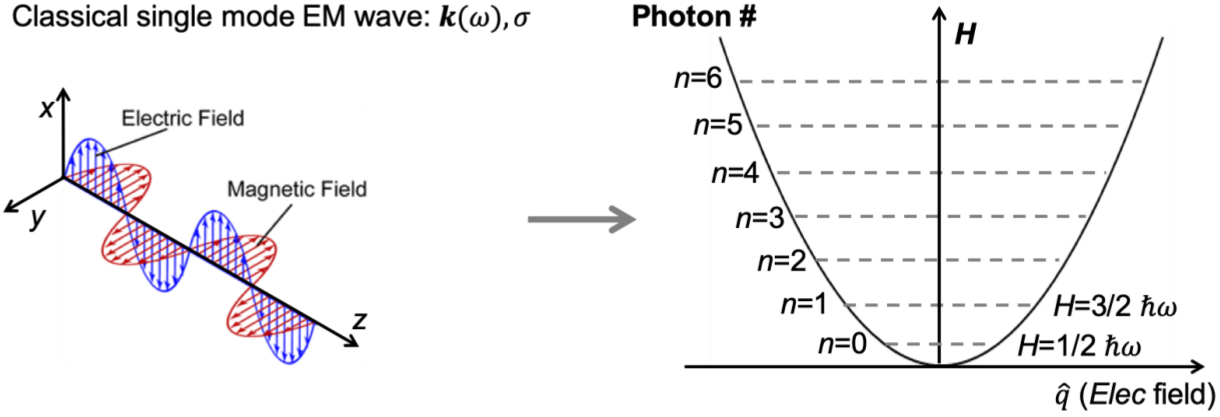

Figure 2.2.1 | Quantization of the electromagnetic fields. $\boldsymbol{k}$ the wave vector, σ wave polarization.

2.3 Photon statistics

Photon statistics classifies the statistical properties of photon steam in a light beam. Quantum light states, such as single photons, exhibit different statistics from classical light states, such as laser beam or thermal light. Therefore, measurement of photon statistics is a way to reveal the quantum nature of light.

Suppose we are measuring the light intensity, or equivalently the photon flux, of a light beam from a steady source with a prefect detector (unit detection efficiency and infinite timing resolution) as a function of time, as shown in the Figure 2.3.1A below. Assume all the light beams have same average intensity, but we may obverse different levels of intensity fluctuation over time depending on the type of the source (Figure 2.3.1B). Specifically, the thermal source will produce the largest fluctuation (blue curve in Figure 2.3.1B), while a laser source less fluctuation (green curve in Figure 2.3.1B) and a perfect single photon source no fluctuation at all (red curve in Figure 2.3.1B). To explain the difference in fluctuation, we zoom in to illustrate the photon steam in each case in Figure 2.3.1C. The photons from thermal source trends to arrive in clusters, while photons from laser source (i.e. coherent state $|\boldsymbol{\alpha}\rangle$) arrive totally random and photons from single photon source are equally spaced in time. We can plot the probability distribution of photon number in a given time interval for those three cases (Figure 2.3.1D). The time interval is chosen such that the average photon number in it is one. The distribution of laser light follows what is called the Poisson distribution, while the thermal light can be refereed as super-Poisson because the distribution spreads more broadly. Both Poisson and super-Poisson distribution are allowed in classical theory of light. In stark contrast, the distribution of single photon is a delta-like function peaked at one photon number, as straightforward from its definition and the illustration in Figure 2.3.1C. This is the extreme case of the so-called sub-Poisson distribution as the distribution spreads narrower than Poisson. Sub-Poisson distribution is impossible in classical theory but allowed in quantum theory, therefore it is a signature of quantum state of light.

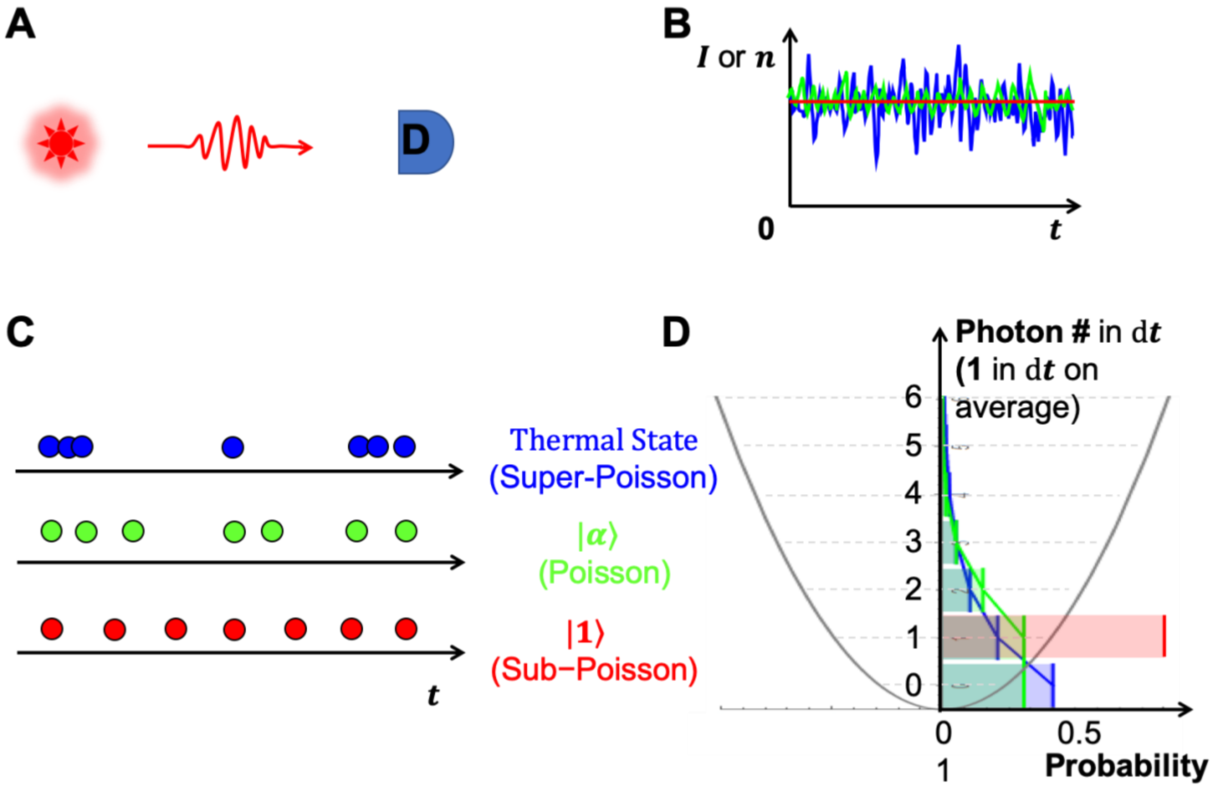

Figure 2.3.1 | Photon statistics of thermal, coherent and single-photon states of light.

Ideally, we can just measure the photon number distribution of a light beam to tell the photon statistics, as illustrated in Figure 2.3.1 above. Practically, we may not have such a perfect detector that can resolve the photon numbers. An alternative way is to measure the so called second order coherence function $g^{(2)}(\tau)$ through a Harry Brown and Twiss type intensity interferometer as shown in the Figure 2.3.2 below. For a single-mode field,

$$g^{(2)}(\tau) = g^{(2)}(0) = \frac{\langle a^{\dagger} a^{\dagger} a a \rangle}{\langle a^{\dagger} a \rangle^2} = \frac{\langle n(n-1) \rangle}{\langle n \rangle^2} = 1 + \frac{\langle (\Delta n)^2 \rangle - \langle n \rangle}{\langle n \rangle^2}. \tag{2.3.1}$$

Basically, the light beam is spited to two parts by a 50:50 beam-splitter and directed to two detectors. The normalized coincident count $g^{(2)}(\tau)$ is measured as a function of the time delay τ between the signals from the two detectors. At zero-time delay, $g^{(2)}(0)$ of single photon drops to zero because there is only one photon, which can only reach one of the detectors but not both. At time delay greater than the characteristic time scale τ_c (for example the lifetime of single photon emitter), coincidence from successive photons can happen and the $g^{(2)}(\tau)$ will reach a baseline plateau. In this case, $\Delta n = 0 < \sqrt{\langle n \rangle}$ and $g^{(2)}(0) < g^{(2)}(\tau)$, which is called antibunching, meaning there is a less probability of finding more than one photon as the time delay approaching zero. For laser light, $\Delta n = \sqrt{\langle n \rangle}$ and $g^{(2)}(\tau)$ remains flat curve, meaning the probability of finding two photons is independent of time delay. For thermal light, , $\Delta n = \sqrt{\langle n \rangle + \langle n \rangle^2} > \sqrt{\langle n \rangle}$ and $g^{(2)}(0)$ reaches double the baseline and it is called bunching as $g^{(2)}(0) > g^{(2)}(\tau)$, meaning a greater probability of detecting a second photon given a first photon detection.

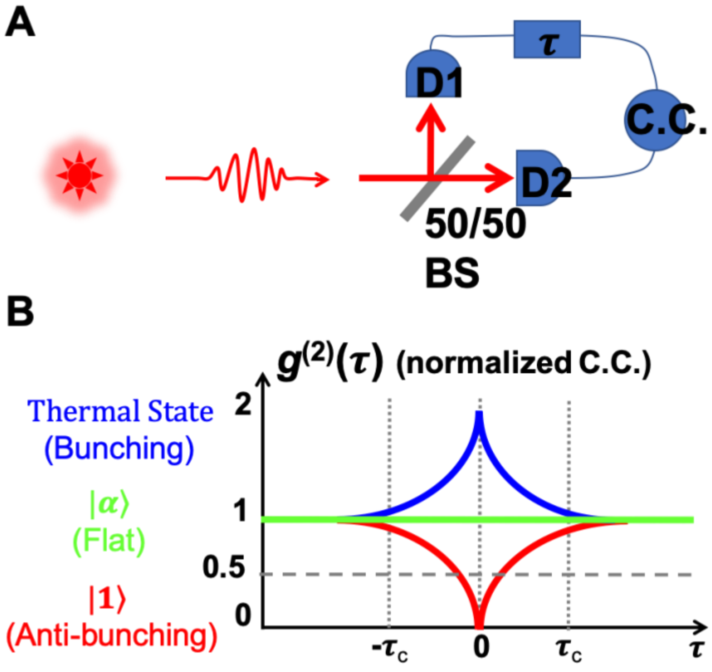

Figure 2.3.2 | The Harry Brown and Twiss intensity interferometer and the second order coherence function $g^{(2)}(\tau)$.

2.4 Room-temperature single-photon emitters in hBN

Hexagonal boron nitride (hBN) is a two-dimensional van der Waals insulator with large band gap (~ 6 eV). Figure 2.4.1 below shows the atomic structure of a monolayer hBN.

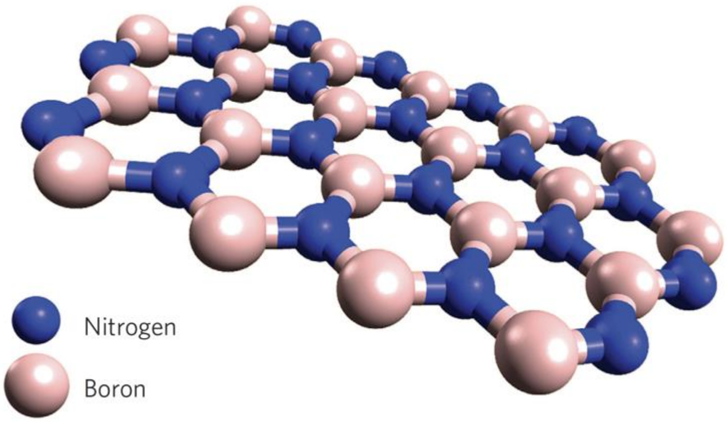

Figure 2.4.1 | Atomic structure of monolayer hBN. Adopted from Ref. (*24*).

Atomic defects, or color centers, in the band gap of hBN can be single photon emitters. The emitters density and quality vary a lot across different sources of hBN crystals. Although single-photon emission from all nano-flakes, chemical-vapor-deposition (CVD) thin films and bulk hBN crystals are observed and reported (*24*, *27*), so far, the emitters in nano-flakes produce the best quality single photons.

The hBN nanoflakes are purchased from Graphene Supermarket, in the form of a liquid suspension and drop-cast on silicon substrate with ~ 280 nm thermal oxide on top. The samples are then annealed at 1000 C for 30 min in an Ar/H_2 environment followed by slow cooling down.

Figure 2.4.2 below shows the scanning electron microscope (SEM) image of a few hBN nano-flakes on a holy transmission electron microscope (TEM) grid, revealing the morphology. Figure 2.4.3 below shows the distribution of thickness and lateral size of 68 hBN nanoflakes, as measured by atomic force microscope (AFM). Their typical thickness ranges from tens of to more than one hundred nanometers, and their lateral sizes are typically from tens of to a few hundred nanometers.

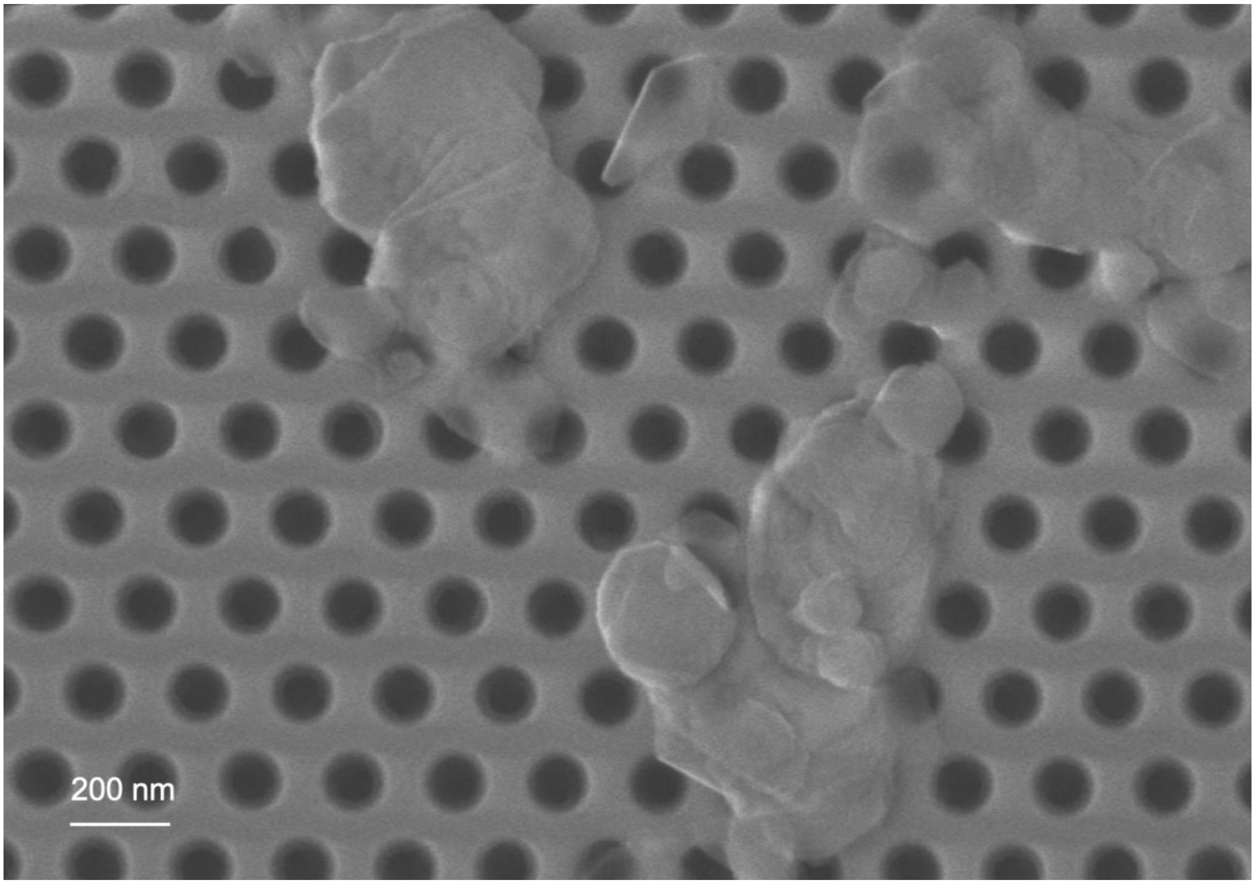

Figure 2.4.2 | Scanning electron microscope (SEM) image of a few hBN nano-flakes on a holy TEM grid.

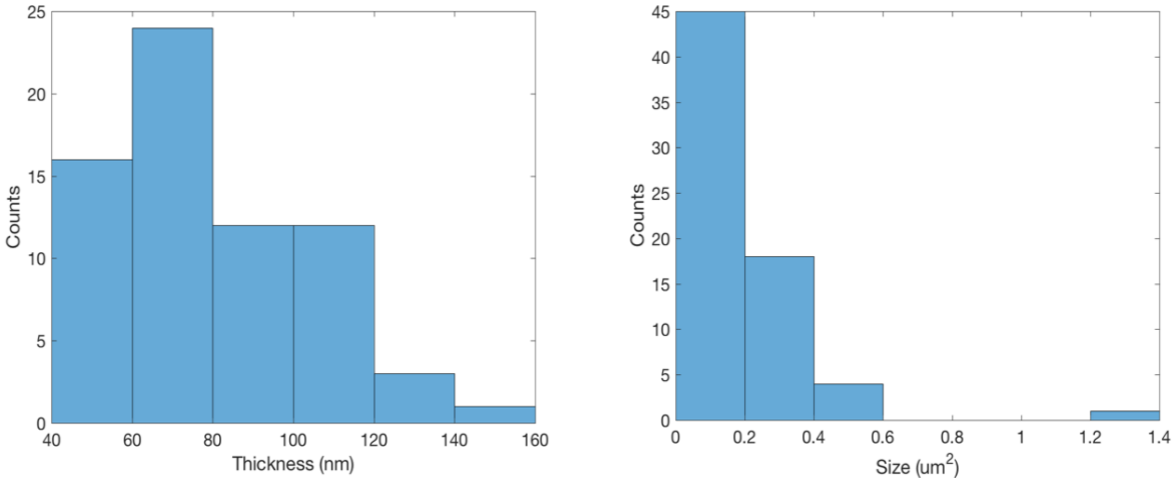

Figure 2.4.3 | Thickness and size distribution of 68 hBN nanoflakes.

Individual single photon emitters are found by fluorescence imaging. We first use scanning confocal microscope to find the emitting spots and then overlay the emission channel onto the laser reflection channel to correlate the emitters and the nano-flakes, as shown in Figure 2.4.4 below.

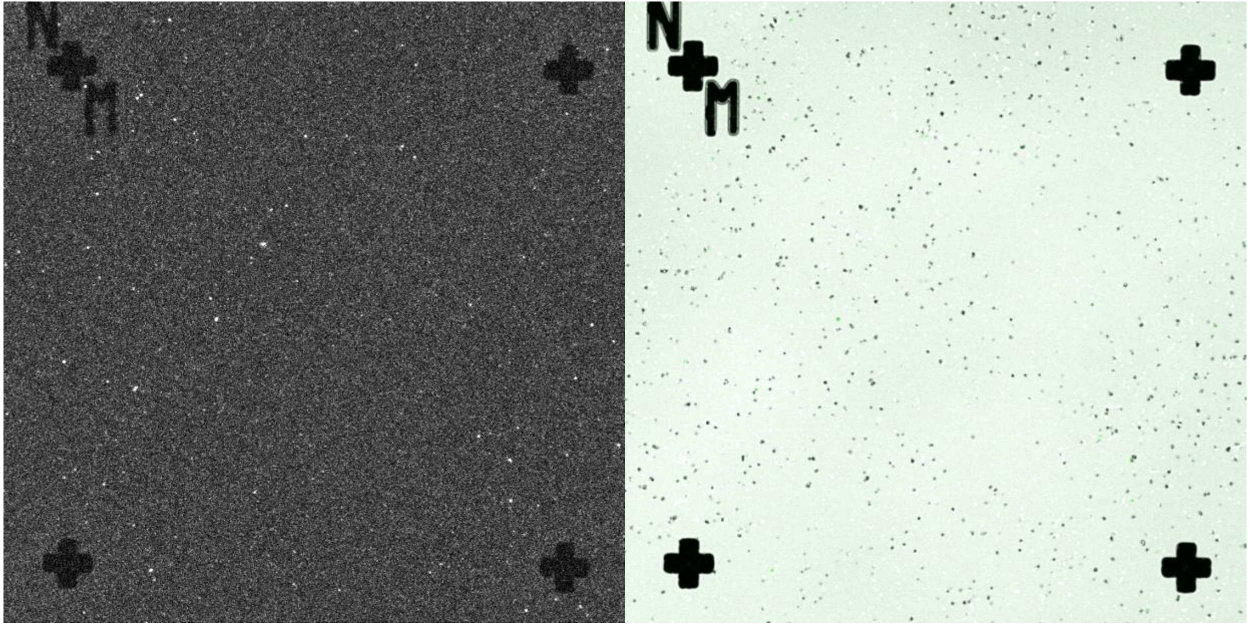

Figure 2.4.4 | Typical scanning confocal microscope image of the photon emission (left) and its overlay on laser reflection (right). Image contrast has been adjusted. The length of the cross marker is 20 um.

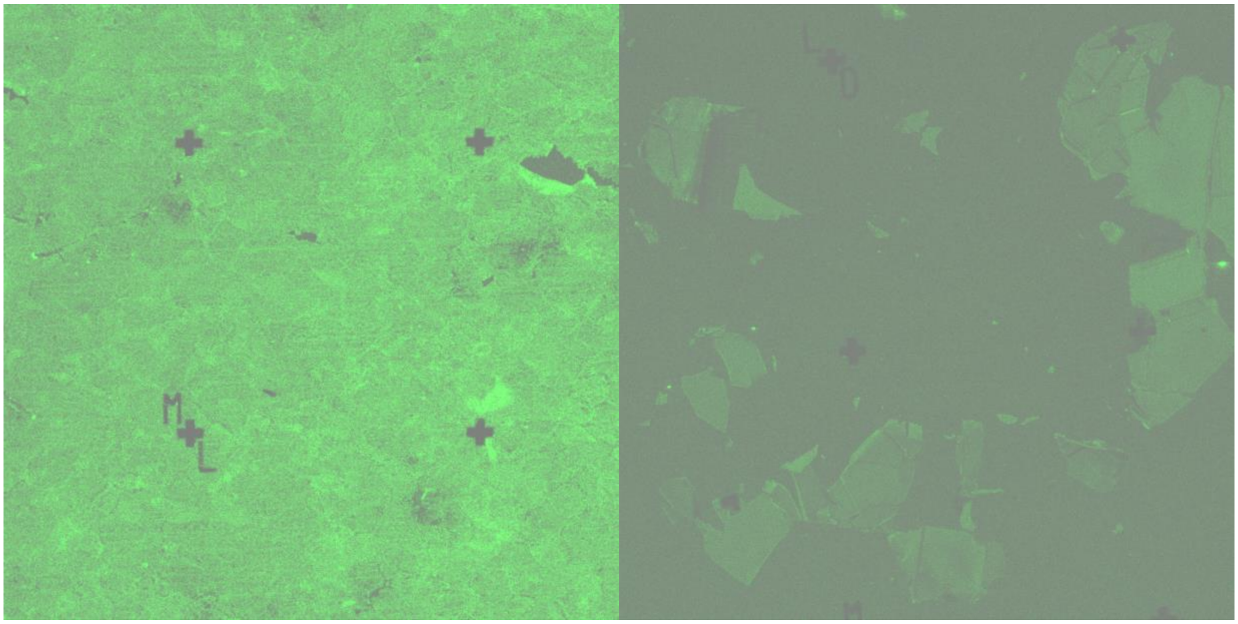

Figure 2.4.5 | Typical scanning confocal microscope images overlay of emission and reflection channels for multilayer CVD hBN (left) and bulk crystal hBN (right) after annealing. Images contrast has been adjusted. The length of the cross marker is 20 um.

In comparison, we also present the scanning confocal microscope images of CVD multilayer hBN and bulk crystal hBN, as shown in Figure 2.4.5. The former has emission almost everywhere on the sample, while the latter has almost no emission from the hBN (the few emission spots turned out to be some dirty on the substrate).

After scanning confocal microscope screening, single-photon emitter candidates are further investigated by photoluminescence (PL) spectroscopy measurement. Figure 2.4.6 below shows a typical emission spectra of emitter with 473 nm continuous wave laser excitation. Majority of the emission goes into the narrow zero-phonon line (ZPL), proving a high-quality emitter. The two phonon-side bands (PSB1 and PSB2) are also visible, with the frequency difference of ~1370 cm_{-1} corresponding to the E_{2g} phonon of hBN (*28*). The well resolved doublet at PSB1 is a typical feature for hBN nanoflakes. A few tiny peaks are visible that might result from the PL emission of other color centers in the collected region.

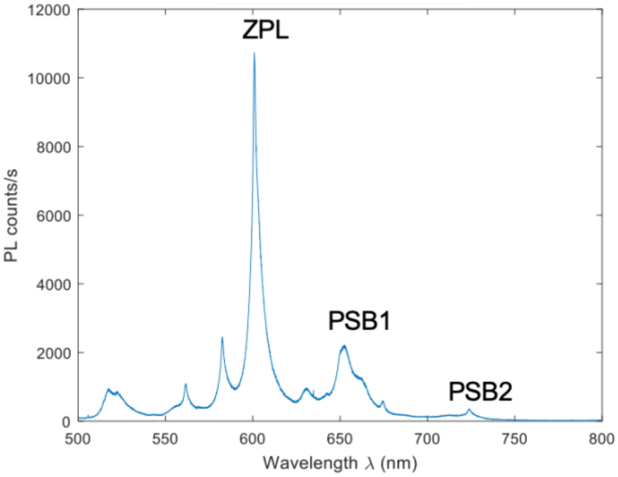

Figure 2.4.6 | Emission spectra of a typical single-photon emitter in hBN nano-flake.

Its second order coherence function $g_{(2)}$ is measured by a HBT setup (Figure 2.4.7). Figure 2.4.8A below presents the measured data with a single exponential fitting following

$$g^{(2)}(\tau) = 1 - \left[1 - g^{(2)}(0)\right]\exp\left(\frac{-|\tau|}{\tau_0}\right) \qquad (2.4.1)$$

which gives the raw $g^{(2)}(0) = 0.21$ without background correction and emitter lifetime $\tau_0 = 3.0$ ns. The $g^{(2)}(\tau)$ data is measured by ten-second signal integration with 100 micro Walt excitation of continuous wave 532 nm laser. In addition, we perform the excitation power dependence of the emission intensity, as shown in Figure 2.4.8B. A typical saturation behavior at non-resonant excitation is observed, which can be fitted by

$$I = I_{Max} \times \frac{P}{P + P_{sat}} \tag{2.4.2}$$

to yield the maximum emission intensity of $I_{Max} = 6.6 \times 10^6$ counts per second and the saturation power of $P_{sat} = 833$ uW. The intensity saturation data is measured with excitation of the same continuous wave 532 nm laser.

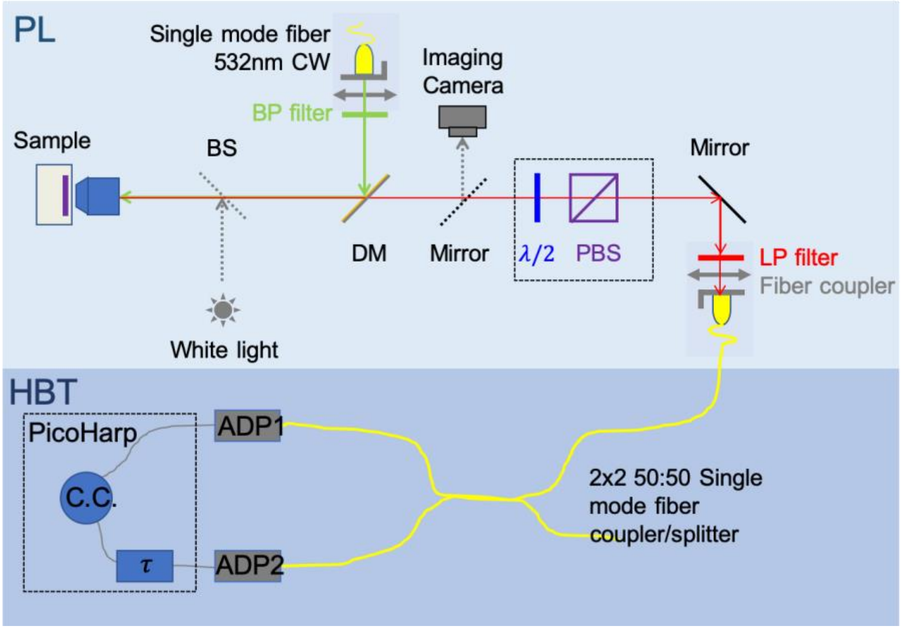

Figure 2.4.7 | Schematics of the photoluminescence (PL) plus Harry Brown Twiss (HBT) setup.

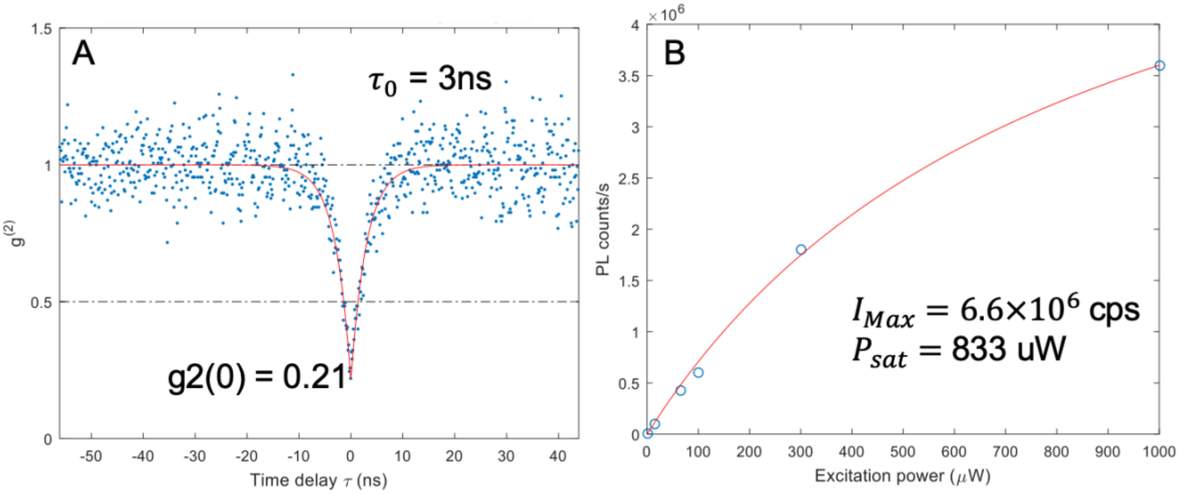

Figure 2.4.8 | Measured $g^{(2)}(\tau)$ and saturation intensity of the single-photon emitter in Figure 2.4.6

Note that the emission intensity is detected value without correction of the optical loss and detector efficiency. Furthermore, there is no additional photonic structure around the emitter to enhance the photon extraction. The detected counts rate of several MHz demonstrates the single-photon emitter in hBN among the brightest emitters discovered so far.

The high quality of the single-photon emitters in hBN have been proved by the narrow zero-phonon line, low value of $g^{(2)}(0)$ and the super-bright emission. Moreover, these emitters are super stable and can last for years in ambient condition. However, as like all the other solid-state single-photon emitters, emitters in hBN also suffer from the inhomogeneous emission wavelength of different emitters. Figure 2.4.9 below plots the histogram of the zero-phonon line position of 126 emitters with 1 nm bin width. The emission wavelength spans a wide range of about 200 nm.

Such emission energy inhomogeneity comes from the variation of the microscopic environment surrounding the emitters. It breaks the indistinguishability of single photons, which is required for large scale quantum computation, such as universal linear optics (*7*), boson sampling (*29*) and quantum walks. For quantum communication, where indistinguishability is not required, the photonic systems usually involve narrow-band components which also place stringent requirement on the precision of single photon energy, especially in the case of wavelength division multiplexing (WDM) for multi-channels and multi-users applications. In all case, controlling the single-photon wavelength is critical. We will discuss our approach to this problem using the Stark effect in the next chapter.

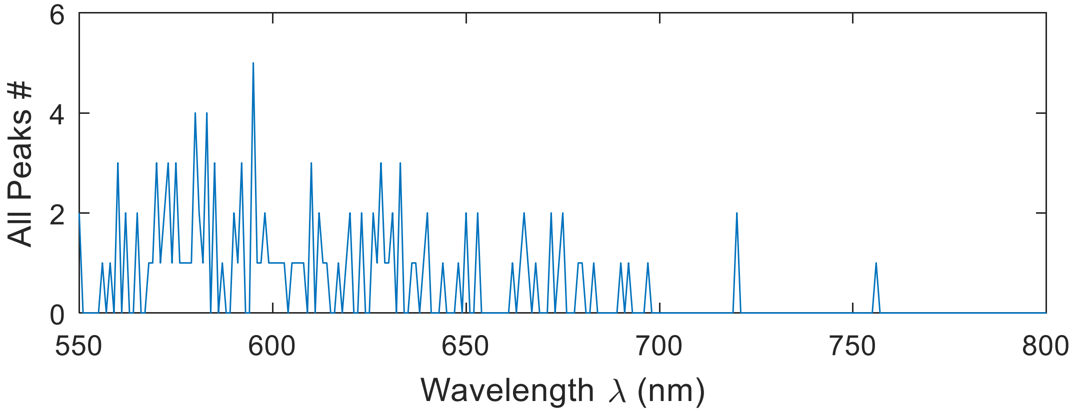

Figure 2.4.9 | Distribution histogram of the zero-phonon line emission wavelengths of 126 emitters in hBN.

2.5 Low temperature emission spectra

At finite temperature, the lattice vibrations, or the phonons, collide with the defect emitters. Therefore, the emission linewidth will be broadened, which increases as temperature increases. Given the measured lifetime of the order of a few nano seconds, the intrinsic linewidth would be on the order of sub GHz or a few micro eV.

To approach the intrinsic linewidth and spectra, we can simply cool down the sample temperature. Figure 2.5.1 below shows the typically measured spectra and linewidth of single-photon emitters in hBN at 5 K as compared to room temperature. Two main features are clear. One is the large linewidth difference about 50 times at the two temperatures, which agrees with the thermal energy scale $k_B T$. The other feature is the slight peak shift, which can to attributed to the temperature induced lattice constant change. In the right subfigure, another small peak at 635.3 nm is resolved, which is buried in main peak at room temperature.

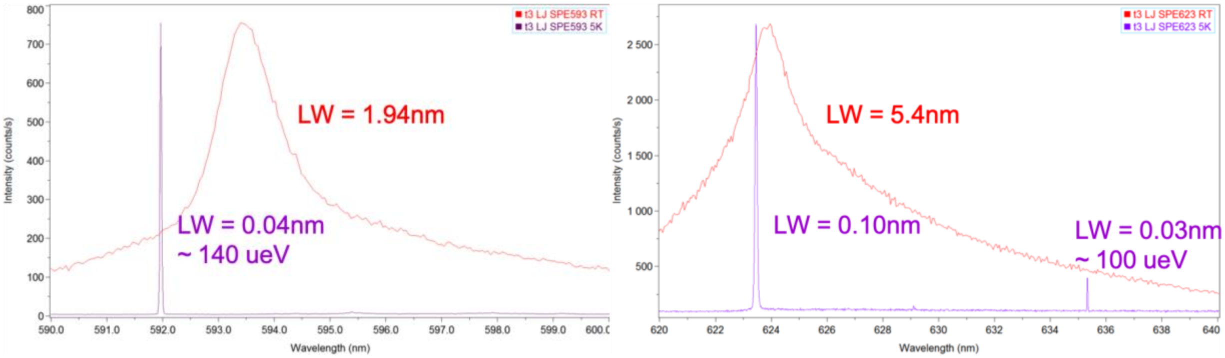

Figure 2.5.1 | Typical spectra and linewidth of single-photon emitters in hBN at 5 K and room temperature.

2.6 Determination of the location of single-photon emitter

Determining the exact location of single-photon emitter is important for photonic integration and precise control. Here, we demonstrate the emitter localization with respect to nano-scale metal electrodes. The emitter spectra and $g^{(2)}(\tau)$ are measured after electrodes fabrication, plotted in Figure 2.6.1 below. The high-quality spectra and fitted $g^{(2)}(0) = 0.45$ verify the single-photon emission.

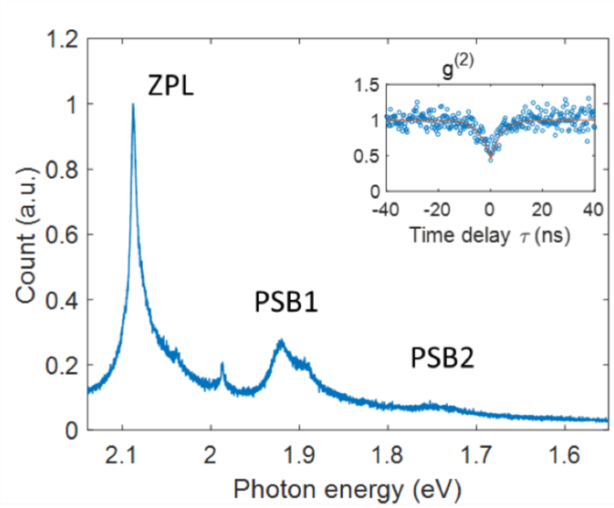

Figure 2.6.1 | Emission spectra of another single-photon emitter in hBN nano-flake with measured $g^{(2)}(\tau)$ in inset.

To find out the location of our single-photon emitter (SPE) with respect to the center of four electrodes, we borrow the concept of single molecule localization microscopy (SMLM) (Figure 2.6.2). After mounting the sample to a home-built SMLM optical setup, we acquire a bright-field image of electrodes and a photoluminescence (PL) image of SPE, separately. The two-channel optical image of Emitter #1 (cyan: electrodes, magenta: PL of SPE) is shown in (a). We analyze the electrode image to determine its center. Each electrode's cross-sectional profile (dotted cyan line) is examined to find its centroid at multiple locations (blue circles), from which two cross lines (red) were least-square fitted to estimate the center of the four electrodes (b). Then, following the standard localization procedure in SMLM, we locate the SPE center by fitting the PL intensity profile with a two-dimensional Gaussian function. (c) shows the SPE image and horizontal and vertical cross-sections at the fitted center (blue plus mark). We repeat the two-channel image acquisition six times, from which an average position of SPE with reference to the electrode center was determined as (-12 nm, -139 nm) with the positional deviation bounded within a ø40 nm circle. (d) shows the spatial distribution of the SPE locations over six measurements (blue cross marks). An average location is marked as a red dot.

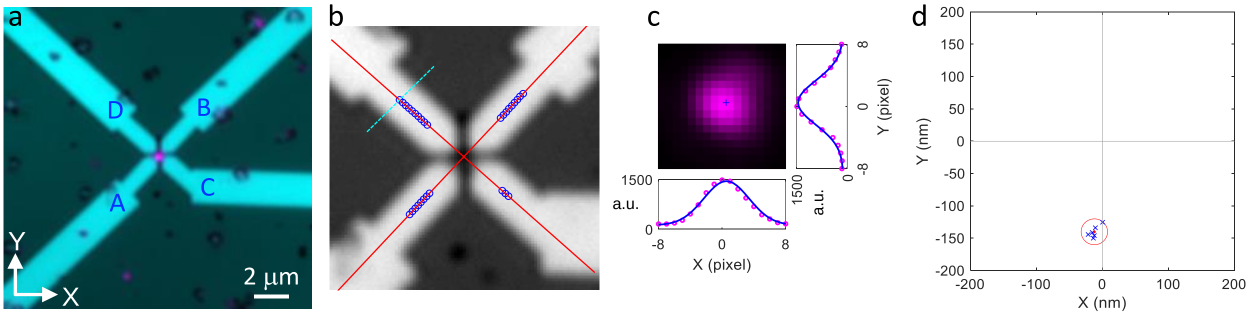

Figure 2.6.2 | Localization of single-photon emitter (SPE). See text for details.

2.7 Comparison with other single-photon emitters

Single-photon emitters in hBN have distinct advantages over other emitters. First, we focus on room-temperature operation and rule out those emitters that only intrinsically exist at cryogenic temperature, such as III-V epitaxial quantum dots and quantum-dot-like emitters in transition metal dichalcogenide. Second, we rule out those unstable emitters such as II-VI colloidal quantum dots (*30*) (despite their being used to demonstrate many concepts) as they are not considered as promising candidate for quantum applications.

Then, left is only color-centers in wide bandgap insulators such as diamond NV center and hBN emitter in this work. Below are comparisons from various perspectives.

1) **Efficient photon extraction.** For NV centers in 3D bulk diamond, it is difficult to extract photons because of total internal reflection due to its high refractive index. When the NV approaches surface of bulk diamond or in nanodiamond, its optical properties degrade (*31*). In contrast, hBN is a 2D material (thus an intrinsic nanomaterial), and there is no photon extraction problem because of the absence of total internal reflection in nanometer thin hBN.

2) **Dipole alignment** is critical for external control. The random orientation of NV dipole in 3D makes it hard to align with electric or photonic controls, particularly in nanodiamond. However, because hBN is a 2D layered material, the color center dipole is expected to lie in plane, and therefore can be well aligned with the horizontal electrodes or photonic structures.

3) **Easy fabrication and integration.** While diamond is a difficult material for integration with the mature Si CMOS technology, hBN is CMOS compatible (*32*).

2.8 Approaches to overcome the limitations of solid-state emitters

There are two inherent limitations of solid-state emitters such as color centers in hBN and diamond: one is their inhomogeneous spatial and/or temporal local environment in the host solid matrix, which breaks the indistinguishability of the single photon and usually manifests itself by random shift of photon energy. To overcome this limit, electric control via Stark effect has been found effective through controlling the photon energy of individual emitters and stabilizing the local charges (for example, in III-V epitaxial quantum dots (*33*, *34*). However, all previous Stark effect was done at liquid helium temperature, because either the emitters only produce single photons at low temperature, or the effect was too weak to observe at room temperature.

The second limitation associated with finite temperature is the homogeneous thermal broadening of the photon linewidth due to electron-phonon scattering. Consequently, room-temperature indistinguishable single-photon generation has never been reported from any solid-state emitter. For example, the radiative lifetime (T_1) of color centers is usually on the order of nano-seconds (2-5 ns for hBN emitter, and ~10 ns for diamond NV), while their room-temperature coherence time (T_2, inverse of linewidth), limited by aforementioned thermal broadening, can be on the order of pico-seconds or shorter (scale of 1 ps for hBN emitter, scale of 100 fs for diamond NV). Equation (2.8.1) below shows how the mismatch between T_1 and T_2 (T_1/T_2 about 1000 for hBN, about 10^4-10^5 for diamond NV) degrades the indistinguishability of single photons. That is, as $T_1/T_2 >> 1$, the characteristic two-photon interference dip ($g^{(2)}(0)=0$ for perfect indistinguishably photons) vanishes (*35*).

$$g^{(2)}(0) = 1 - \frac{T_2}{2T_1}. \tag{2.8.1}$$

To overcome this limitation, the traditional approach is "simply" cooling down the emitter to 4 K or lower temperatures to extend T_2, at the price of complicated cryogenic setup and fighting with the painfulness of sample drift, which severely limits practical applications. For room-temperature operation, one can either reduce T_1 to match T_2 by plasmonic nanoantenna or by cavity quantum electrodynamics engineering (*36*). For example, exceeding 1000 times T_1 reduction has been reported (*37*), which is promising for hBN emitter (but still far from feasible for diamond NV). It is an excellent future direction to incorporate both the electric and photonic control to achieve room-temperature indistinguishable single photons.

2.9 Conclusion and outlook

To conclude, we have presented the characterization of single-photon emitter in hBN and shown its superb properties such as narrow emission linewidth and super bright emission intensity. To move forward, we have to overcome the limitations of solid-state emitters, including emitters in hBN. In next chapter, we will use Stark effect to control the emission energy of single-photon emitter in hBN, addressing the first limitation discussed in last section.

There are a few more next steps along the line. One is to clarify the microscopic atomic and electronic structure of the single-photon emitter in hBN. Actually, since hBN is layered materials, it is possible in principle, for the first, to directly see the atomic structure by a transmission electron microscope (TEM) that can resolve both the atomic positions and species. What's more, such atomic structure can be correlated with the optical information. This is a very exciting idea. We have dedicated lots of efforts along this direction. The difficulty is that monolayer hBN is needed for TEM imaging. However, we found as the hBN approaching monolayer, the optical properties of the single-photon emitter become unstable and the spectra becomes very broad as that in CVD hBN samples.

Another one is to deterministically create single-photon emitters in pristine hBN crystal. This is important for scalable integration with electrical and/or photonic structures for precise control and large-scale circuits. We also dedicated a lot of efforts along this direction using scanning helium ion beam microscope to introduce local defects in a precision of sub-nanometer. We have tried a variety of helium ion dose and density. After high temperature annealing, we indeed found photon emission from patterned region, but the emission spectra were always very broad and there were no sharp emission peaks as we would expect from high quality emitter.

For single emitter strong coupling, it has never been achieved in diamond NV due to the difficult material fabrication, but hBN emitter could be easier because of the layered material structure and COMS compatible fabrication.

Another one is to explore the possibility of spin-dependent electronic states as in diamond NV center for quantum bit, which is an interesting future direction.

3 Room-temperature giant Stark effect of single-photon emitter in hBN

3.1 Introduction

To integrate single-photon emitters (SPEs) into quantum computation and communication systems, controlling the photon energy is critically required. As we see from last chapter, one of the major challenges for all solid-state single-photon emitters is the spatial- and temporal- inhomogeneity of their microscopic environment. Such inhomogeneity breaks the indistinguishability of single photons and usually manifests itself in the lift of energy degeneracy from multiple emitters. For large scale quantum computation, such as universal linear optics (*7*), boson sampling (*29*) and quantum walks, indistinguishability is required. For quantum communication, where indistinguishability is not required, the photonic systems usually involve narrow-band components which also place stringent requirement on the precision of single photon energy, especially in the case of wavelength division multiplexing (WDM) for multi-channels and multi-users applications. Because such technology requires the wavelength of light source precisely aligned to predefined grid and communication channels are distinguished by the photon energy.

Stark effect, a well-established phenomenon in atomic physics, describes the shift of spectra lines by an external electric field. It can precisely control single-photon emitters photon energy. Further, such electric control can be facilely integrated into quantum systems (*38*), advantageous over other tuning methods such as temperature (*39*), strain (*40, 41*) and magnetic field (*42*). Thus far, Stark effect has been used to tune the single-photon energy of III-V epitaxial quantum dots (*38*), quantum-dot-like emitters in layered WSe_2 (*43*), atomic defect emitters in diamond such as NV and SiV centers (*44–47*), as well as organic dye molecules (*48*). However, because either the emitters only produce single photons at low temperature, or the effect was too weak to observe at room temperature, all the previously demonstrated Stark shifts were all at liquid Helium temperature, placing significant challenges for practical quantum applications.

In this chapter, we describe our results of the first room-temperature Stark effect of SPEs with giant tuning ranges of 31 meV, discovered in hBN color centers. Moreover, we develop a Rotating Field Method to resolve the angular dependence of the Stark effect to determine the breaking of inversion and rotation symmetries at the hBN SPE. The discovered remarkably giant room-temperature Stark effect and the significant advance in understanding its atomic structure could enable new possibilities of quantum information technologies, such as WDM and indistinguishable single photon sources, at room temperature.

3.2 The physics and device implementation of the Stark effect

The physics of Stark effect is illustrated in Figure 3.2.1. A two-level system representing the single-photon emitter (SPE), with an optical transition from the excited level $|e\rangle$ to ground level $|g\rangle$, is perturbed by the local electric field $\mathbf{F}$ induced by applied voltage. Consequently, the electronic orbitals of the two levels are distorted and the transition single-photon energy is shifted. According to perturbation theory of quantum mechanics, to the second order approximation, the Stark shift can be modeled as the following formula (*43–45, 49*):

$$h\Delta\nu = -\Delta\boldsymbol{\mu}\cdot\mathbf{F} - \frac{1}{2}\alpha|\mathbf{F}|^2 \tag{3.2.1}$$

where $h\Delta\nu$, $\Delta\boldsymbol{\mu}$, $\mathbf{F}$ and α denote the change in emission photon energy, the difference between dipole moments of ground state $|g\rangle$ and excited state $|e\rangle$, the local electric field acting on the emitter, and the atomic polarizability, respectively. That is,

$$\Delta\boldsymbol{\mu} = \boldsymbol{\mu}_{\boldsymbol{e}} - \boldsymbol{\mu}_{\boldsymbol{g}} = \langle e|\mathrm{e}\mathbf{r}|e\rangle - \langle g|\mathrm{e}\mathbf{r}|g\rangle \tag{3.2.2}$$

where e is the electron charge and $\mathbf{r}$ the real space position vector. For a two-level system with a permanent dipole moment, Equation (3.2.1) can be simplified to

$$h\Delta\nu = -\Delta\boldsymbol{\mu}\cdot\mathbf{F} = -|\Delta\boldsymbol{\mu}||\mathbf{F}|\cos{(\phi-\theta)} \tag{3.2.3}$$

where ϕ and θ denote the orientation angles of the dipole moments difference $\Delta\boldsymbol{\mu}$ and of the electric field $\mathbf{F}$, respectively. Following previous reports (*43–45*), we adopt the Lorentz approximation to calculate the local field $\mathbf{F}$ from applied field $\mathbf{E}$ as $\mathbf{F} = \mathbf{E}(\varepsilon+2)/3$, where ε is the permeability of the hBN. At finite temperature T, the electronic levels are broadened ($\Delta E(T)$) due to electron-phonon scattering and so does the emitted photon energy. As a result, the Stark shift ($h\Delta\nu(\Delta\boldsymbol{\mu},\mathbf{F})$) needs to be large enough to be observable and useful.

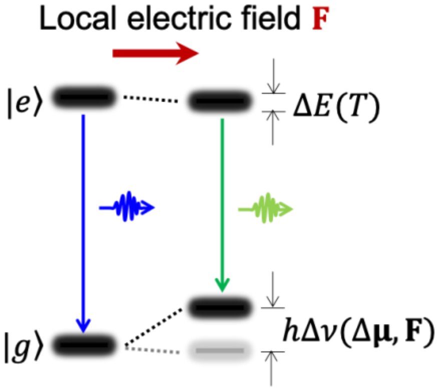

Figure 3.2.1 | The physics of Stark effect.

In this study, SPEs in multi-layer hBN nano-flakes are chosen due to their much better optical performance compared to those in monolayers (*24*). Individual single photon emitters are found by fluorescence imaging and characterized by PL emission spectroscopy, polarization analysis and $g_{(2)}$ measurement. Then electron beam lithography is used to define the electrode pattern around the located SPEs.

Multiple electrodes are carefully designed to surround the SPEs such that we can control not only the amplitude but also the direction of the electric field. We fabricate miniature gaps of a few hundred nanometers between the adjacent and diagonal electrodes, respectively, which can generate a large electric field in the order of ~ 0.1 V/nm. Figure 3.2.2a shows the two-channel optical image of the fabricated four-electrode device (Emitter#1), where the gold color is the bright-field image of the gold electrodes and red color the photoluminescence (PL) image of the hBN SPE. Presented in Figure 3.2.2b is the zoom-in pseudo-color SEM image of the same device. The blue region is the hBN flake and the red dot marks the location of the SPE determined by fitting its photoluminescence (PL) image in Figure 3.2.2a with respect to the electrodes after fabrication (details in Figure 2.6.2). A, B, C and D (yellow) are the four gold electrodes where voltages are applied to generate external **E** fields. The black arrows show the adopted coordinate system.

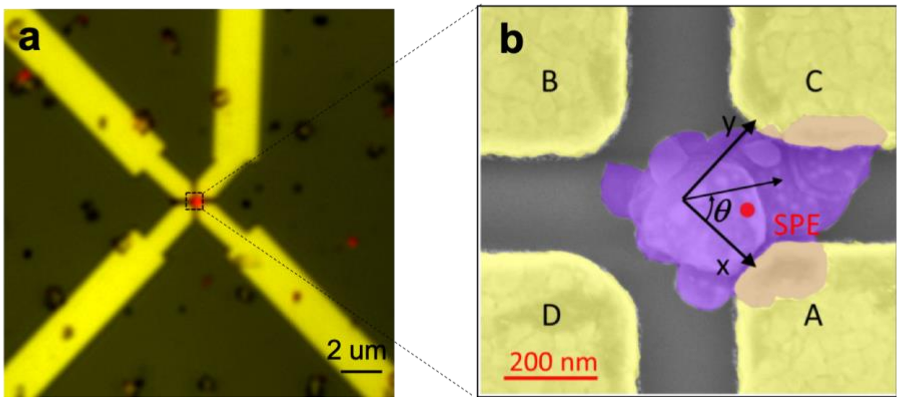

Figure 3.2.2 | The four-electrode device for Stark effect in hBN single photon emitter.

3.3 Observation of room-temperature giant Stark effect

After characterizing and confirming the optical properties of our device, we apply electric fields to the SPE to study the Stark effect. Voltages within ±100 V are applied to electrodes A and B with equal magnitude of opposite signs (Figure 3.3.1a Inset) while PL emission spectra are collected at each voltage. Figure 3.3.1a plots the zero-photon line (ZPL) PL intensity map as a function of photon energy and applied voltage. A giant Stark shift up to 31 meV is clearly observed, about one order of magnitude greater than the values previously achieved in color center SPEs (*44*, *45*) and 4 times of its room-temperature linewidth (~ 7 meV). We plot the ZPL peak position as a function of applied voltage in Figure 3.3.1b. The blue and red color corresponds to change of voltage in forward and backward directions, respectively. The dots are experiment data with errorbars showing the 95% confidence interval from fitting. It is clear that the Stark shift is approximately linear to the applied voltage and reverses sign at opposite electric field. Linear regression of data in Figure 3.3.1b gives a tuning efficiency of 137 μeV/V. The deviation from linearity is possibly due to the light induced ionization in nearby non-emitting defects that can modify the local electric field(*45*). Insets of Figure 3.3.1b show the $g_{(2)}$ of the device at +10V and -10V, which changed little compared to the 0V case as in Figure 2.6.1 inset, proving single photon emission with applied voltage. The spectra and $g_{(2)}$ are measured under the excitation of a continuous-wave 473 nm and 532 nm laser, respectively. The acquisition time for $g_{(2)}$ is 10 s. The excitation intensity is 100 uW/um$_2$ for all. All the Stark effect data are measured in vacuum, while $g_{(2)}$ is done in ambient air.

We can learn some about the electronic states of the SPE from our Stark effect data. The possibility is ruled out that the observed linear Stark shift is due to the presence of degenerate states, because there is neither ZPL splitting nor multi-peaks with applied fields, even when the excitation polarization is changed ~30 degrees to account for possibly different selection rules of different states. Note in the previous Stark effect of diamond NV center, two near-degenerate transitions from A2 to {E1, E2} states were visible, and both ZPL tuning and splitting were observed (*45*). Therefore, the measured linear Stark effect here unveils the electric permanent dipole moment in the atomic structure of the hBN color center, which we will discuss in more details later.

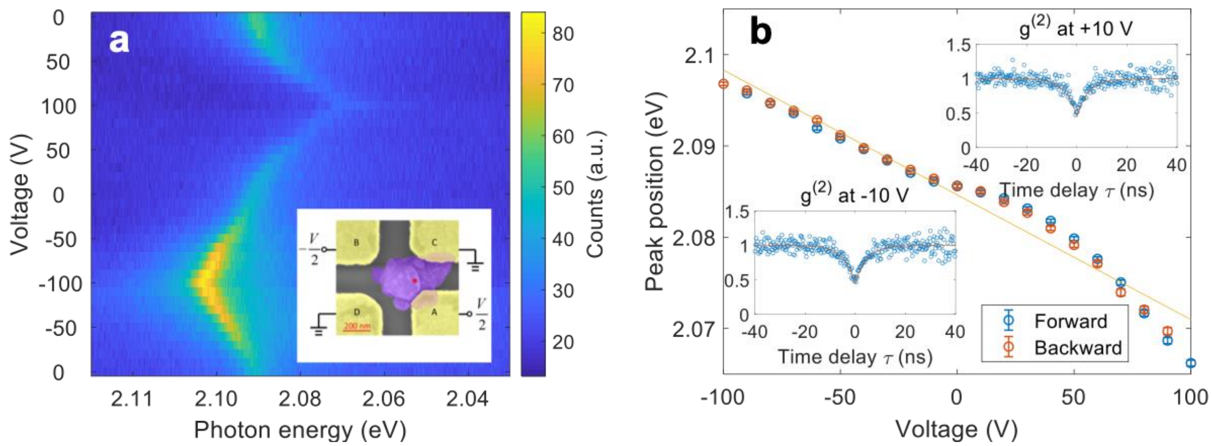

Figure 3.3.1 | Observation of room-temperature giant Stark effect.

We also plot the ZPL linewidth and intensity as a function of applied voltage in Figure 3.3.2. As voltage change from -100V to 100V, the ZPL linewidth gradually increases with its intensity gradually decreases. Such behavior was also observed in previous study in diamond NV center, possibly due to the change of coupling to some dark state (*44*).

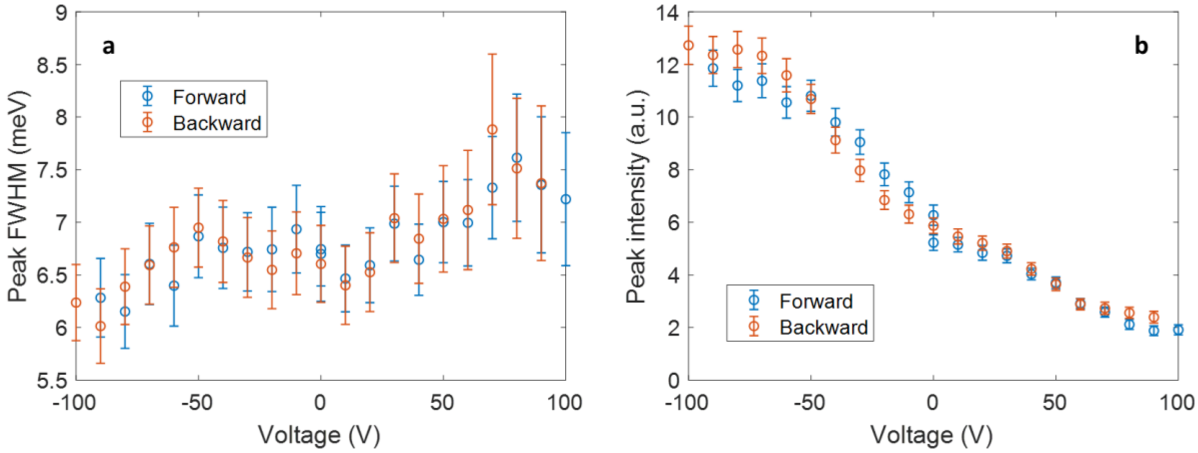

Figure 3.3.2 | ZPL linewidth and intensity as a function of applied voltage of Emitter #1 extracted by fitting to Lorentzian function.

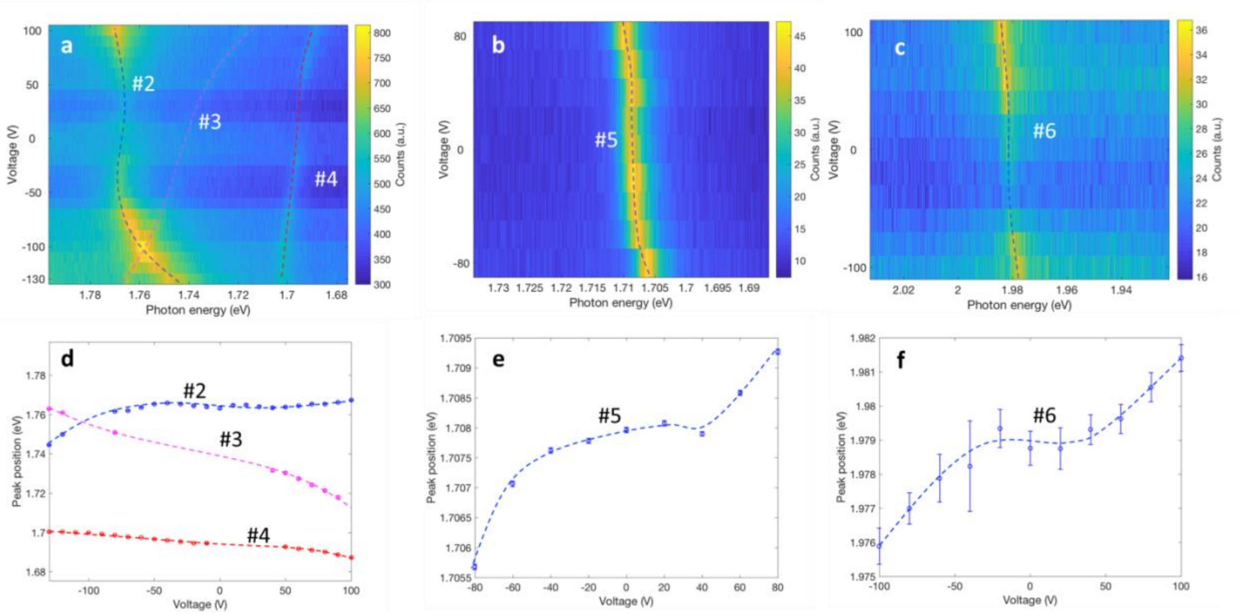

Figure 3.3.3 | Room-temperature giant Stark effect of Emitter #2-6.

We present in Figure 3.3.3 additional room-temperature Stark shift data. **a, b** and **c** show the room-temperature intensity maps of five more emitters (Emitter #2-6) in three more devices as a function of photon energy and applied voltage. **d, e** and **f** show the corresponding fitted peak positions as a function of applied voltage. All the dashed lines are guides to the eye for the peak change. Note that in **a**, at voltage near -100V, remarkably, two peaks from two different emitters are tuned into resonance, which is very important to achieve room-temperature indistinguishability between different emitters.

We further analyze the statistics of Stark effect measured on the six emission lines from the four devices. The observed Stark shifts ranging from 3.5 to 45 meV with an average of about 20 meV. The variety of shift is mostly due to the variation in the local electric fields and their alignment with the dipole of hBN emitters.

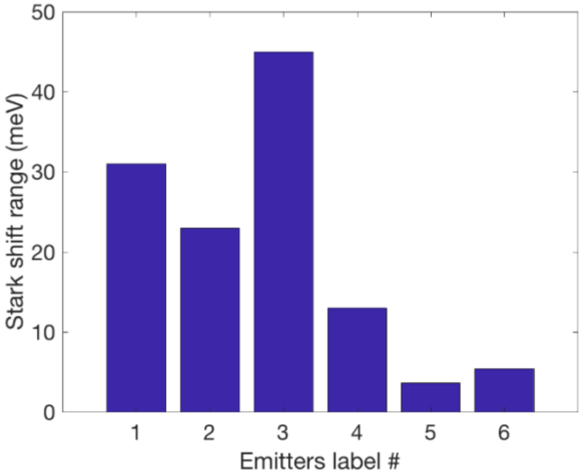

Figure 3.3.4 | The statistics of Stark shifts of the six hBN emitters at room temperature.

We emphasize that the key to observe the room-temperature giant Stark shift is a combined effort of several factors, as formulized in Equation (3.2.3). First of all, the large band gap of hBN crystal and low phonon scattering make a superb room-temperate SPE. Second, the layered structure of hBN likely leads to an in-plane dipole moment (*24*), such that an applied in-plane electric field can be aligned with the dipole orientation. Third, closely spaced electrodes (within hundreds of nanometers) can be easily integrated with the nano-scale hBN flake and large voltages more than 100 V can be applied, resulting in local electric fields around one order of magnitude greater than previous works in diamond color centers. Remarkably, the hBN SPE are stable at such high field and its Stark tuning is reliable.

3.4 Wavelength modulation of single-photon emitters by Stark effect

The reported room-temperature giant Stark effect is a significant advance for photonic quantum technology. The demonstrated energy tuning range is sufficient for WDM for multi-channel and multi-user quantum key distribution (QKD) application in quantum communication, particularly suitable for free-space short-distance mobile QKD, which is the unexplored complementary scenario compared with the highly developed fiber-based long-distance point-to-point QKD.

To further demonstrate the feasibility of wavelength-division-multiplexing, we modulate the emitters ZPL spectra as driven by the Stark effect. During the modulation operation, the emission lines at different voltage are well separated and is reliably for many cycles.

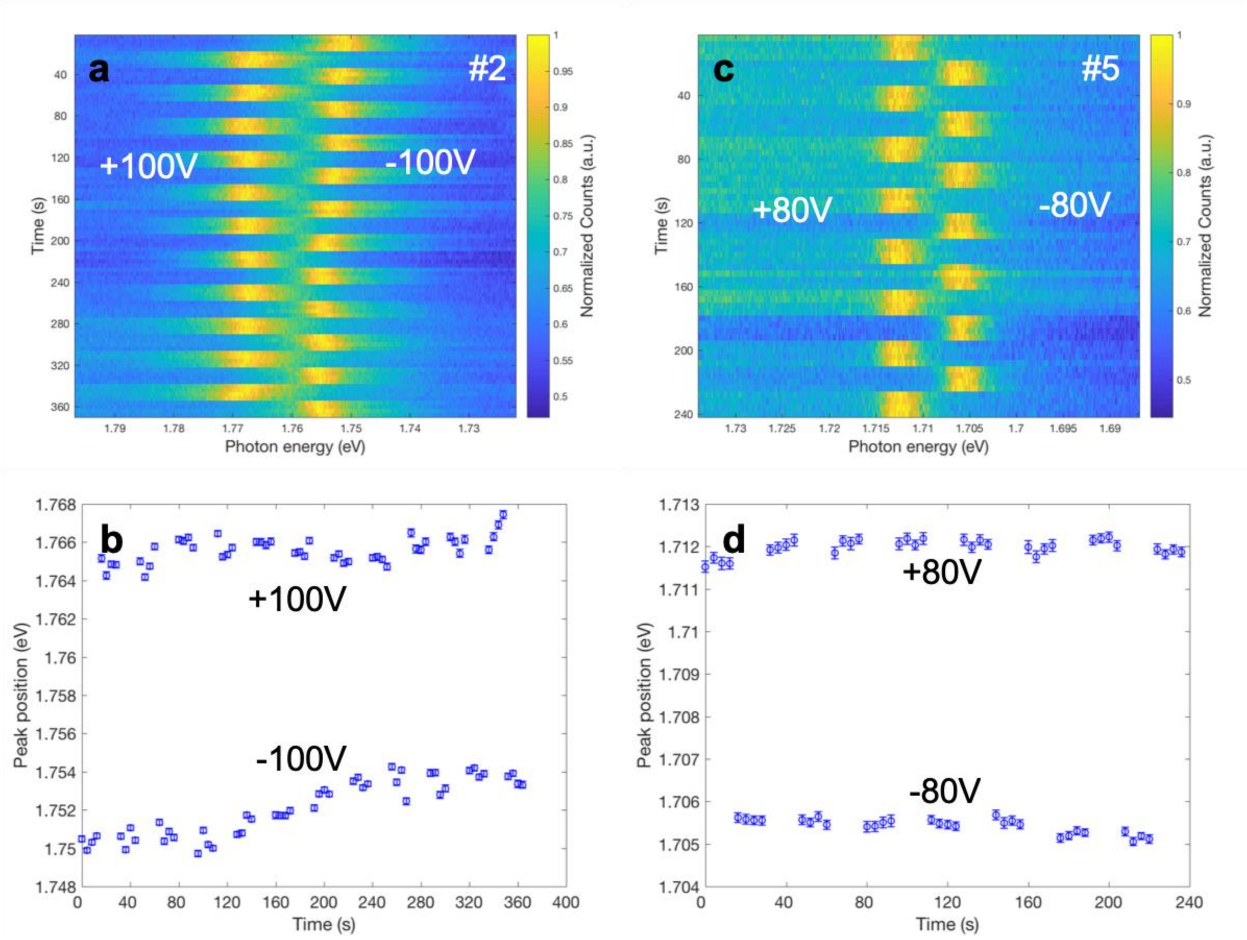

Figure 3.4.1 | Room-temperature wavelength modulation of Emitter #2 and #5 by Stark effect.

3.5 Low temperature Stark effect

Stark effect is in principle independent of temperature as indicated by Equation (3.2.3). In reality, the surrounding environment of solid-state single-photon emitters could be affected by temperature through phonons and free charges. To verify the observed giant Stark shift is not artifact or temperature effect. We measure the same Emitter #1 under same conditions expect a lower temperature of 80K. For the same voltage range, the measurement at 80 K shows similar Stark shift as that at room temperature.

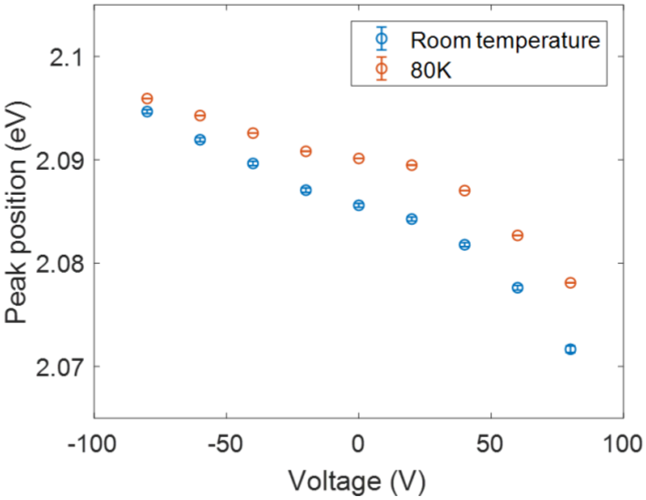

Figure 3.5.1 | Stark shifts of Emitter #1 at room temperature and 80 K.

3.6 Broken symmetries revealed by the angle-resolved Stark effect

According to Equation (3.2.3), the Stark shift depends not only on the magnitude of the applied field, but also its orientation (*50*). In order to probe the angular dependence of the Stark effect and therefore the underlying symmetry of the atomic structure of the color center, we introduce the Rotating Field Method by utilizing the linear combination of the fields generated by the multiple electrodes. As long as the individual fields are linearly independent, their combination can produce fields of arbitrary directions and magnitudes (although limited by dielectric breakdown). With finite element method (COMSOL) simulation, we calculate the voltages for electrodes A and C (other electrodes and substrate are grounded, Figure 3.6.1a) that generate a combined electric field at any specified direction with a constant magnitude at 0.08 V/nm. The ZPL spectrum of the hBN SPE shows strong dependence on the direction of the applied field (Figure 3.6.1b). The ZPL is 1.13 meV red (1.32 meV blue) shifted when the applied field pointing to $\theta = 140°$ (320°), while the shift with the electric field along $\theta = 230°$ is negligible. The zero-field spectrum is plotted for comparison.

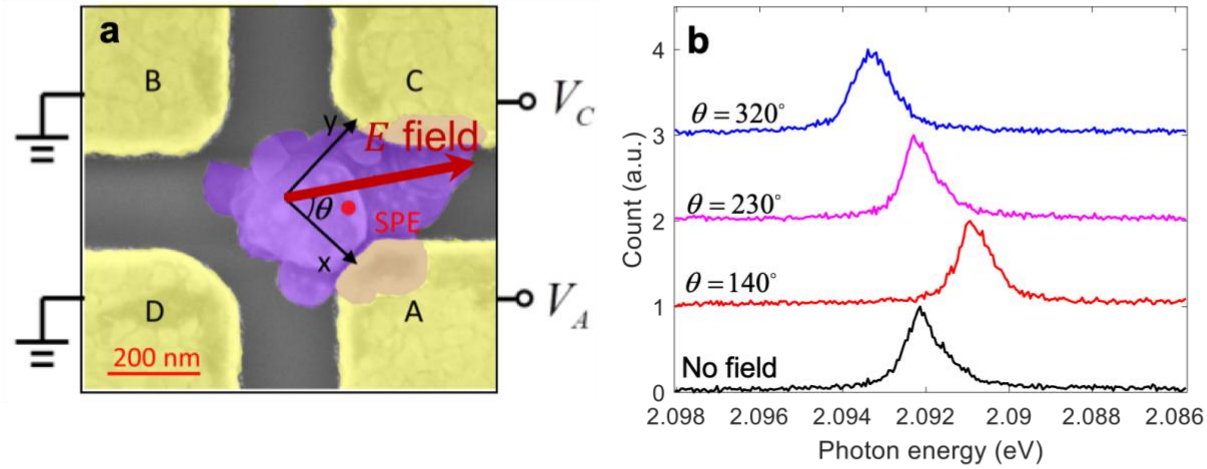

Figure 3.6.1 | The angle-resolved Stark effect of hBN SPE.

We also measure the ZPL spectra per 10° step of θ in electric field direction and extract the Stark shifts by fitting each spectrum data with Lorentzian function. Figure 3.6.2a depicts the obtained Stark shift as a function of the applied field direction θ (orange squares). Two values of the direction angle θ can be clearly identified in the pattern that are orthogonal to each other and correspond to the directions for maximum and zero shifts. Electric fields of opposite directions induce shifts with reversed signs. Our data is well fitted by Equation (3.2.3) (orange solid lines in Figure 3.6.2a), which further confirms that the Stark effect is dominated by an electric permanent dipolar term and that higher order terms are negligible. From the fitting we calculate the magnitude of the dipole $\Delta\boldsymbol{\mu} =$ 0.65 ± 0.04 D where 1 D = 3.33e-30 Cm. The obtained dipole moment is on the same order as that of the NV center in diamond (*44*). Three vertical arrows (blue, magenta and red) correspond to the three spectra in Figure 3.6.1b. The photon energies are obtained by fitting the ZPLs with the Lorentzian line shape. The error bars from fitting are smaller than 0.03 meV. The data is measured at 80 K to reduce ZPL fitting uncertainty at small shifts, taking advantage of the narrow linewidth at low temperature. The optical polarization is measured at room temperature without applying voltage. The same data are plotted in polar coordinates in Figure 3.6.2b, which clearly shows the dipole pattern from the angle-resolved Stark effect. The polarization direction of the excitation laser is also indicated by the green arrow.

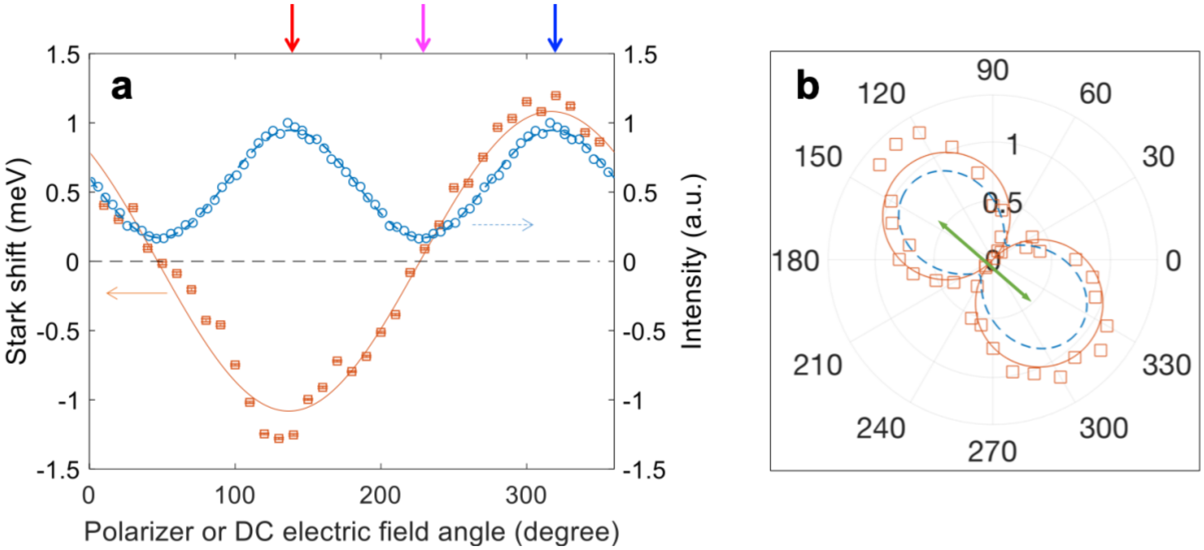

Figure 3.6.2 | The discovered permanent electric dipole and broken symmetries (Emitter #1).

The discovered permanent dipole moment proves that only mirror symmetry is present in the atomic structure of the color center and that both the inversion symmetry and three-fold rotation symmetry of the host hBN crystal are broken. The valuable information about the symmetries will significantly facilitate the future study of the atomic structure and electronic levels of the color center. In contrast, all the previously reported linear polarization of the emitted photons only indicates anisotropy of the emitter structure. Actually, the optical transition dipole responsible for linearly polarized emission corresponds to the off-diagonal terms in the matrix of dipole operator,

$$\boldsymbol{\mu}_{e\to g} = \langle g|e\mathbf{r}|e\rangle \tag{3.6.1}$$

and only the absolute value $|\boldsymbol{\mu}_{e\to g}|$ can be determined in emission polarization measurement, which is inversion symmetric. In contrast, the permanent dipole uncovered in our linear Stark effect corresponds to the diagonal terms (Equation (3.2.2)), both magnitude and direction of the vector are determined. Apparently, the two dipoles are fundamentally different. We re-plot the linear emission data in Figure 3.6.2a (blue), to clearly show the difference from the Stark effect. Noted that the direction for maximum Stark shift is coincident with that of the emission polarization, which corresponds to the intersection axis of the planes of the color center mirror symmetry and the hBN atomic layer.

3.7 Stark effect on emission polarization

Since Stark effect perturbates the electron orbitals, it could affect the emission transitional dipole and hence the single photon polarization. However, in our study, the rotation of the polarization should not be significant because the applied electric field is only small compared with the internal electric field. The former is on the order of E1 ~ 0.4 V/nm, while the internal electric field can be estimated as $E_0 \approx \frac{e}{4\pi\varepsilon_0 r^2} = 16$ V/nm where r ~ 3 angstrom is the in-plane lattice constant of hBN. The expected rotation due to the perturbation may be estimated as arctan(E1/E0) ~ 1.4°. We conducted the polarization measurement on one bright emitter and obtained a small rotation of polarization ~ 1.6° when the voltage changes from -80 V to 80 V, which is comparable to our estimation.

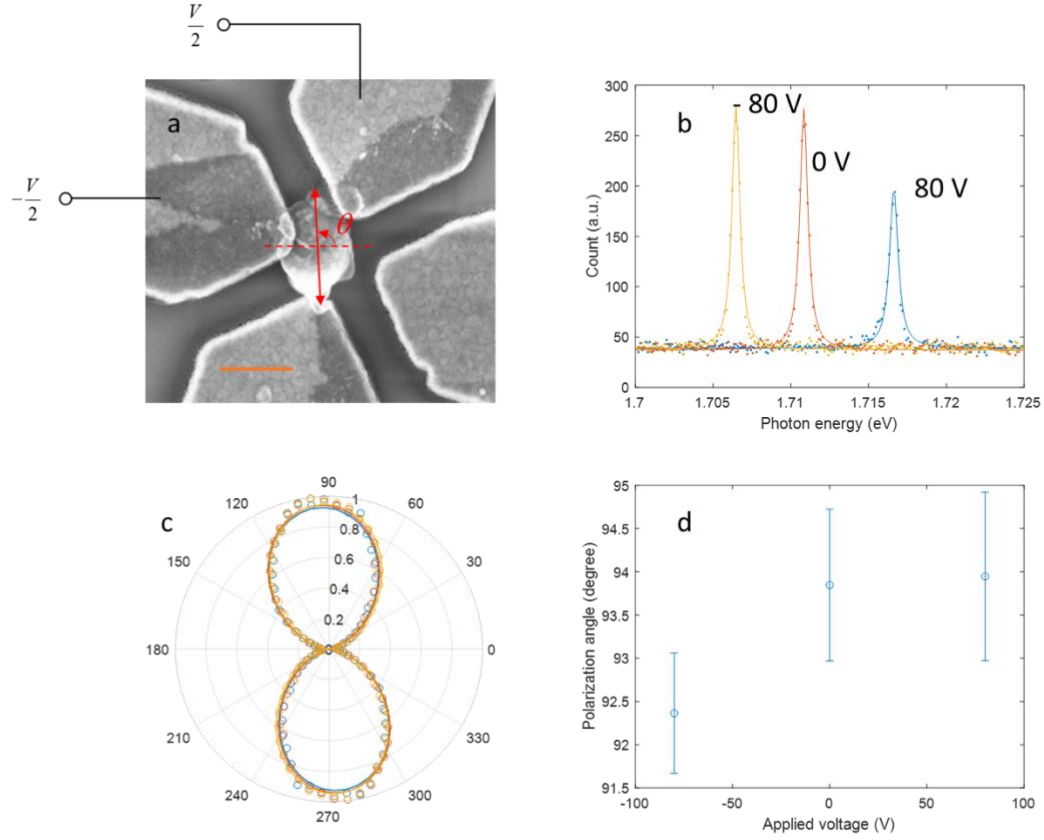

Figure 3.7.1 | Emission polarization at different voltages.

Figure 3.7.1a shows the SEM photo of the device and electric voltage configuration for the polarization characterization at 80 K (rest electrodes and substrates are all grounded). The arrow shows the approximate direction of the measured polarizations. θ denotes the convention of the angle used in c and d. The scale bar is 400 nm. Figure 3.7.1b is the zero-phonon line spectra measured at different voltages. The dots (lines) are experiment data (Lorentzian fitting curves). A wide Start shift of ~9 meV was clearly observed. Figure 3.7.1c presents the polarization measurement and curve fitting at different voltages. The change in polarization is very small. The dots represent intensities corresponding to different polarizer angles and are calculated from peak area of Lorentzian fitting with background subtracted. The lines are squared cosine fitting curves. The colors indicate the applied voltages as in b. Figure 3.7.1d shows the fitted polarization angles and 95% confidence intervals. The measurement was done at 80 K to improve the signal to noise ratio.

3.8 Conclusion and outlook

To conclude, in this chapter we demonstrate the first room-temperature Stark effect of a SPE with a giant shift of 31 meV in hBN color center. This is achieved by combined advantages including the large bandgap and low phonon scattering in hBN, the layered structure of hBN and our ability to make a nanoscale device using hBN nano flake. The large tunability is indispensable to align single photon energies to photonic cavities or predefined standard to construct WDM quantum communication systems.

Furthermore, the large tunability is critical to room-temperature production of indistinguishable photons from multiple SPEs by compensating their emission energy variation for large-scale quantum computation. The high quality of hBN emitter makes it possible to generate room-temperature indistinguishable single photons, a grand challenge for solid-state single-photon emitter that was never possible, by boosting the radiative lifetime about one thousand times to match its coherence time or by cavity quantum electrodynamics engineering (Section 2.8).

We also introduce a method to characterize the Stark effect with respect to the electric field direction, which enables the first angular mapping of Stark effect. The mapped permanent electric dipole moment, aligned with the optical emission dipole, proves that both the inversion symmetry and three-fold rotation symmetry of the host hBN crystal are broken at the color center. Our results provide insightful information for further exploring the properties and applications of the color center in hBN. The room-temperature operation, large tunability, and integrability of hBN SPE could enable scalable solid-state quantum information systems at room temperature.

Remark: Chapter 2 and Chapter 3 include published materials from Yang Xia*, Quanwei Li*, et. al. "Room-temperature giant Stark effect of single photon emitter in van der Waals material, Nano Lett. 2019, 19, 10, 7100-7105" (*contributed equally) (*51*).

4 Nonlinear optics at excited states of valley polaritons in monolayer WS_2

4.1 Introduction

In quantum mechanics, a quantum particle, such as atom and molecule, can be excited from the lowest energy ground state to higher energy states (i.e. excited states), after absorbing energy from incident light. Then, the quantum particle can relax to the ground state by releasing the energy in forms of light or heat. Such a cycling process describes the basic picture of light-matter interaction (in the frame of quantum electrodynamics), where the properties of the excited states and their dynamics are the crucial elements. The study of excited states of gas atom and molecule date back to the 19th century with the discoveries of the Fraunhofer lines in solar spectrum and Balmer series of hydrogen atom, which leads to fluorescent lamps and the discovery of quantum mechanics. Later on, the study of excited states of doped ions in solid state crystal gives birth to the powerful solid-state lasers, and the trace of excited states in Calvin cycle elucidated the path of photosynthesis. In the recent decades, the excited states of quantum particles are manipulated towards building a practical quantum computer.

Despite the importance of excited states in determining the properties of quantum particles, however, there is little study on the excited states of quasi-particle in condense matter system. This is partially because the complicated state structure and environment in such system. For example, excited states of exciton polaritons (EP), the fundamental half-exciton half-photon particles in solid-state cavities, critically control the quantum electrodynamics (QED) and present distinctive light-matter interactions, empowering coherent manipulation of solid state quantum states (*52*–*55*), impossible in ground states. Regardless of their vital importance, the physics of EP excited states, however, remain elusive due to the difficulty accessing such states.

In this chapter, we directly probe the excited states of solid-state EP, in a monolayer tungsten disulphide (WS_2) microcavity. Utilizing novel valley sensitive nonlinear spectroscopy, we unravel the valley-dependent dark 2p excited states through two-photon luminescence and directly look into the dynamically unstable upper polariton band by the instantaneous second harmonic generation. Our study of the EP excited states in transition metal dichalcogenide (TMD) monolayer clarifies the valley-degenerate EP excited states and their underlying quantum dynamics, paving the way to intriguing phenomena such as room temperature valley polariton condensation and chiral superfluidity (*56*). Additionally, the excited states together with the ground states construct a unique valley-degenerate three-level system (*57*), promising great potential in solid-state stimulated Raman adiabatic passage (STIRAP) (*58*) in the solid state and nonlinear control in valley-polaritonic applications (*55, 56*).

4.2 Exciton polaritons and their excited states

Exciton – bond state of an electron and a hole – is the fundamental quasi-particle in semiconductor that mimics hydrogen atom. Its important role in the optical properties of III-V semiconductor, carbon nanotube and transition metal dichalcogenide (TMDC) has been uncovered through the study of excitonic states. When placed in micro-cavity (MC), excitons can hybridize with cavity photons to form new quasi-particles named exciton polaritons in the strong coupling regime. That is, the coupling rate between excitons and photons exceeds both the exciton decay rate and photon leakage rate. Such half-matter half-light quasi-particle inherits the best of its parents: the strong inter-particle interaction from the exciton and ultra-light mass from the light, all in the controllable and scalable solid-state system. EP demonstrate striking physical phenomena that are extremely difficult in conventional solid-state materials, such as Bose-Einstein condensation (BEC) and photon blockade (*52, 53*).

In contrary to the ground states (lowest polariton band), the EP excited states (higher energy bands) introduce distinctive fundamental properties, such as different parity symmetry and quantum coherence (*52–54, 57, 59–62*). They also show abundant QED, including coherent energy exchange (*59, 60*), ultrafast terahertz transitions (*57, 61*), and optical selection rules (*54, 57, 61, 63, 64*). The EP excited states thus broadly impact on the quantum dynamics of BEC (*52*) and photon blockade effect (*53*). Moreover, they could also construct three- or four- level quantum systems, which are crucial for the coherent manipulations of these states in the quantum information processing (*52, 53, 58*). Therefore, a direct physical picture of these states is strongly desired.

However, the excited states of polariton in MC has been hardly understood and there are only few reports in literature such as the attempt using Terahertz pump-probe in the III-V quantum well system and Rydberg polariton states in proverskite. The challenges in study of polariton excited states are twofold: i) the excited states of polariton are usually too broadened and too weak to observe due to the excitonic many-body effect and ii) the most excited states cannot be accessed by the usual linear optical spectroscopy due to the different selection rule rooted from transition symmetry. Therefore, it is important and needed to elucidate the excited states of polariton for both fundamental light-matter interaction study and harnessing such interaction for polaritonic applications. Particularly, polaritonic excited states in monolayer TMDC in MC represents the frontier of such study, promising for exotic physics such as BEC and superfluicds at room temperature due to the large exciton binding energy and for polaritonics applications that utilize polariton as the information carrier for classic and quantum information processing.

4.3 The valley degree of freedom

The charge and spin degree of freedoms (DOF) of electrons and holes are the underlying key elements and information carrier of electronics. These DOF are the basis for a wide range of applications, such as transistors, photodetectors, integrated circuits and magnetic memory devices. In the ***k*** space (momentum space) of two-dimensional (2D) hexagonal crystals, such as graphene and transition metal dichalcogenide (TMDC), when the valence band maximum and conduction band minimum occurs at the Brillouin zone corners, i.e. K points, it forms energy preferable “valleys” in the (quasi-) particle band. The broken inversion symmetry distinguishes two different kind of valleys donated as K and K’. Because they are largely separated in the ***k*** space, intervalley scattering of particle is unlikely to happen. Therefore, we can use valley index to label the localized particles in ***k*** space. In this sense, the valley becomes a new DOF of the particles. The valley DOF is in close analog to the spin DOF. This new DOF can be potentially used as an information carrier, just like charge and spin, in the next generation electronics – valleytronics.

In monolayer TMDC of 2H structure, the inversion symmetry is broken and thus it provides a perfect system to explore the enabled valley DOF. Unlike in graphene where spin-orbital coupling is extremely weak, here in the TMDC the spin-orbital is strong because of the *d* orbitals of the transition metal atoms, which causes a large spin splitting in the valence bands of monolayer. The strong spin-orbital coupling together with the inversion symmetry broken gives rise to coupled spin and valley properties (*65*). One of the consequence is that the spin and valley relaxation at the valence-band edges are suppressed because flipping of each index alone is forbidden by the large valley contrasting spin splitting (0.1-0.5 eV), which implies long spin and valley lifetime of hole states. Also, the valley and spin dependent optical selection rules can be used to optically excite particles of desirable spin and valley. Figure 4.3.1 shows the crystal structure and schematic band structure of monolayer 2H MoS_2.

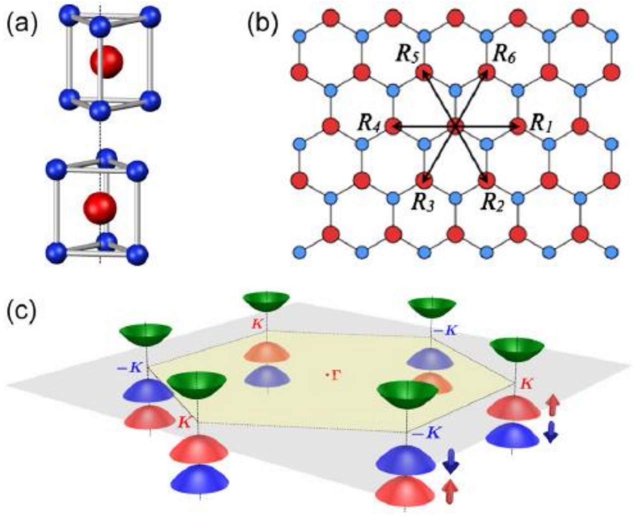

Figure 4.3.1 | (a) Unit cell of bulk 2H MoS_2. (b) Top view of MoS_2 monolayer. (c) Schematic of the band structure with the K points, spin splitting and valley spin coupling. From Ref. (*65*).

Lately discovered EP in monolayer transition metal dichalcogenides (TMD) offer a novel testbed to explore the EP quantum states with new valley degree of freedom (DOF) (*55*, *56*, *66*–*68*). TMD monolayers are an attractive group of direct-gap two-dimensional (2D) semiconductors (*69*, *70*). The 2D TMD excitons possess large binding energy (up to ~0.7 eV) (*71*, *72*), huge oscillator strengths (*69*, *71*), and new valley DOF (*73*–*75*). By placing the 2D excitons in cavities, robust EP can be formed at room temperature (*66*, *76*, *77*), and strikingly found to be equipped with valley DOF (*76*–*79*). This valley DOF inherited from the exciton constituent provides a unique perspective to unravel the physical properties of EP excited states and track down the valley-correlated electrodynamics.

4.4 Schematics of the experiment

We directly probe the valley-dependent EP excited states in a 2D semiconductor, beyond conventional studies on the ground states. We elucidate these states via two-photon photoluminescence excitation (TPE) and second harmonic generation (SHG) spectroscopy with the underlying optical selection rule, by utilizing three outstanding advantages. First, the large exciton binding energy facilitates the spectroscopic identification of quantum states of 2D EP (*64*, *72*, *80*); second, the valley DOF provides a unique quantum mark to monitor these states (*73*–*78*); third, the broken inversion symmetry in TMD monolayers results in strong SHG signals acting as an instantaneous process to probe metastable states (*64*, *80*).

The experimental approach is outlined in the schematic of Figure 4.4.1. Figure 4.4.1a shows the microcavity (MC) sample structure. It consists of bottom and top distributed Bragg reflectors (DBRs), and a cavity composite layer where a monolayer of WS_2 is sandwiched between two hydrogen silsesquioxane (HSQ) layers as well as a protection layer of Al_2O_3. The nonlinear spectroscopy approach is via excitation with normal incident two-photon pump and detecting signals at angular far field with circular polarizations. Figure 4.4.1b depicts the energy diagram of valley EP. The optical transitions of K(K') valley excitons in monolayer WS_2 can be enabled by left (right) circularly polarized $\boldsymbol{\sigma}^+$ ($\boldsymbol{\sigma}^-$) light. When such excitons are strongly coupled to a planar MC, the EP with valley DOF (*76*–*79*) leads to two degenerate sets of energy bands labeled as K and K'. In each set, the excitonic 1s states couple to cavity photon mode and form two anti-crossed bands of upper polariton (UP) and lower polariton (LP) branches. The excitonic dark 2p states cannot directly couple with one-photon but could transfer to lower states, acting as the higher energy band (*57*, *64*, *72*, *81*). For the ultrafast transitions and coherent correlations among these states, the lowest band LP is taken as the ground states, the dark 2p states and the UP as two typical kinds of EP excited states (*57*). These excited states could quickly relax to the LP and emit circularly polarized photons. The 2p states are optically forbidden in linear spectroscopy (*61*). As shown in Figure 4.4.1c, the UP are optically allowed but thermodynamically unstable (*59*), and thus are difficult to be probed in fluorescence approach. The UP-resonant SHG instantaneously emits out through UP states. SHG emission shows opposite helicity of pump photons due to the angular-momentum conservation. In this context, we successfully probe the dark 2p states by TPE based on the nonlinear selection rule. When the two-photon pump is resonant with UP, instantaneous SHG reaches the dynamically unstable UP. By monitoring polarization dependence, we are able to uncover the physical properties of EP excited states with valley DOF.

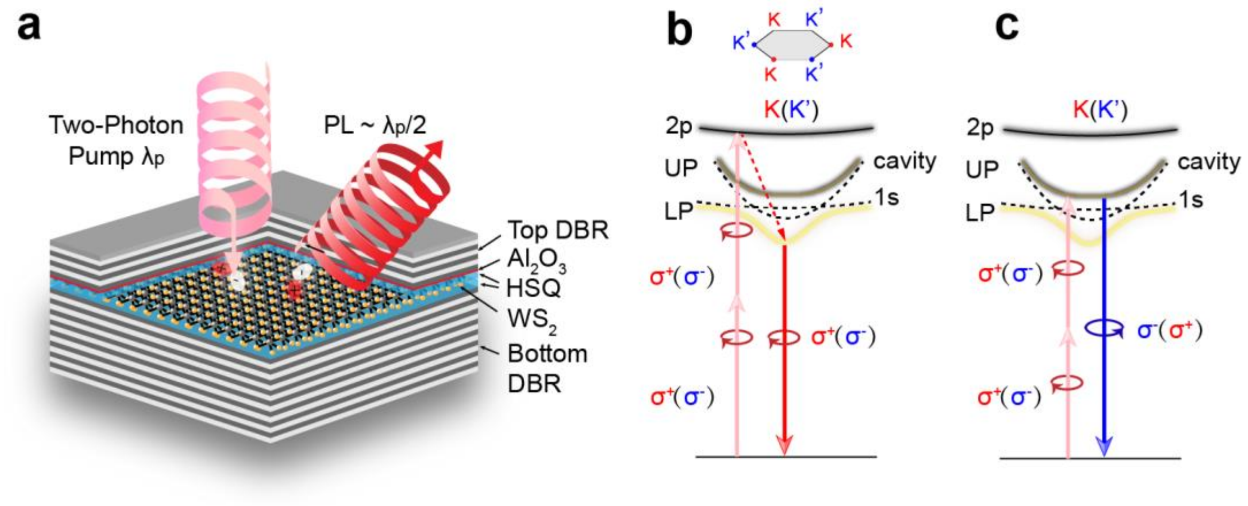

Figure 4.4.1 | Schematics of sample structure and energy diagram of valley exciton polariton (EP) quantum states.

4.5 Sample fabrication

An all-dielectric microcavity (MC) embedded with monolayer WS_2 (Figure 4.4.1a) is studied for our demonstration. The MC consists of a bottom mirror (DBR of 15.5 pairs of Nb_2O_5/SiO_2), a top mirror (DBR of 7.5 pairs of Si_3N_4/SiO_2) and a cavity composite layer, which includes an exfoliated monolayer WS_2, two sandwiching layers of HSQ and a capping layer of Al_2O_3. A single-crystal silicon (100) wafer with deep etched markers (35 um deep) is first pre-cleaned by a Piranha solution. The bottom DBR is then deposited via ion beam sputtering (Veeco IBS) at a temperature of 120 ºC with a pressure of < $5\times10_{-5}$ Torr. The sputtering rate is set to be ~0.1 nm/s to achieve ultrahigh flatness and > 99.95% reflectivity with a centre wavelength of 625 nm and stop band width of ~200 nm. Since the monolayer WS_2 would be degraded at high temperature, the top DBR is fabricated by plasma enhanced chemical vapor deposition (PECVD) at a temperature of 350 ºC.

The cavity layer structure is very crucial to maintain the high excitonic performance of monolayer WS_2. Here the monolayer WS_2 (2D Semiconductor, Inc.) is directly exfoliated onto a PDMS stamp and then transferred to DBR substrates via dry transfer method (Figure 4.5.1 left). We have selected HSQ as the sandwiching layers to enhance the excitonic performance. The HSQ was first spin-coated onto the substrate, and then the spin-coated thin films are crosslinked into amorphous SiO_2 via thermal annealing at 400 ºC in Ar environment. The thicknesses for the bottom and top HSQ layer are controlled to be 105 nm and 90 nm, respectively. To prevent the damage from the plasma environment during the PECVD growth, another 5 nm thermal Al_2O_3 is deposited onto the top HSQ layer by atomic layer deposition (ALD) at 200 ºC. With the cavity layer structure design, the MC in this work forms a total λ/2 cavity with electric field distribution sharply peaked at the location of WS_2 monolayer.

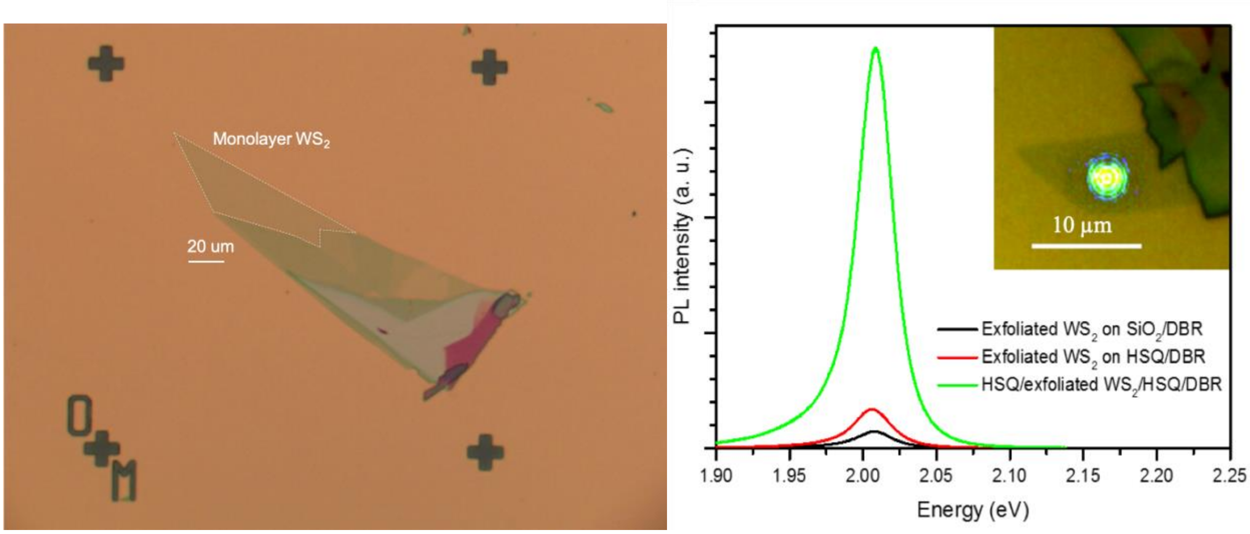

Figure 4.5.1 | Optical image of a typical transferred monolayer WS2 on HSQ/DBR substrate (left) and typical PL enhancement comparison (right, adopted from Ref. (*82*)).

4.6 The strong coupling regime

In order to access these excited states, the strong coupling regime is demonstrated in this monolayer WS_2 cavity and the corresponding EP photoluminescence (PL) is observed at different pump conditions. For clarity, the data are collected at 80K unless otherwise stated. To determine the strong coupling regime, k-space (angle-resolved) reflectivity map of white light is carried out. Figure 4.6.1a shows the k-space (angle-resolved) reflectivity map. The reflectivity modes of white light are revealed at dark areas of the map with coordinates of photon energy versus sine of angles (θ). The dashed line represents the exciton A 1s states (ex_A) at 2.075 eV and the dashed curve as the cavity photon modes. The grey color scale represents the reflectivity. Two distinct anti-crossing modes at the darker areas are clearly revealed and identified as the UP and LP. To confirm the formation of EP, a coupled oscillator model is fitted with UP and LP as the solid grey and orange curves, respectively.

The polariton dispersion can be modelled using a coupled oscillator model (*52*, *83*)

$$\begin{pmatrix} E_{ex} + i\hbar\Gamma_{ex} & V_A \\ V_A & E_{cav}(\theta) + i\hbar\Gamma_{cav} \end{pmatrix} \begin{pmatrix} \alpha \\ \beta \end{pmatrix} = E \begin{pmatrix} \alpha \\ \beta \end{pmatrix}. \tag{4.6.1}$$

Here the cavity mode was determined as $E_{cav}(\theta) = E_{ph}/\sqrt{1-(\sin\theta\,/n_{eff})^2}$ with cutoff photon energy E_{ph} and effective refractive index n_{eff} of the cavity layer. E_{ex} is the exciton energy. The Γ_{cav} and Γ_{ex} are the half width half maximum (HWHM) of cavity photon and exciton, respectively. E are the eigenvalues corresponding to the energies of polariton modes. α and β construct the eigenvectors. V_A is the coupling strength. The eigenvalues are:

$$E = \left(\frac{E_{ex}+E_{cav}}{2}\right) + i\left(\frac{\hbar\Gamma_{ex}+\hbar\Gamma_{cav}}{2}\right) \pm \sqrt{V_A^2 + \frac{1}{4}(E_{ex}-E_{cav}+i\hbar\Gamma_{ex}-i\hbar\Gamma_{cav})^2} \quad (4.6.2)$$

where $\hbar\Omega_{Rabi} = 2\sqrt{V_A^2 - \frac{1}{4}(\hbar\Gamma_{ex}-\hbar\Gamma_{cav})^2}$ as the Rabi splitting at detuning $\Delta = E_{cav} - E_{ex} = 0$. As V_A^2 dominates in the square root part in this work. The splitting-to-linewidth ratio (SLR) can be represented as $SLR = \frac{\hbar\Omega_{Rabi}}{2\Gamma_{polariton}} \approx \frac{V_A}{\Gamma_{polariton}}$ where $\Gamma_{polariton}$ is the HWHM of polaritons. The interaction rate can be represented by V_A and the polariton decay rate can be determined by the HWHM $\Gamma_{polariton}$, one can understand SLR as the ratio of the interaction rate to the polariton decay rate. A Rabi splitting of 41.6 meV and a large splitting to linewidth ratio of >3.3 are also obtained, in consistency with previous report (*84*).

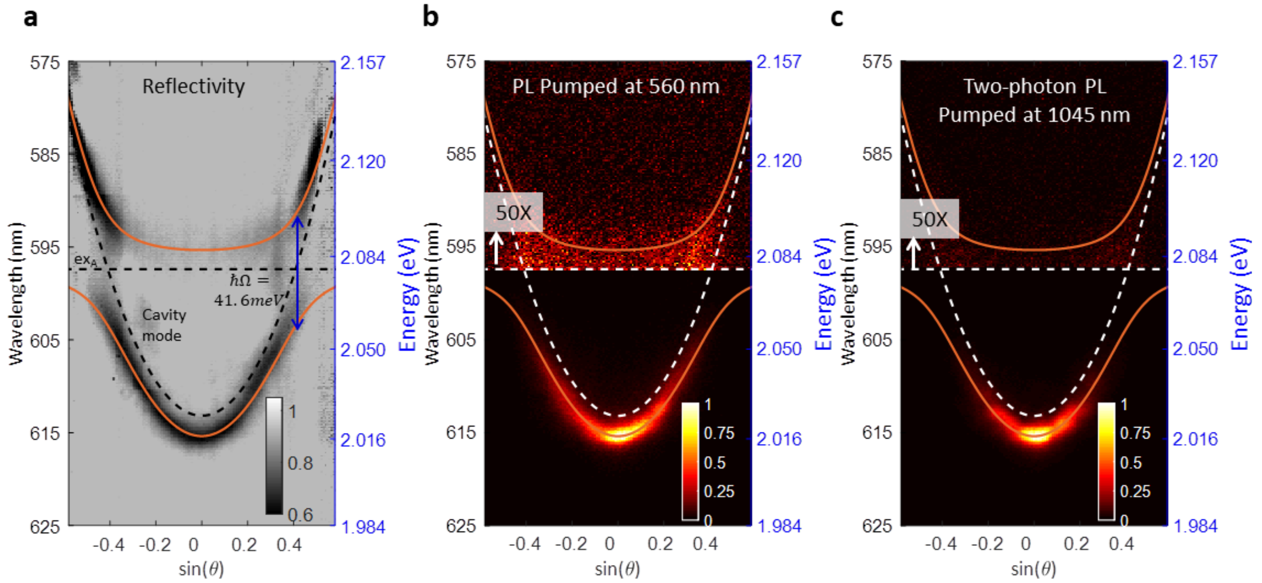

Figure 4.6.1 | Determination of the strong coupling regime via k-space reflectivity and photoluminescence (PL) at 80K.

To observe the fluorescence, the EP are firstly pumped by a pulsed laser of 560 nm, which lies on the edge of the cavity side band. The ground state LP is dominant while the UP becomes visible as magnified by 50 times as in Figure 4.6.1b, suggesting fast thermal relaxation from UP to LP. The color scales represent the normalized intensity. The PL dispersion also shows excellent agreement with the extracted reflectivity dispersion from Figure 4.6.1a. More importantly, the EP could also be observed by TPE fluorescence (Figure 4.6.1c). The TPE can get access to the 2p dark states by pumping at 1045 nm, whose two-photon energy is close to the resonance of 2p states (*64, 72, 85*). Remarkably, the TPE shows prominent k-space fluorescence map, similarly to the case of linear pump at 560nm. The LP is still dominant while UP is also magnified by 50 times for better visibility, and this dispersion is consistent with the reflectivity dispersion. This observation strongly suggests that the 2p resonance corresponds to one of EP excited states. This excited state could inherit physical properties from the pure exciton constituent and take a direct transition channel to the optically allowed EP states and finally relax at ground state LP.

4.7 Valley-polarized two-photon excitation fluorescence

To examine the physical properties of the 2p excited states and the transition mechanism to LP ground states, the valley-polarized TPE is performed. Here we focus on the ground state (LP) emission polarization as an efficient indicator for the valley properties and transition process (*73–75*). When pumped with $\boldsymbol{\sigma^+}$ (left circular) polarization at 1045 nm, k-space fluorescence map is detected at both $\boldsymbol{\sigma^+}$ and $\boldsymbol{\sigma^-}$ polarizations (Figure 4.7.1a). Clearly the $\boldsymbol{\sigma^+}$ TPE fluorescence has much stronger intensity than $\boldsymbol{\sigma^-}$ one, implying the inherited valley DOF (*64*). To analyze the valley dependence, the emission helicity (h) is defined as

$$\boldsymbol{h = \frac{I(\sigma^+) - I(\sigma^-)}{I(\sigma^+) + I(\sigma^-)} \times 100\%} \tag{4.7.1}$$

A k-space helicity map in Figure 4.7.1b is extracted from Figure 4.7.1a, where a uniform valley helicity about 20% is obtained along the LP band. When the pump is switched to the $\boldsymbol{\sigma^-}$ polarization, the TPE fluorescence contrast of $\boldsymbol{\sigma^+}$ and $\boldsymbol{\sigma^-}$ is reversed and a k-space helicity map with about -20% helicity is obtained in Figure 4.7.1c. For comparison, the helicity maps with a linear pump at 560 nm only show optical helicity of 8%. The two-photon energy of 1045 nm pump (~2.373 eV) is much more off-resonance of exciton 1s state (2.075 eV) than the one-photon energy of 560 nm pump (2.214 eV). The valley helicity is reported to increase as the pump gets closer to the 1s exciton resonance for decreased inter-valley scattering (*75, 80*). In contrary, here the higher helicity at TPE suggests the resonance with dark 2p states. Moreover, it also implies an ultrafast relaxation channel from 2p states to LP to preserve the valley DOF, similar to the bare valley exciton case (*64*). Therefore, this valley dependence clarifies the correlation between dark 2p states and LP. Note that no obvious angular dependence of optical helicity is observed, since the helicity is determined by the relaxation dynamics (*77*, *86*) rather than polariton composition as suggested in recent reports (*76*, *78*).

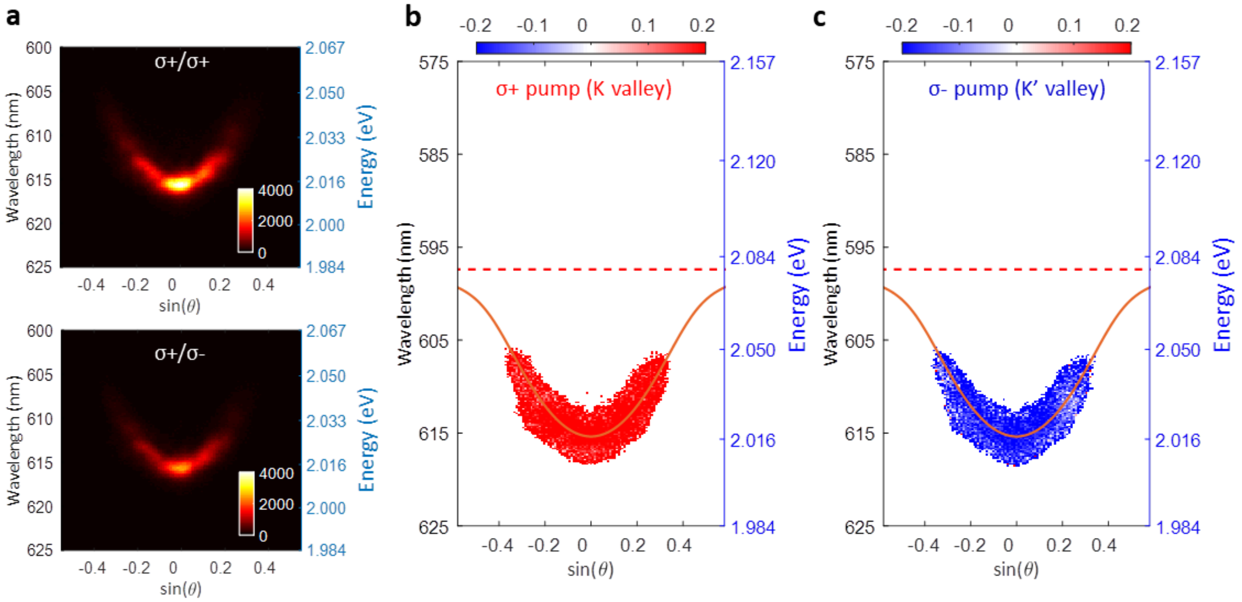

Figure 4.7.1 | Observation of TPE valley-dependent helicity at 80K. a, Polarization-resolved k-space TPE fluorescence maps by 1045 nm pump with $\boldsymbol{\sigma}^{+}$ polarization. b, The TPE helicity map extracted from $\boldsymbol{\sigma}^{+}$ pump in a. c, The TPE helicity map with $\boldsymbol{\sigma}^{-}$ pump at 1045nm. In both b and c, the orange solid lines represent the LP dispersion and the dashed lines as the ex_A.

4.8 TPE resonance of the excited 2p states

Notably, valley-polarized TPE spectroscopy is carried out to illustrate the resonance of 2p states. The excitation wavelength is scanned to two-photon energy close to UP. Figure 4.8.1a shows the integrated intensity (black) and maximum helicity (blue) as functions of the TPE pump wavelength. Both the peaks in the intensity and helicity emerge at the effective two-photon wavelength around ~522 nm, corresponding to the resonance of dark 2p states, unveiling spectroscopic signature of this excited state. Moreover, similar experiments at other temperatures up to RT are also carried out. Figure 4.8.1b shows the temperature dependence of the TPE resonance peak position (upper panel, error bars from peak fitting), linewidth (middle panel), and maximum helicity (lower panel, error bars are from multiple measurements). All the error bars are from multiple measurements, and also from peak fitting for linewidth. As temperature increases, both the TPE resonance and 1s exciton peak (control sample of bare WS_2) positions show similar trend of redshift, which is consistent with previous reports (*72*, *85*). The linewidth gradually increases at higher temperature due to stronger scattering process and faster thermal relaxation (*72*, *77*). While these processes depolarize TPE fluorescence helicity to about zero at RT, the 2p intensity peak survives at RT suggesting the direct transitions from excited states 2p to EP are robust up to RT though the intervalley scattering may become significant. As temperature increases, the helicity decreases as the excitonic fraction of EP increases, confirming that the relaxation thermodynamics primarily affects the valley dependence (*77*, *86*).

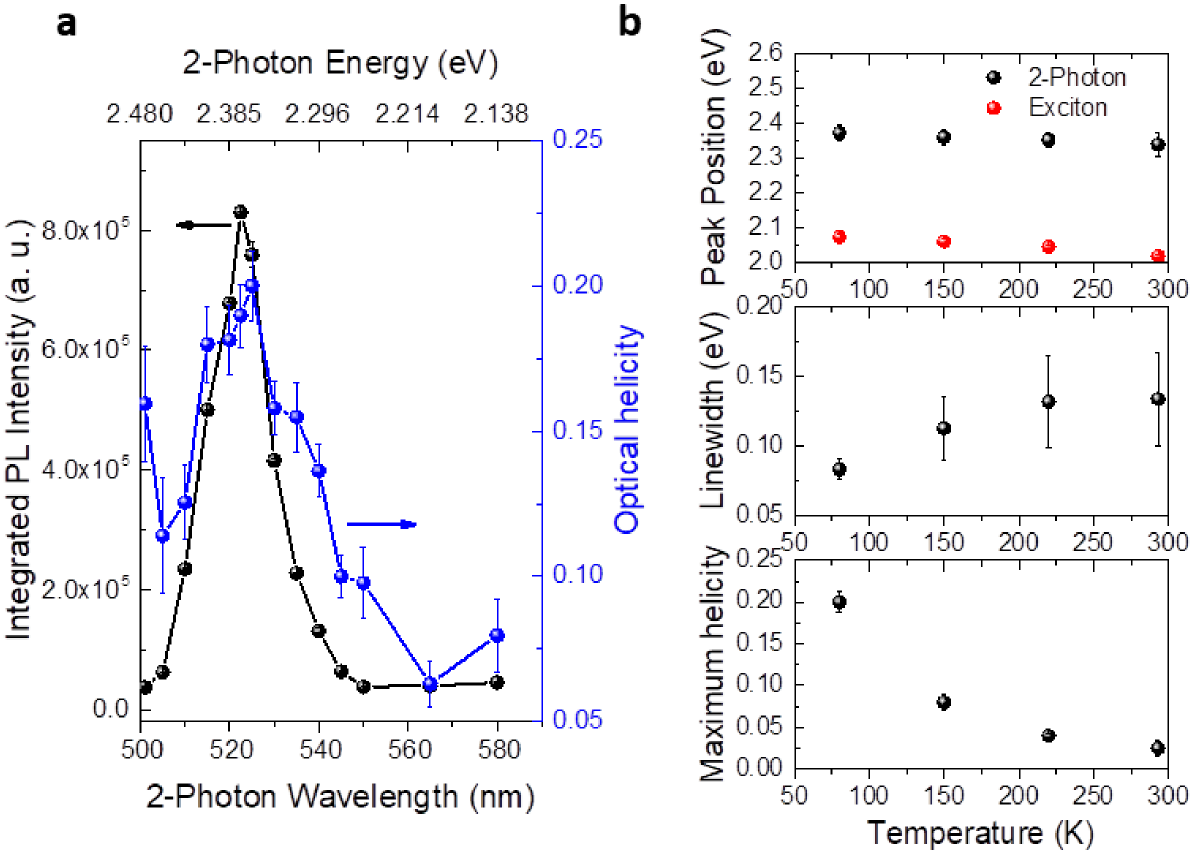

Figure 4.8.1 | Revealing the TPE resonance of 2p states and its temperature dependence.

4.9 Upper polariton-resonant SHG

Meanwhile, we also directly probe UP with valley DOF by polariton-resonant SHG. As another typical excited state of EP, UP is a coherent state lifted up by the Rabi splitting but with much weaker emission (Figure 4.6.1), because of hybrid composition of UP and the thermodynamic relaxation from UP to LP (*59*). When pumped at 1190 nm, the TPE is far off-resonance from 2p state and is thus forbidden. There is still weak leakage emission from forbidden excitation (much weaker emission from UP than from LP) (*64*) by detecting with the same polarization of pump as in Figure 4.9.1a. However, when the emission is detected with the opposite polarization of pump, the UP shows brighter intensity by orders of magnitude around $\mathbf{sin}(\boldsymbol{\theta}) = \mathbf{0}$ as in Figure 4.9.1b. In Figure 4.9.1a and Figure 4.9.1b, the dispersion diagrams are translated from Figure 4.6.1, and the color bars represent the intensity. Note here the whole map in Figure 4.9.1a and LP in Figure 4.9.1b are magnified by 15 times for better visibility. The extracted helicity map for $\boldsymbol{\sigma}^{-}$ pump in Figure 4.9.1c (vice versa for $\boldsymbol{\sigma}^{+}$ pump) shows a near unity opposite helicity for UP but close to zero helicity for LP, where the color bar represents the helicity. Due to the inversion symmetry breaking and the conservation of angular momentum with the valley angular momentum, this bright UP emission with opposite helicity is actually from the resonant SHG, which is an instantaneous process and not limited by the fast dynamics of UP (*64*, *80*, *87*). Moreover, we find the SHG spectroscopy shows consistent intensity and helicity resonances with UP, the resonance peaks blueshift as temperature increases up to 297K without extinct helicity, confirming that SHG is an instantaneous process disregarding polariton thermodynamics. In consistency, we also observe similar helicity dependence of LP-resonant pump SHG. Therefore, the polariton-resonant SHG provides a universal approach to probe any polariton states without influence by the dynamic instability.

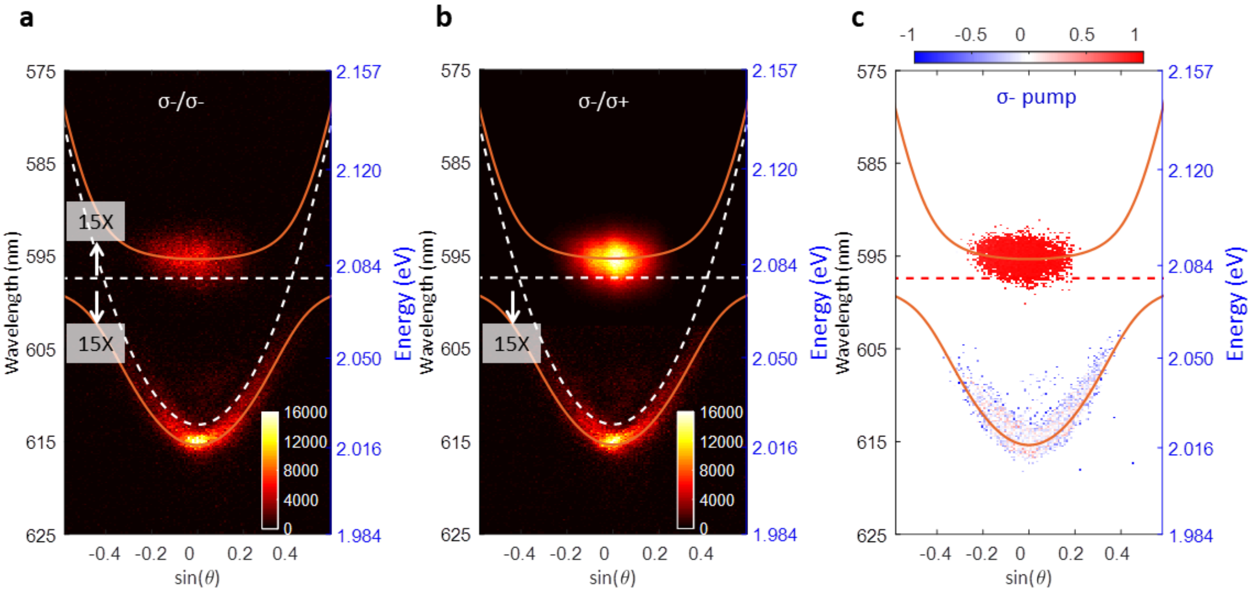

Figure 4.9.1 | Probing the UP with valley DOF by resonant SHG.

4.10 Conclusion and outlook

In conclusion, the excited states of EP in a monolayer TMD are revealed via TPE and SHG spectroscopy. Based on the spectroscopic analysis and polarization dependence in these states, the transition process and valley dynamics in 2D EP are also resolved. This study represents the first step towards a clear understanding of EP excited states. The valley-dependent excited states of 2D EP promise the feasibility of valley BEC and chiral superfluidity (*56*, *68*). Moreover, the transitions from EP excited states to ground state raises many possibilities in chiral terahertz photonics and coherent quantum manipulation of exciton polaritons (*52*, *55*, *61*), as well as nonlinear control in valleytronics (*64*, *68*, *80*, *87*).

Remark: Chapter 4 includes co-authored materials from Xiaoze Liu*, Jun Yi*, Quanwei Li*, et. al. " Nonlinear optics at excited states of exciton polaritons in two-dimensional atomic crystals (submitted)" (*contributed equally).

5 Physics of quantum metasurface: a unique beam-splitter for optical quantum interference

5.1 Introduction

Metamaterials, the structured materials with subwavelength elements, enable beyond-nature electromagnetic responses and applications such as negative refractive index, super resolution imaging and invisible cloaking (*88–91*). Metasurfaces, the two-dimensional counterpart of metamaterials, allow us to arbitrary tailor the wave front and propagation of classical light in an unprecedented flat optics fashion (*92–96*). On the other hand, quantum optics has been a leading platform for quantum computation and quantum communication due to the superb properties of photons such as long coherence time, room-temperature operation, easy manipulation and light-speed propagation (*97–101*). Consequently, exciting possibilities could emerge by marrying the capability of metamaterials and the power of quantum optics. In this context, metamaterials were used to test quantum foundation (*102*) and recent works used metasurfaces for entanglement generation (*103*), quantum state reconstruction (*104*), as well as interferometry (*105*). However, in all these cases, metamaterials or metasurfaces themselves functioned either classically or did not produce new quantum phenomenon except simplifying the traditional bulky and/or complex optic components. Therefore, it is still an important open question whether metamaterials or metasurfaces can enable new regimes in quantum optics.

In this and the next chapters, we propose and experimentally demonstrate that metasurface rotation enables a new degree of freedom in optical quantum interference through its unique anisotropic coefficients of transmission and reflection, which is impossible before. We show that the output of two-photon interference can be dynamically controlled at will to be bunching (boson-like attractive behavior) or split (fermion-like repulsive behavior) or arbitrarily intermediate state, by simply rotating the metasurface. Our metasurface opens a door for both fundamental quantum photon-photon interaction and the development of future optical quantum technologies.

In this chapter, we present the theory of quantum interference and design of the metasurface beam-splitter. The experiments of quantum two-photon interference at such metasurface will be discussed in next chapter.

5.2 The HOM effect, bosonic and fermionic quantum interference

The quantum two-photon interference (TPI) at beam-splitter (BS) plays the central role in optical quantum information processing such as linear optics (*97*), boson sampling (*106*, *107*) and quantum walks (*108*), because it produces the indispensable effective photon-photon interaction between otherwise non-interacting photons. Specifically, when two identical single photons incident on a conventional 50:50 BS, the TPI manifests itself as the hallmark Hong-Ou-Mandel (HOM) effect (*109*) such that the two photons always bunch and exit the BS from the same output port in an entangled state (Figure 5.2.1). Such quantum interference comes from the delicate addition of complex amplitudes of alterative quantum paths that critically depends on their relative phase.

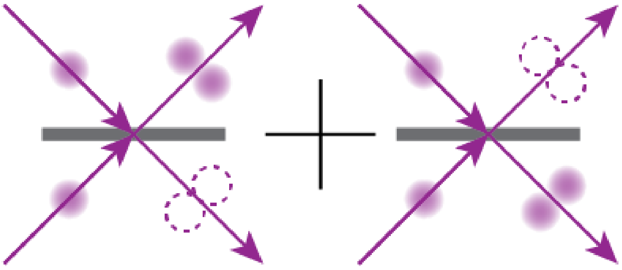

Figure 5.2.1 | Bunched entangled state in two-photon interference at conventional 50:50 beam-splitter

To see why, let us have a closer look at what happens at the beam-splitter as illustrated in the Figure 5.2.2 below. Suppose two identical single particles, both bosons or fermions, incident simultaneously at two different input ports of a conventional lossless 50:50 beam-splitter, labeled as port 1 and port 2, respectively. The BS operation can be described as

$$BS = \begin{bmatrix} t & r \\ r & t \end{bmatrix} = \frac{1}{\sqrt{2}} \begin{bmatrix} 1 & i \\ i & 1 \end{bmatrix}. \quad (5.2.1)$$

Here the BS is assumed to be symmetric, which is only for the convenience of discussion and will lead to the same final conclusion as asymmetric. Each of the two particles can be either transmitted or reflected by the BS. Therefore, there are in total four different cases or quantum paths. That is, both particles get transmitted, both get reflected, one gets reflected while the other gets transmitted and vice versa. Note that the first two cases enclosed in the dashed box lead to the same final configuration that there is one particle in each output port 3 and 4. These two cases cannot be distinguished by experimental measurements because of the indistinguishability of the two photons.

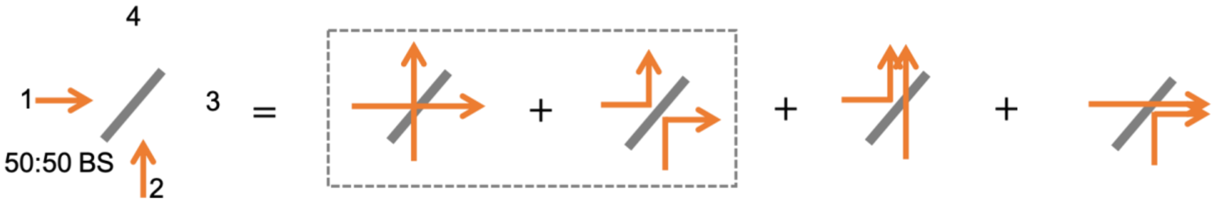

Figure 5.2.2 | Two-particle interference at conventional 50:50 beam-splitter.

To obtain the measurement probability of this configuration, as denoted as $P(1_3, 1_4)$, we need to first add the complex amplitudes of the two cases, then calculate the modulus of the sum and the square of the modulus, according to the principle of quantum mechanics as discussed in the first chapter of the third volume of Feynman's Lectures on Physics. Additionally, there is another phase factor between the two amplitudes comes from the permutation symmetry of the particles, which is 1 for bosons while -1 for fermions. Finally, we reach to the results in Table 5.2.1 below, where we also include the probabilities for the other two configurations that both particles exist the BS in the same output port, denoted as $P(2_3, 0_4)$ and $P(0_3, 2_4)$, respectively. The probabilities for two classical distinguishable particles are also included for comparison.

Quantum statistics of the two particles	$\boldsymbol{P(1_3, 1_4)}$	$\boldsymbol{P(2_3, 0_4)}$	$\boldsymbol{P(0_3, 2_4)}$
Bosonic	$\left\lvert\frac{1}{\sqrt{2}} \times \frac{1}{\sqrt{2}} + \frac{i}{\sqrt{2}} \times \frac{i}{\sqrt{2}}\right\rvert^2 = 0$	$\frac{1}{2}$	$\frac{1}{2}$
Fermionic	$\left\lvert\frac{1}{\sqrt{2}} \times \frac{1}{\sqrt{2}} - \frac{i}{\sqrt{2}} \times \frac{i}{\sqrt{2}}\right\rvert^2 = 1$	0	0
Classical	$\left\lvert\frac{1}{\sqrt{2}} \times \frac{1}{\sqrt{2}}\right\rvert^2 + \left\lvert\frac{i}{\sqrt{2}} \times \frac{i}{\sqrt{2}}\right\rvert^2 = \frac{1}{2}$	$\frac{1}{4}$	$\frac{1}{4}$

Table 5.2.1 | The output probabilities of two-particle interference at a conventional lossless BS.

As we see from the table above, for bosons the $P(1_3, 1_4)$ vanishes due to the destructive interference of the two cases, while for fermions $P(1_3, 1_4)$ reaches to unity, or double of the classical value, due to the constructive interference of the two cases. As a result, compared with the equal probabilities of the four cases for classical particles, bosons lead to a higher probability that the two particles bunch together, which can be viewed as an effective attractive interaction between the two bosons. Whereas, fermions have a higher probability that they split, consist with Pauli exclusion principle, which can be viewed as an effective repulsive interaction.

Alternatively, we can track down the two-particle quantum state as it been transformed by the BS operation. We label the four ports of the BS by the corresponding annihilation operators a_i for bosons and b_i for fermions, where $i = 1, \dots, 4$ as shown in the Figure 5.2.3 below.

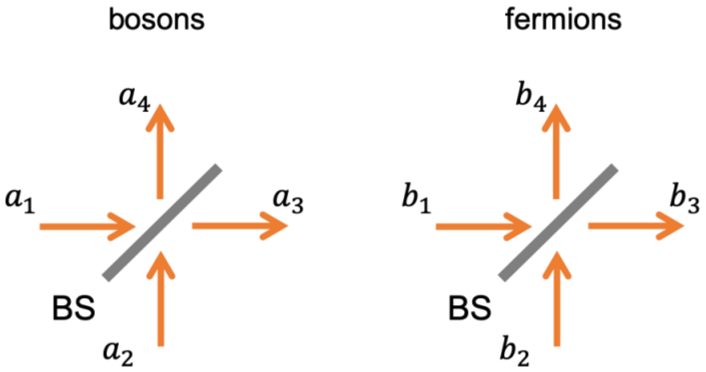

Figure 5.2.3 | The four ports of a BS with annihilation operators labeled for bosons and fermions.

The annihilation operators are transformed by the BS as following.

$$\begin{pmatrix} a_3 \\ a_4 \end{pmatrix} = \begin{bmatrix} t & r \\ r & t \end{bmatrix} \begin{pmatrix} a_1 \\ a_2 \end{pmatrix} = \frac{1}{\sqrt{2}} \begin{bmatrix} 1 & i \\ i & 1 \end{bmatrix} \begin{pmatrix} a_1 \\ a_2 \end{pmatrix} \tag{5.2.2}$$

$$\begin{pmatrix} b_3 \\ b_4 \end{pmatrix} = \begin{bmatrix} t & r \\ r & t \end{bmatrix} \begin{pmatrix} b_1 \\ b_2 \end{pmatrix} = \frac{1}{\sqrt{2}} \begin{bmatrix} 1 & i \\ i & 1 \end{bmatrix} \begin{pmatrix} b_1 \\ b_2 \end{pmatrix} \tag{5.2.3}$$

The transformation for creation operators is obtained by taking the complex conjugate of above equations. On the other hand, the critical difference between bosons and fermions are revealed by their canonic commutation relations. For bosons, the commutator requires

$$[a_i\ , a_j^\dagger] \equiv a_i\ a_j^\dagger - a_j^\dagger a_i\ = \delta_{ij}, \tag{5.2.4}$$

$$[a_i\ , a_j\ ] = 0 = [a_i^\dagger, a_j^\dagger]. \tag{5.2.5}$$

Here, $\delta_{ij} = 1$, if $i = j$ and $\delta_{ij} = 0$, if $i \neq j$. For fermions, the anti-commutator requires

$$\{b_i\ , b_j^\dagger\} \equiv b_i\ b_j^\dagger + b_j^\dagger b_i\ = \delta_{ij}, \tag{5.2.6}$$

$$\{b_i\ , b_j\ \} = 0 = \{b_i^\dagger, b_j^\dagger\}. \tag{5.2.7}$$

Equation (5.2.7) leads to $b_i^\dagger b_i^\dagger + b_i^\dagger b_i^\dagger = 0$ and $b_i^\dagger b_i^\dagger = 0$, that is the Pauli exclusion principle.

Now, we can work out the two-particle quantum state as it passes through the BS. For bosons,

$$\begin{aligned}
&|1\rangle_1|1\rangle_2 \\
&= a_1^\dagger a_2^\dagger\, |0\rangle_1|0\rangle_2 \\
&\xrightarrow{BS} \frac{1}{2}\left(a_3^\dagger + i\, a_4^\dagger\right)\left(i\, a_3^\dagger + a_4^\dagger\right)\, |0\rangle_3|0\rangle_4 \\
&= \frac{1}{2}\left(a_3^\dagger a_4^\dagger + i \cdot i\, a_4^\dagger a_3^\dagger + i\, a_3^\dagger a_3^\dagger + i\, a_4^\dagger a_4^\dagger\right)|0\rangle_3|0\rangle_4 \\
&= \frac{1}{2}\left(a_3^\dagger a_4^\dagger + i \cdot i\, a_3^\dagger a_4^\dagger + i\, a_3^\dagger a_3^\dagger + i\, a_4^\dagger a_4^\dagger\right)|0\rangle_3|0\rangle_4 \\
&= \frac{i}{\sqrt{2}}\left(|2\rangle_3|0\rangle_4 + |0\rangle_3|2\rangle_4\right), \qquad (5.2.8)
\end{aligned}$$

where the second last equal sign uses the commutator relation $a_3^\dagger a_4^\dagger - a_4^\dagger a_3^\dagger = 0$, which means a 0 phase factor (no sign change) under two-boson permutation. The last equal sign uses

$$a_i^\dagger a_i^\dagger |0\rangle_i = a_i^\dagger |1\rangle = \sqrt{2}\, |2\rangle. \qquad (5.2.9)$$

In contrast, for fermions,

$$\begin{aligned}
&|1\rangle_1|1\rangle_2 \\
&= b_1^\dagger b_2^\dagger\, |0\rangle_1|0\rangle_2 \\
&\xrightarrow{BS} \frac{1}{2}\left(b_3^\dagger + i\, b_4^\dagger\right)\left(i\, b_3^\dagger + b_4^\dagger\right)\, |0\rangle_3|0\rangle_4 \\
&= \frac{1}{2}\left(b_3^\dagger b_4^\dagger + i \cdot i\, b_4^\dagger b_3^\dagger + i\, b_3^\dagger b_3^\dagger + i\, b_4^\dagger b_4^\dagger\right)|0\rangle_3|0\rangle_4 \\
&= \frac{1}{2}\left(b_3^\dagger b_4^\dagger - i \cdot i\, b_3^\dagger b_4^\dagger\right)|0\rangle_3|0\rangle_4 \\
&= \frac{1}{2}\left(b_3^\dagger b_4^\dagger + b_3^\dagger b_4^\dagger\right)|0\rangle_3|0\rangle_4 \\
&= |1\rangle_3|1\rangle_4, \qquad (5.2.10)
\end{aligned}$$

where the second last equal sign uses the anti-commutator relation $b_3^\dagger b_4^\dagger + b_4^\dagger b_3^\dagger = 0$, which means a π phase factor (sign change) under two-fermion permutation, and $b_i^\dagger b_i^\dagger + b_i^\dagger b_i^\dagger = 0$ (Pauli exclusion principle). These results lead to the same probability distribution as before in Table 5.2.1.

Importantly, from the derivation, we can identify the contributions of all the phase factors for $P(1_3, 1_4)$, as clear in

$$\begin{aligned}
&P(1_3, 1_4) \\
&= \left|tt + \mathrm{Exp}\left(i\phi_{permutation}\right) rr\right|^2 \\
&= \left|1 + \mathrm{Exp}[i\left(\phi_{permutation} + 2\phi_{rt}\right)]\right|^2/4, \qquad (5.2.11)
\end{aligned}$$

where $\phi_{permutation}$ denotes the phase factor gained from two-particle permutation. Note the two phase-factor contributions from quantum particle permutation and BS cannot be separated. It is their sum that determines the action of the two-particle interference and the resulting effective particle-particle interaction.

Now, we put one detector in each of the port 3 and port 4 and measure the coincidence count probability $P(1_3, 1_4)$ as a function of the time delay of one particle, say in port 1. Figure 5.2.4 below shows the expected results for bosons and fermions. At large time delay greater than the particle coherence time $\boldsymbol{\tau}_c$, the two cases (both reflected and both transmitted) are distinguishable without quantum interference, alike classical particles, so does $P(1_3, 1_4)$. At zero time delay, however, the two cases are indistinguishable and their quantum interference leads to either vanishing $P(1_3, 1_4)$ for bosons or unity $P(1_3, 1_4)$ for fermions. The second order coherence function $g^{(2)}$ is simply the $P(1_3, 1_4)$ normalized by its classical value.

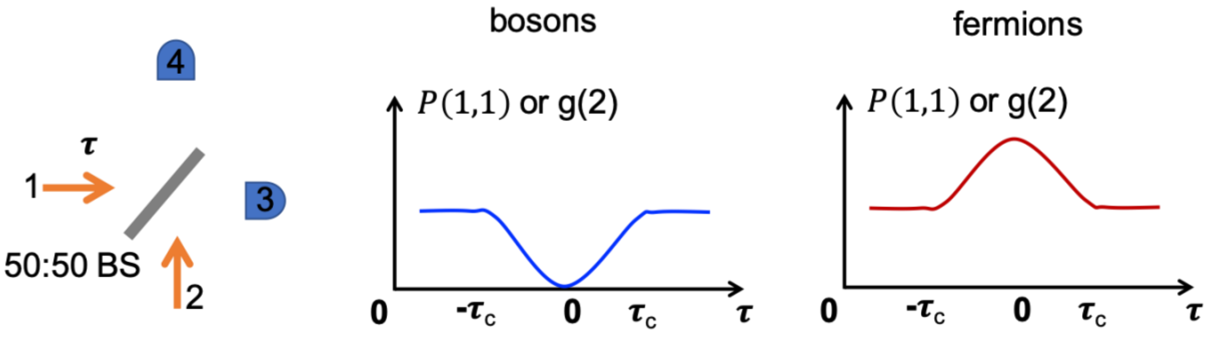

Figure 5.2.4 | $P(1_3, 1_4)$ as a function of relative particle delay for bosons and fermions.

5.3 The constrained transmission and reflection at passive beam-splitter

In last section, we assumed the BS operation to be the specific form of

$$BS = \begin{bmatrix} t & r \\ r & t \end{bmatrix} = \frac{1}{\sqrt{2}}\begin{bmatrix} 1 & i \\ i & 1 \end{bmatrix}, \tag{5.3.1}$$

which is balanced ($|t| = |r|$) and symmetric. We also see how the phase difference i between r and t plays the important role in determining the action of the quantum interference. As in any interference phenomenon, it is of great significance to be able to manipulate on-demand the phase at BS in TPI.

However, for a lossless beam-splitter, conversation of energy, or equivalently the unitarity of the BS operation, places constraints on the allowed values of t and r. Let us denote the most general BS matrix as,

$$BS = \begin{bmatrix} t1 & r2 \\ r1 & t2 \end{bmatrix}, \tag{5.3.2}$$

and $rj \equiv |rj|\mathrm{Exp}(i\phi_{rj})$ and $tj \equiv |tj|\mathrm{Exp}(i\phi_{tj})$, where $j = 1, 2$. The constraints are

$$|r1| = |r2| \equiv |r|, \tag{5.3.3}$$

$$|t1| = |t2| \equiv |t|, \tag{5.3.4}$$

$$|r|^2 + |t|^2 = 1, \tag{5.3.5}$$

$$\phi_{r1} - \phi_{t1} + \phi_{r2} - \phi_{t2} = \pi. \tag{5.3.6}$$

The last equation means the sum of the all phase differences must be π and cannot be changed. If we further assume the balanced and symmetric conditions, we will arrive at the BS matrix in Equation (5.3.1).

Clearly from Equation (5.3.6), for a passive device, loss is necessary to obtain sum of phase difference other than π. For ease of discussion and without losing generality, we assume the BS is symmetric. The general constrains allowing loss are,

$$|t|^2 + |r|^2 \leq 1 \tag{5.3.7}$$

and

$$|t \pm r|^2 \leq 1 \tag{5.3.8}$$

If we further assume the balance condition, that is $|t| = |r|$ and thus $r = te^{i\phi_{rt}}$, we will get

$$2|t|^2(1 + |\mathrm{Cos}(\phi_{rt})|) \leq 1 \tag{5.3.9}$$

which corresponds to the shadow region in the Figure 5.3.1 below. It plots $|t|$ in Y axis and ϕ_{rt}/π in X axis, which is a periodic function with period π. The two solid circles (purple color) are the only allowed values of the $|t|$ and ϕ_{rt}/π in a balanced and symmetric BS without loss. As the loss increase, the constrain on ϕ_{rt}/π gradually relaxes and it can take more and more values. It requires $|t| \leq 1/2$ for ϕ_{rt}/π to have arbitrary value. The three solid stars (red color) mark the other extreme values of ϕ_{rt}/π equals an integer. Along the two doted vertical lines (purple color), $\frac{\phi_{rt}}{\pi} =$

0.5 as in the lossless BS. Whereas, along the three dashed vertical lines (red color), $\frac{\phi_{rt}}{\pi} = 0$ (Mod 1), impossible in the lossless BS.

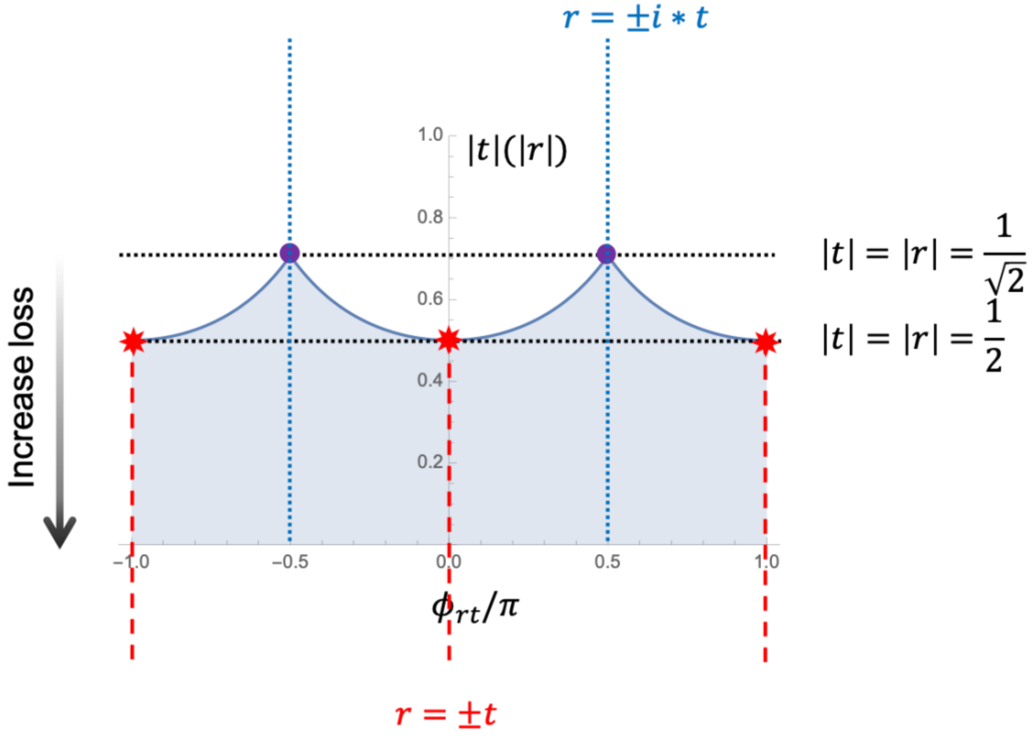

Figure 5.3.1 | The constrains on t and r for a passive BS.

5.4 Two-photon interference at a passive beam-splitter allowing loss

Now let us investigate how the two-photon interference can be changed by the relaxed constrains on the t and r at a passive BS allowing loss. It is straightforward to calculate

$$P(1_3, 1_4) = |tt + rr|^2 = 4|t|^4 \mathrm{Cos}^2(\phi_{rt}) \tag{5.4.1}$$

which is plotted in the Figure 5.4.1 below, as a function of $|t|$ and ϕ_{rt}/π. Again, we marked the most interesting points in the 3D map.

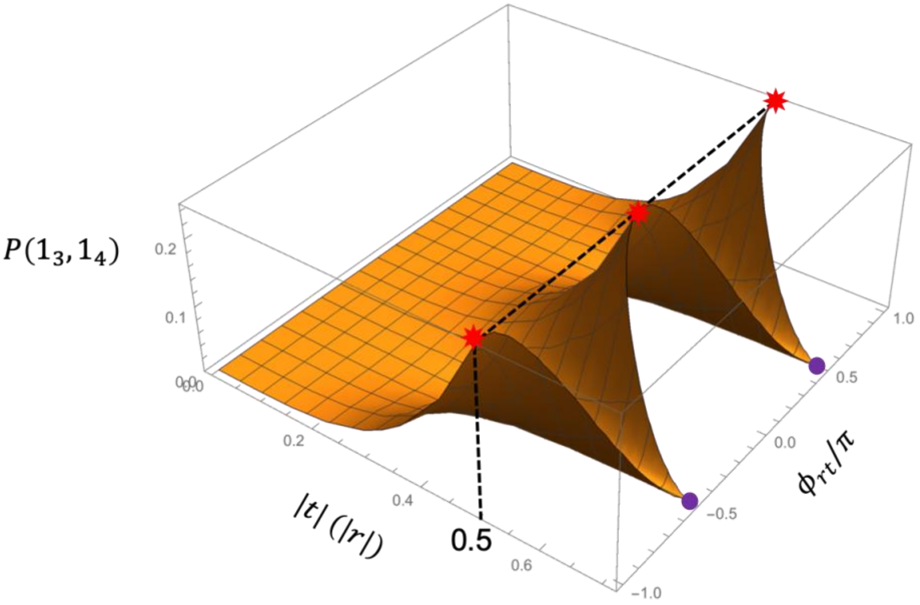

Figure 5.4.1 | $P(1_3, 1_4)$ as a function of $|t|$ and ϕ_{rt}/π for a passive BS.

We can further calculate the second order coherence function $g^{(2)}$ (Figure 5.4.2), which is simply $P(1_3, 1_4)$ normalized by its classical counterpart $P_{cl}(1_3, 1_4)$, as a function of $|t|$ and ϕ_{rt}/π. It is clear to observe that $g^{(2)}$ is a periodical function of ϕ_{rt}/π with period of π and uniform along $|t|$ due to normalization. We also mark the two extreme cases of $r = \pm t$, i.e. $\frac{\phi_{rt}}{\pi} = 0 \text{ (Mod 1)}$ and $r = \pm it$, i.e. $\frac{\phi_{rt}}{\pi} = 1/2 \text{ (Mod 1)}$. They correspond to constructive and destructive quantum interference of the two-photon amplitudes at the lossy BS, respectively. Moreover, we plot the $P(1_3, 1_4)$ as a function of photon delay $\boldsymbol{\tau}$ as we did in last section. In such imaginary experiments, the result at $r = \pm it$, i.e. $\frac{\phi_{rt}}{\pi} = 1/2 \text{ (Mod 1)}$ is the same as that for bosons on a lossless BS. Whereas, the result at $r = \pm t$, i.e. $\frac{\phi_{rt}}{\pi} = 0 \text{ (Mod 1)}$ assembles that for fermions on a lossless BS. This is exactly why photons, as intrinsic bosons, can mimic fermionic behavior at some special cases, leading to an effective repulsive photon-photon interaction, impossible in lossless BS.

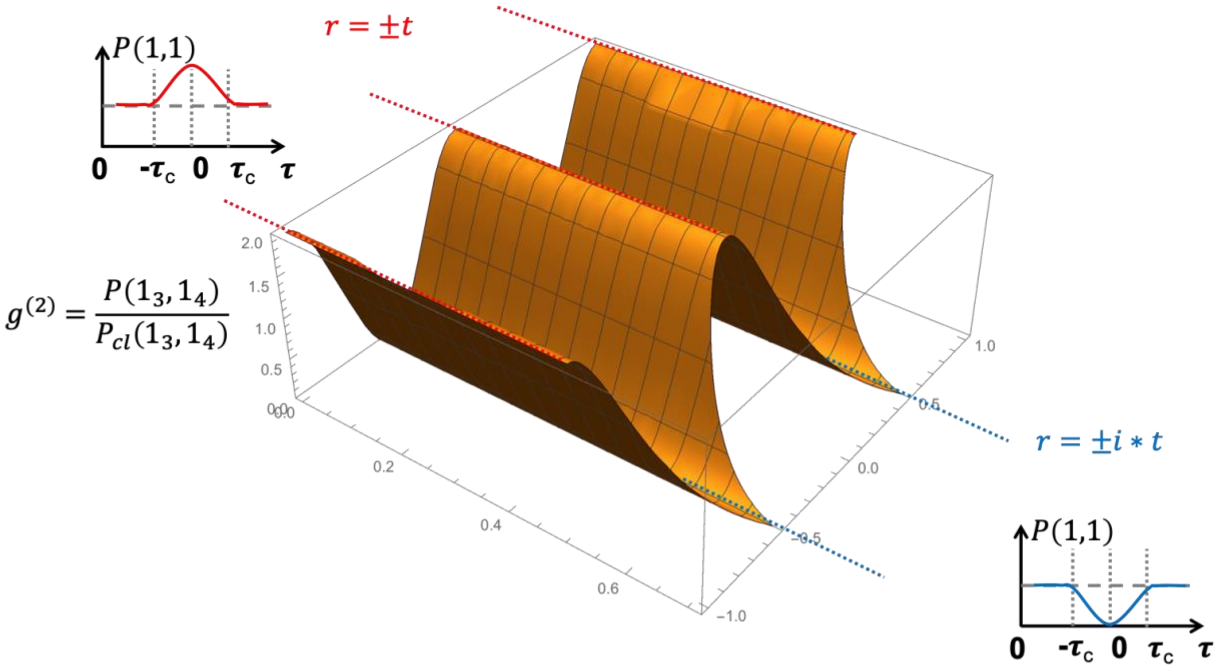

Figure 5.4.2 | $g^{(2)}$ as a function of $|t|$ and ϕ_{rt}/π for a passive BS.

Despite of the similarity, the behavior of two-photon interference at a BS with $r = \pm t$ is not exactly the same as two-fermion interference. The difference lies in the probabilities of other configurations. We summarize all the extreme cases in the Table 5.4.1 below.

Quantum statistics of the two particles & the BS relations	$\boldsymbol{P(1,1)}$	$\boldsymbol{P(2,0)}$ or $\boldsymbol{P(0,2)}$	$\boldsymbol{P(1,0)}$ or $\boldsymbol{P(0,1)}$	$\boldsymbol{P(0,0)}$
Bosonic $\boldsymbol{r = \pm i * t}$	0	1/8 (x2)	1/4 (x2)	1/4
Bosonic $\boldsymbol{r = \pm t}$	1/4	1/8 (x2)	0	1/2
Classical	1/8	1/16 (x2)	1/4 (x2)	1/4
Fermionic $\boldsymbol{r = \pm i * t}$	1/4	0	1/4 (x2)	1/4
Fermionic $\boldsymbol{r = \pm t}$	0	0	1/2 (x2)	0

Table 5.4.1 | The output probabilities of two-particle interference at a BS with 50% energy loss.

5.5 Design of the metasurface beam-splitter

We have seen in last section how the magic two-particle quantum interference work out and how an effective interaction arises between otherwise non-interacting particles. The two-photon interference (TPI) at lossless BS produces an effective attractive interaction for photons, which is used for two-photon gate in optical quantum computing. However, the controllability of such interaction in TPI is limited by the fixed phase difference between alterative quantum paths, due to the bosonic quantum statistics of photons (*110*) and the bounded response of conventional unitary BS (*111*). Thus, as in any interference phenomenon, it is of great significance to be able to manipulate on-demand the quantum phase in TPI.

In pursuing that, entanglement was used to construct such two-photon input states that are globally symmetry upon particle exchange but phase-tunable in spatial state to mimic fermionic or anyonic statistics (*112–115*). However, such approach requires extra entanglement resource in the initial input two-photon state. In addition, the mimicked quantum statistics are constrained to the global property of the two-photon state across the entire quantum network and cannot be manipulated locally at each BS, which severely limits the quantum functionality. In an alternative approach, loss was employed, indirectly or directly, to change the phase response of an effective BS (*116*, *117*). However, so far this approach is limited to either specially selected input and output states in a large number of modes (*118*, *119*) or a fixed single operation per device (*120*). Therefore, a desirable degree of freedom at BS is still missing for the phase control in TPI.

Metasurface beam-splitter (metaBS) can provide a better solution. We are looking for a metasurface that can simultaneously behave as

$$BS = \begin{bmatrix} t & r \\ r & t \end{bmatrix} = \begin{cases} |t| \begin{bmatrix} 1 & i \\ i & 1 \end{bmatrix} \\ |t| \begin{bmatrix} 1 & 1 \\ 1 & 1 \end{bmatrix} \end{cases} \tag{5.5.1}$$

for some two eigen operations. If we define

$$r \equiv |r|\text{Exp}(i\phi_r), \tag{5.5.2}$$

$$t \equiv |t|\text{Exp}(i\phi_t), \tag{5.5.3}$$

and

$$\phi_{rt} \equiv \phi_r - \phi_t. \tag{5.5.4}$$

Then, Equation (5.5.1) means

$$|r| = |t| \tag{5.5.5}$$

and

$$\phi_{rt} = \begin{cases} \pi/2 \\ 0 \end{cases} \tag{5.5.6}$$

for the two eigen operations. The most convenient way to realize this is utilizing an anisotropic phase response depending on the relative angle between the metasurface structure and light polarization.

Having the target metaBS property in mind, we use full wave finite element simulation (COMSOL) to search its structure. Very few ideal designs are found after thousands of trials. Finally, we designed the metaBS to be an array of subwavelength strips of ultrathin three-layer Cr-MgF_2-Cr structure (Figure 5.5.1), because of its robust performance and reliable fabrication. At given polarization, for example P wave, and incident angle of input light, the metaBS behaves as amplitude balanced but phase different when the strips are parallel or perpendicular to the incident plane (X-Z plane) defined by the light wavevector and the metaBS surface normal (z' axis). In former case, the metaBS essentially acts as a half Cr-mirror, where the phase difference between the reflection coefficient and transmission coefficient is zero (i.e. $\phi_{rt} = 0$). In the latter case, the metaBS introduces a $\phi_{rt} = \pi/2$ phase difference between r and t. Such unique anisotropic phase response defines two distinct eigen operations of the metaBS as below,

$$BS = \begin{bmatrix} t(\theta) & r(\theta) \\ r(\theta) & t(\theta) \end{bmatrix} = \begin{cases} |t| \begin{bmatrix} 1 & i \\ i & 1 \end{bmatrix}, & \theta = \frac{\pi}{2}, \\ |t| \begin{bmatrix} 1 & 1 \\ 1 & 1 \end{bmatrix}, & \theta = 0, \end{cases} \tag{5.5.7}$$

where θ represents the angle between the metaBS local x' axis and the laboratory X axis (intersection of the planes of photon incident and metasurface) (Figure 5.5.1**A**). This way, the mechanical rotation of the metaBS along its surface normal (z' or Z axis), as specified by θ, becomes a degree of freedom (DOF) for the metaBS operation. This is impossible in conventional BS, where the requirement of unitary operation or energy conversation restricts the ϕ_{rt} to the only value $\pi/2$, as we have discussed in previous sections.

Figure 5.5.1**B** shows the schematics of the designed metaBS unit strip cross-section. The three-layer strip is made of 18nm Cr, 65nm MgF_2 and 18nm Cr along z' direction, with 285 nm width (W) and 450 nm period (P) along y' direction. The strip array is sandwiched by two one-mm thick one-inch diameter round NBK7 glass plates, where the gaps are filled with standard index matching oil. The other side of the two glass plates are coated with standard anti-reflection coating. The final metaBS device is symmetric and can be simply handled as a standard one-inch round optics.

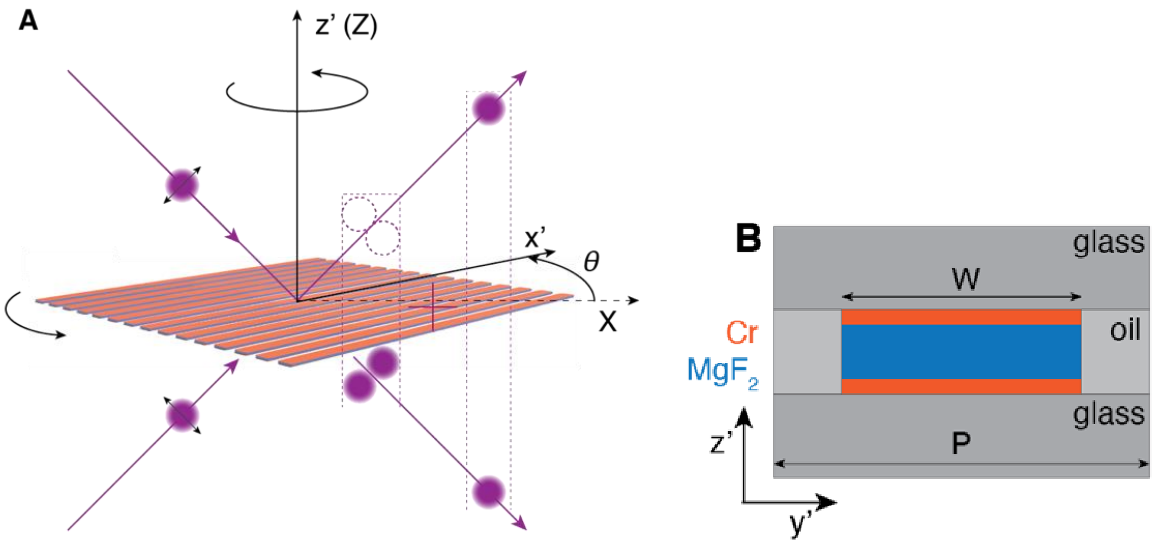

Figure 5.5.1 | The concept and design of metasurface beam-splitter (metaBS) for optical quantum interference.

The theoretical performance of the designed metasurface is list in the Table 5.5.1 below.

Eigen operation	$\|r\|$	$\|t\|$	$2\phi_{rt}/\pi$
$\boldsymbol{\theta = \frac{\pi}{2}}$	0.34	0.35	0.99
$\boldsymbol{\theta = 0}$	0.33	0.34	0.05

Table 5.5.1 | Theoretical performance of the designed metasurface.

5.6 The new degree of freedom in two-photon interference

The metaBS possesses the unique anisotropic phase response that defines two distinct eigen operations as described in last section. Now depending on the rotation angle θ of the metaBS, the output of TPI and the associated effective photon-photon interaction can be dynamically tuned.

When two indistinguishable single photons arrive simultaneously at the unique metaBS in two different input ports, quantum TPI occurs. That is, alternative quantum paths leading to same final configuration will add up constructively or destructively depending on their relative phase. Recall the metaBS operation from last Section 5.5, assuming both incident photons are P waves, the probability $P(1_3, 1_4)$ is the following,

$$P_{(1,1)q}(\theta) = |tt + rr|^2 = |t|^4 \left|1 + \mathrm{Exp}[i(\phi_{photon} + 2\phi_{rt})]\right|^2, \quad (5.6.1)$$

where $\phi_{photon} = 0$ is the phase factor from permutating two photons under bosonic statistics. As indicated by Equation (5.6.1) and following conclusion in last section, the two phase contributions from quantum statistics and metaBS cannot be separated and their sum determines the action of TPI. In other words, as same as the two photons, the metaBS is an essential constitute of TPI. More importantly, the metaBS now enables us to control the effective behavior of the quantum statistics of photons, which is otherwise fundamentally unchangeable. We further derive the second order coherence function $g^{(2)}(\Delta\tau = 0, \theta)$, which is simply $P_{(1,1)q}(\theta)$ normalized by its classical counterpart $P_{(1,1)c}(\theta)$:

$$g^{(2)}(\Delta\tau = 0, \theta) = \frac{P_q(1,1)}{P_c(1,1)} = \frac{4|t|^4 \cos^2\theta}{2|t|^4} = 2\cos^2\theta, \quad (5.6.2)$$

where $\Delta\tau$ is the delay between two incident photons. It is clear from Equation (5.6.1) and Equation (5.6.2) that the rotational θ DOF at metaBS gives birth to a new DOF in TPI at metaBS. Specifically, the $g^{(2)}(\Delta\tau = 0)$ can continuously vary from 0 to 2. In stark contrast, the $g^{(2)}(\Delta\tau = 0)$ would remain a single value 0 in the original TPI experiment.

5.7 Conclusion and outlook

In this chapter, we have proposed, designed and analyzed the metasurface beam-splitter, which can enable a new degree of freedom in quantum two-photon interference through its mechanical rotation. In next chapter, we will continue to present the fabrication of such metasurface and the two-photon interference experiments.

6 Experimental two-photon interference at metasurface beam-splitter

6.1 Introduction

Photonic quantum information processing critically relies on two-photon quantum interference at beam-splitter that provides an indispensable effective photon-photon interaction. However, desirable control of such interaction is limited by the bosonic nature of photons and the restricted unitary operation of conventional beam-splitter.

Using the metasurface beam-splitter (metaBS) developed in last chapter, for the first time, we show that the metaBS rotation can enable a new degree of freedom (DOF) in optical quantum interference, well beyond what is possible conventionally. We experimentally demonstrate that the output of TPI at a metaBS can be dynamically tuned to mimic boson-like bunching state, fermion-like split state, or their arbitrary intermediate anyon-like state, regardless of the intrinsic bosonic nature of photons. Meanwhile, the output state can be changed from entangled to disentangled. Consequently, the effective photon-photon interaction at metaBS can be manipulated at will from attractive to repulsive. This novel quantum phenomenon and functionality is achieved by breaking the unitary operation with loss in a nontrivial way and utilizing the tailored anisotropic phase responses at metaBS. In this way, the metaBS not only introduces new quantum paths and their interferences, but also enables two distinct eigen operations such that the rotation DOF of metaBS along its surface normal gives birth to the emergent DOF in TPI. Such capability is rooted in the metaBS itself, without extra requirements of entanglement or specially selected states. More importantly, the metaBS can be controlled independently and locally, a distinct advantage over previous approaches.

Our metaBS opens new regime for optical quantum interference and effective photon-photon interaction, which could lay the groundwork for innovative quantum computation and quantum communication on a nanophotonic platform.

In last chapter, we discussed the theory of quantum interference and design of the metasurface beam-splitter. This chapter is dedicated to fabrication of the metasurface and the experiments of quantum two-photon interference at such metasurface.

6.2 Fabrication of the metasurface

The metasurface is fabricated by standard nano-fabrication facilities and processes. The fabrication procedure begins with a one-millimeter thick one-inch diameter N-BK7 glass plate with anti-reflection coating on one side (Thorlabs, standard B-coating). On the bare side of the glass plate, an electron beam evaporation system (Solution, CHA) is used to deposit chromium, magnesium fluoride and chromium thin film alternatively with thickness (18/65/18nm). The deposition speeds are 0.4 A/s for chromium and 4.6 A/s for magnesium fluoride. Thickness of thin films deposited by CHA is calibrated with atomic force microscope (NX20, Park Systems) prior to the real sample deposition.

Metasurface structures are patterned by gallium focused ion beam (FIB) milling using a Zeiss ORION NanoFab triple beam helium/neon/gallium ion microscope with current 100pA at 30kV. Pattern files generated using MATLAB were loaded as bitmaps into NanoPatterning and Visualized Engine (NPVE) software from Fibics Inc. The patterned structure is imaged by the helium ion beam (1-2 pA, 25 keV). The patterned area is typically 40 um by 40 um.

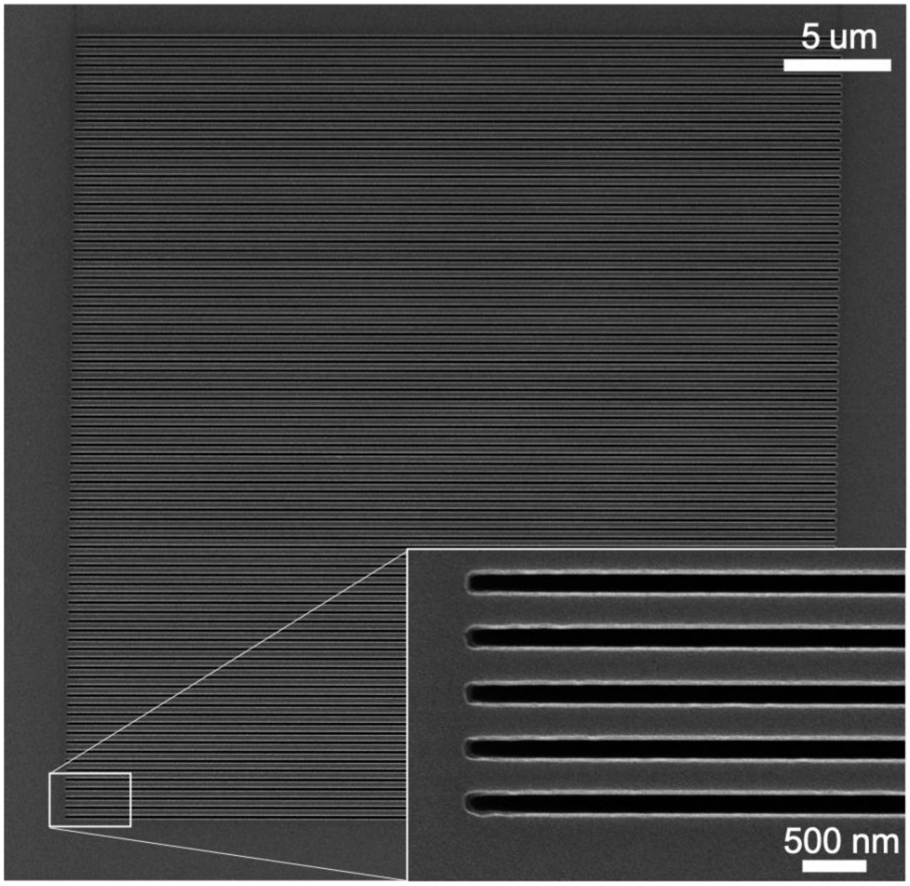

Figure 6.2.1 | Top view scanning helium ion microscope image of a typical metaBS device.

Figure 6.2.1 shows the top view scanning helium ion microscope image of a typical metaBS device after patterning. The grey regions are the three-layer strips while the black regions are the milled trenches.

Finally, the whole metaBS layers are sealed by another 1 mm thick NBK7 glass plates on top with gaps filled by standard index matching oil. Thus, the final metaBS device is symmetric and can be simply handled as a standard one-inch round optics.

6.3 The experiment setup

Figure 6.3.1 below shows the simplified schematic of the experiment setup. Degenerate photon pairs at 710 nm wavelength are produced in spontaneous parametric down conversion from a BBO crystal with type II phase matching. The two photons are then coupled to the two-photon interferometer through single mode fibers. The polarization of each photon is controlled before incident onto the metaBS. The photons incident angle is small (~7 degree). A tunable delay is introduced into one of the incident photons. Finally, the output photons from metaBS are collected by two single-photon counting modules (SPCMs) for coincidence counts measurements.

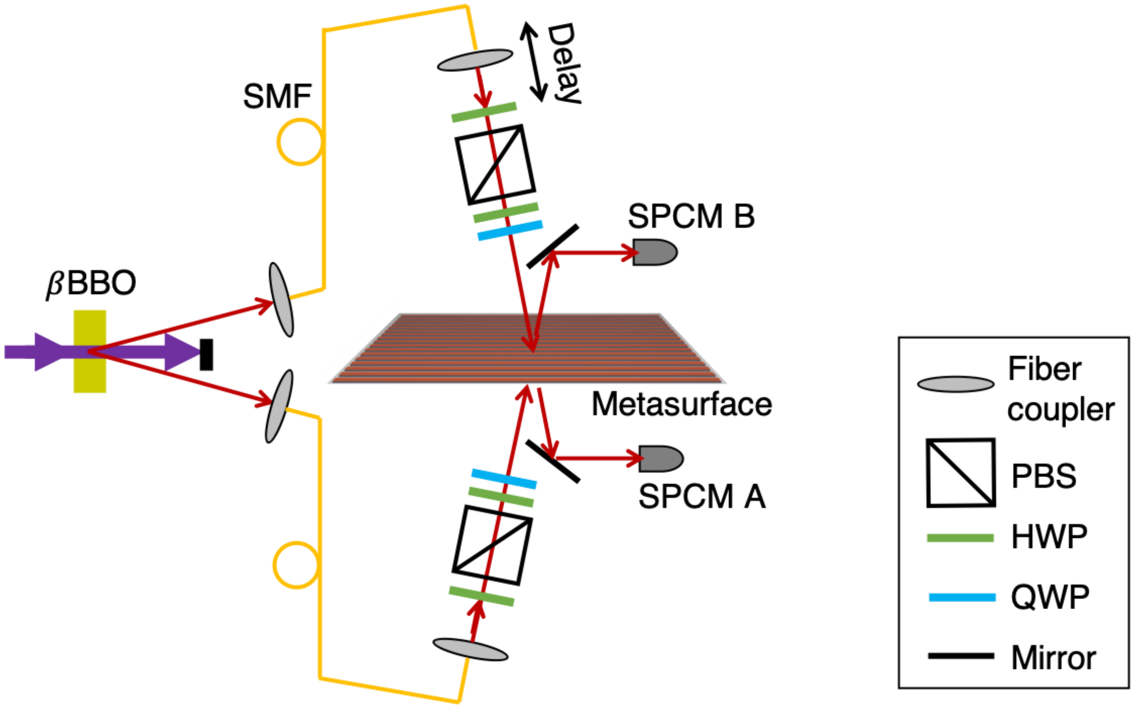

Figure 6.3.1 | The simplified schematics of the experiment setup.

The full experiment layout is shown in the Figure 6.3.2 below, where supporting optics for imaging and alignment are not shown.

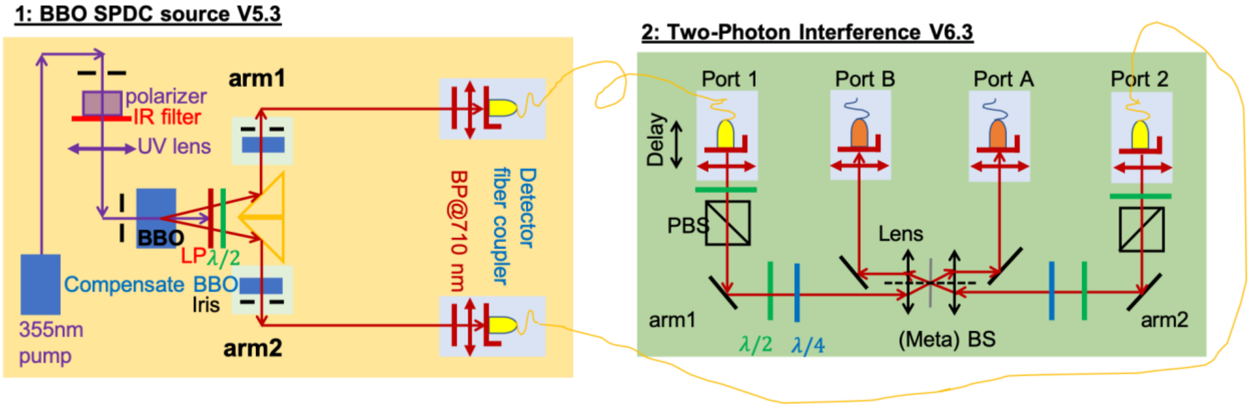

Figure 6.3.2 | The full layout of the experiment setup, without showing imaging and alignment systems.

We can use the same interferometer setup for classical Mach-Zehnder interference and reflection and transmission measurement. This is done by simply replacing the two-photon source by a 710 nm laser beam plus a 50:50 beam-splitter and replacing the two SPCM by two simple silicon photon detectors.

6.4 Characterization of the metasurface

The metaBS phase response ϕ_{rt} can be measured by laser Mach-Zehnder interferometer. The 710 nm laser beam first passes through a lossless conventional 50:50 beam splitter (or a 50:50 fiber coupler). Then the two split beams are directed into the two-photon interferometer port 1 and port 2 (Figure 6.3.2 right). Finally, the two intensities of the two output ports A and B are recorded by Si photon detectors as a function of the delay of port 1.

Assume the metaBS is symmetric and balanced and follow the definitions in Section 5.5, the intensities at output port A and port B can be written as

$$I_A = I_0\left(|r_1|^2|r|^2 + |t_1|^2|t|^2 + 2|r_1 r t_1 t|\cos\left(\phi_{1rt} + \phi_{rt} - \phi_{delay}\right)\right) \tag{6.4.1}$$

and

$$I_B = I_0\big(|t_1|^2|r|^2 + |r_1|^2|t|^2 + 2|r_1 r t_1 t|\cos(\phi_{1rt} - \phi_{rt} - \phi_{delay})\big) \tag{6.4.2}$$

where I_0 is the laser intensity before the first 50:50 BS, r_1 (t_1) and ϕ_{1rt} are the reflection (transmission) coefficient and phase difference of the first 50:50 BS, and ϕ_{delay} is the phase delay from delaying port 1.

Although we can determine the value of ϕ_{rt} from fitting the measured data of intensities I_A and I_B as a function of delay ϕ_{delay} using Equation (6.4.1) and Equation (6.4.2), it is more robust to obtain ϕ_{rt} by fitting the correlations (i.e. parametric equation) between I_A and I_B. Because the parametric equation from correlation is immune to any random phase fluctuations in the interferometer. From Equation (6.4.1) and Equation (6.4.2), we get

$$\begin{aligned} &I_A^2(|r|^2|t|^2) + I_B^2(|r|^2|t|^2) + I_A I_B(-2|r|^2|t|^2\cos(2\phi_{rt})) \\ &+dI_A + eI_B + f \\ &= 0. \end{aligned} \tag{6.4.3}$$

The correlations are in general ellipse shape and can be fitted by the parametric equation

$$aI_A^2 + bI_B^2 + cI_A I_B + dI_A + eI_B + f = 0 \tag{6.4.4}$$

where a, b, c, d, e and f are the coefficients. By comparing Equation (6.4.3)(6.4.1) and Equation (6.4.4), the phase response of the metaBS can be determined by the obtained fitting parameters through

$$2\phi_{rt} = \cos^{-1}\left(\frac{-c}{2\sqrt{ab}}\right). \tag{6.4.5}$$

We have verified that Equation (6.4.5) still holds even if the metaBS is unbalanced and asymmetric. In this case,

$$\phi_{rt} + \phi'_{rt} = \cos^{-1}\left(\frac{-c}{2\sqrt{ab}}\right), \tag{6.4.6}$$

where ϕ_{rt} and ϕ'_{rt} are the phase differences viewed from the two sides of the metaBS, respectively. Only their summation can be determined, and their relative values cannot be distinguished. Actually, in the quantum two-photon interference, it is also this summation rather than their individual values that determines the quantum action. We plot in Figure 6.4.1 below the intensity correlation of the two output ports at conditions of $\theta = \pi/2$ and $\theta = 0$, respectively. The extracted $2\phi_{rt}$ (or $\phi_{rt} + \phi'_{rt}$) from the fittings are summarized in the Table 6.4.1 below.

To measure $|r|$ ($|t|$), we simply use only one of the input ports in the two-photon interferometer and monitor the intensity at two output ports. In reality, the metaBS is always slightly unbalanced and asymmetric, thus we use the averaged values from its two sides. The measured average values are also summarized in the same table. The measurement results agree well with the design values as list in Table 5.5.1.

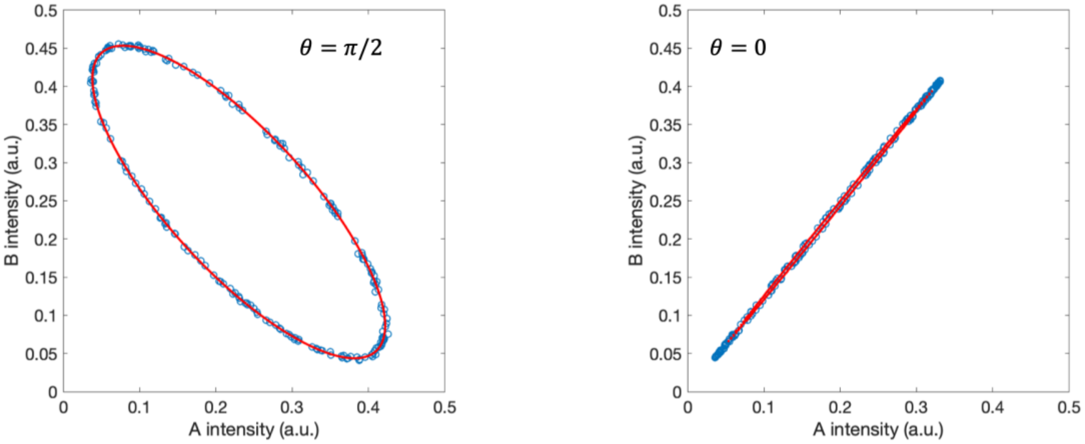

Figure 6.4.1 | Intensity correlation of classical Mach-Zehnder interferometer and their ellipse fitting curves.

Measurement condition	$\boldsymbol{\lvert r \rvert}$	$\boldsymbol{\lvert t \rvert}$	$\boldsymbol{2\phi_{rt}/\pi}$ (or $\boldsymbol{(\phi_{rt} + \phi'_{rt})/\pi}$)
$\boldsymbol{\theta = \frac{\pi}{2}}$	0.336	0.345	0.79
$\boldsymbol{\theta = 0}$	0.305	0.324	0.01

Table 6.4.1 | Summary of measured metaBS parameters.

6.5 Realization of the new rotation degree of freedom

With the experimental setup and characterized metaBS, we are readily to observe the two-photon interference at metaBS. To begin with, we exam the eigen operations. Specifically, at $\theta = \pi/2$, the eigen operation $\phi_{rt} = \pi/2$ at metaBS leads to a completely destructive addition for detecting two photons at separate output ports, resulting in vanishing $P_{(1,1)q}$ and $g^{(2)}(\Delta\tau = 0)$ (Figure 6.5.1A). As in the original HOM effect, the two photons always bunch together, which was attributed to the bosonic statistics of photons. Meanwhile, it produces an effective attractive interaction between the otherwise noninteracting photons. The measured $g^{(2)}(\Delta\tau)$ shows a clear dip about 0.35 at $\Delta\tau = 0$, where a dip below 0.5 is an ambiguous evidence of pure quantum effect (Figure 6.5.1B). In contrast, at $\theta = 0$, the other eigen operation $\phi_{rt} = 0$ at metaBS gives rise to a completely constructive addition for detecting two photons at separate output ports, forming doubled $P_{(1,1)q}$ and $g^{(2)}(\Delta\tau = 0)$ (Figure 6.5.1E). In this case, the two photons always split, which assembles fermionic statistics and produces an effective repulsive interaction between the two photons. The measured $g^{(2)}(\Delta\tau)$ shows a clear peak about 1.71 at $\Delta\tau = 0$, where a peak above 1.5 ambiguously proves the pure quantum effect (Figure 6.5.1F). At $\theta = \pi/4$, the two eigen operations equally superpose (Figure 6.5.1C) and the flat $g^{(2)}(\Delta\tau)$ (Figure 6.5.1D) minics anyonic statistics (*115*, *121*) and must be distinguished from a trivial vanishing TPI of two classical particles obeying Bolzman statistics. The circles in (**D, E, F**) are the measured data with error bars (smaller than the circles) calculated assuming Poisson distribution of event detection, and the solid curves are their fittings.

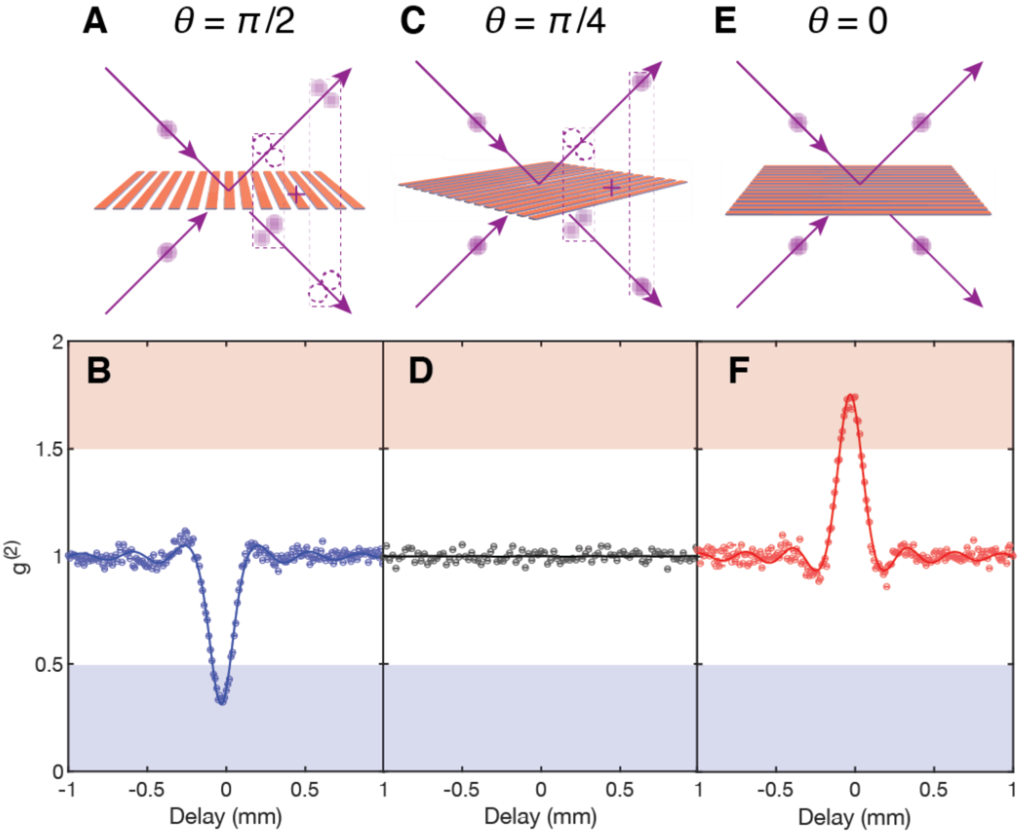

Figure 6.5.1 | Characteristic two-photon interference at the metaBS.

The power from the emergent DOF θ goes beyond the three special cases discussed above; it can take any value and control at will the TPI and the effective photon-photon interaction. Figure 6.5.2 below shows $g^{(2)}(\Delta\tau = 0, \theta)$ as a function of the metaBS rotation angle θ. As θ continuously varying from $-\pi/2$ to $\pi/2$, $g^{(2)}(\Delta\tau = 0, \theta)$ value changes continuously from 0.35 to 1.71, mimicking the continuous and arbitrary transition from boson-like to anyon-like to fermion-like quantum statistics. That is, the output changes from bunching state to intermediate state to split state. As a result, the effective photon-photon interaction evolves from attractive to neutral to repulsive. Clearly, θ represents a new quantum DOF for optical quantum interference. We emphasize that the generalized TPI at any angle θ other than 0 or $\pi/2$ is a superposition of the two eigen cases plus additional terms, with their coefficients determined by the θ. The grey curves are catenated from 61 $g^{(2)}(\Delta\tau,\theta)$ curves at each θ value, from which the main circles data points are extracted. The mimicked quantum statistics here are different from previous approaches using entanglement since other unmeasured configurations have different probabilities (Table 5.4.1).

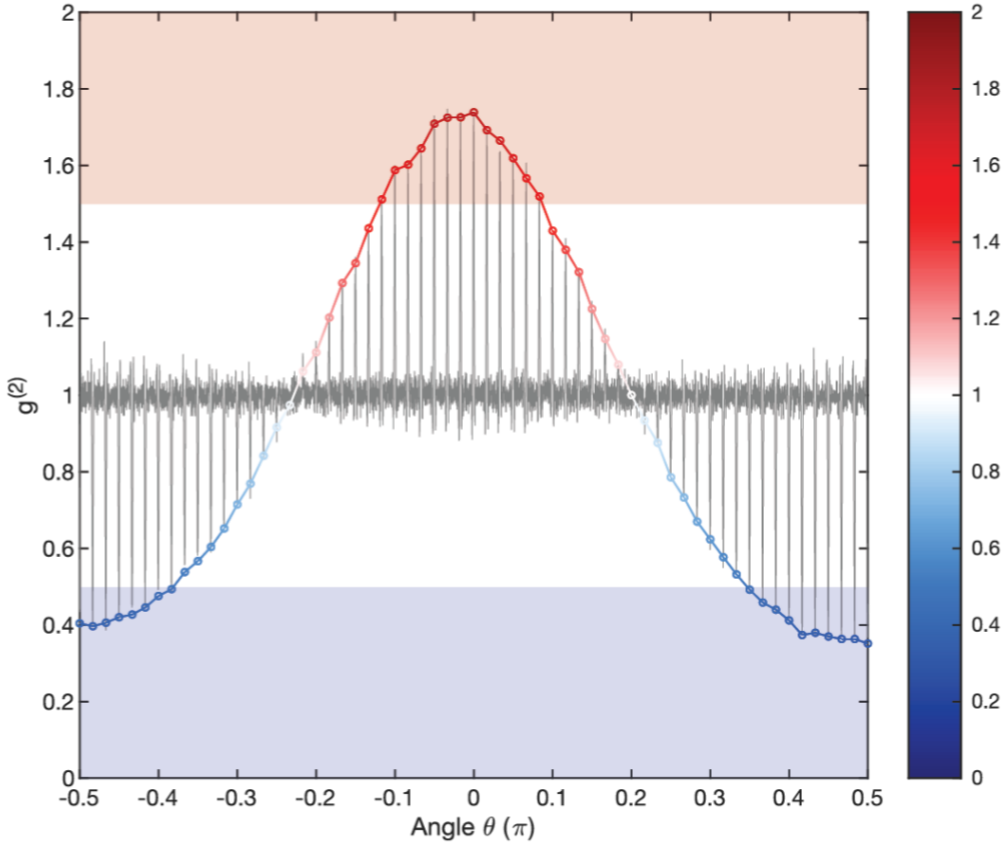

Figure 6.5.2 | The metaBS rotation degree of freedom (DOF) in two-photon interference (TPI).

6.6 Generalization to arbitrary polarizations

So far, we have fixed the polarization of two photons as P waves, but new quantum operation enabled by the metaBS can be readily generalized to any photon polarizations. Figure 6.6.1**A** shows the schematics of the measurement where the metaBS is fixed at $\theta = 0$, while the polarization states of the two incident photons are independently controlled. Figure 6.6.1**B** shows the Bloch sphere representation of the polarization state where the P (S) wave is defined as the H (V) state.

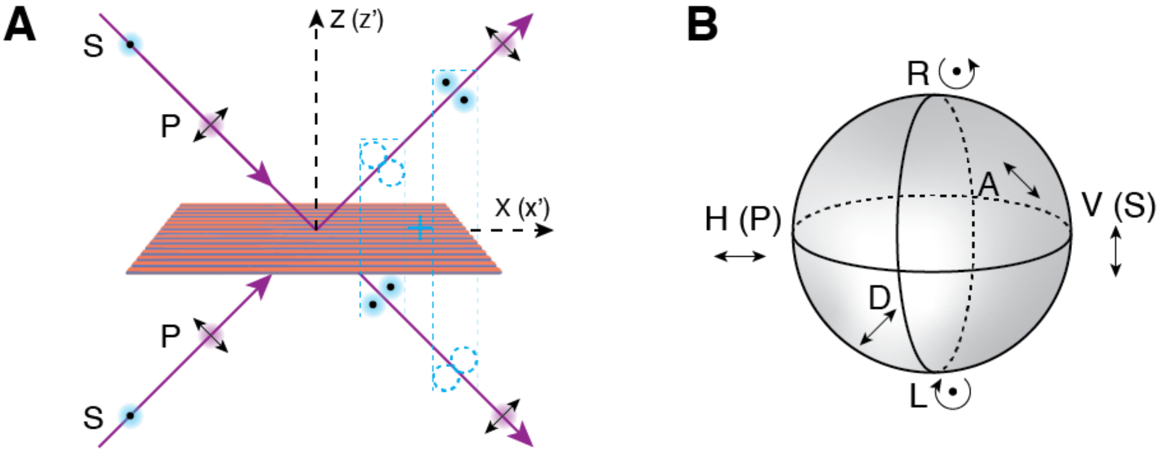

Figure 6.6.1 | The concept of generalized TPI at metaBS for various photon polarizations.

To see that, we measure quantum TPI with independently controlled photon polarizations while keeping the metaBS still at $\theta = 0$. This allows us to map $g^{(2)}(\Delta\tau = 0, p1, p2)$ as a function of the two photons polarizations $p1$ and $p2$ (Figure 6.6.2). The two-photon interference shows a rich texture ranging from 0.35 to 1.71. Such rich texture is never observed before. $g^{(2)}(\Delta\tau = 0, p1, p2)$ has a maximum value greater than 1.5 in the center when both photons are H polarized (P wave) corresponding to the $\theta = 0$ eigen operation of metaBS and then gradually decrease to less than 0.5 in the four corners where both photons were V polarized (S wave) corresponding to the $\theta = \pi/2$ eigen operation. We emphasis the physical meaning of the two sets of white regions are different: the two diagonal white regions (marked by gray dashed lines) correspond to no interference when the two photons have orthogonal polarization; whereas the two anti-diagonal white regions (marked by red dash-dot lines) correspond to a balanced superpositions of the two opposite eigen-operation interferences.

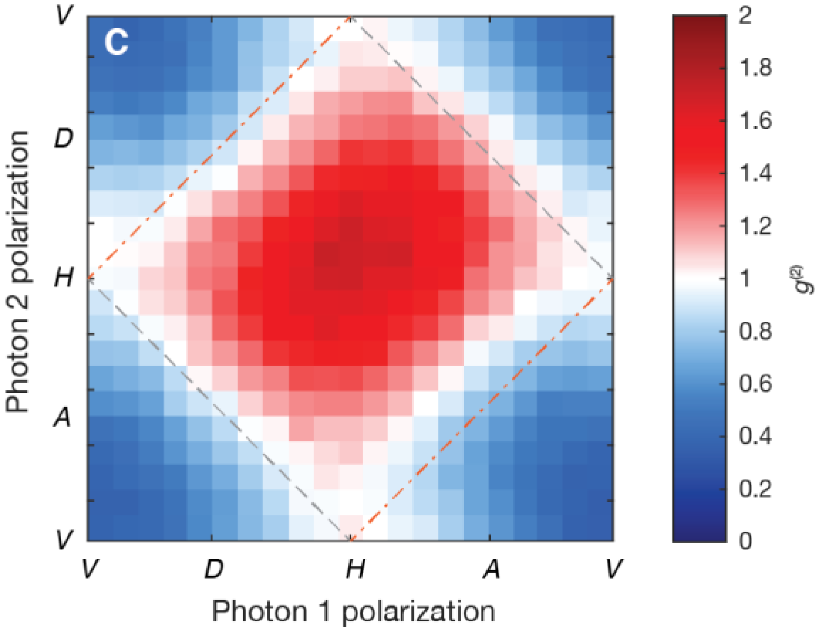

Figure 6.6.2 | The generalized TPI at metaBS with arbitrary linearly polarized photons.

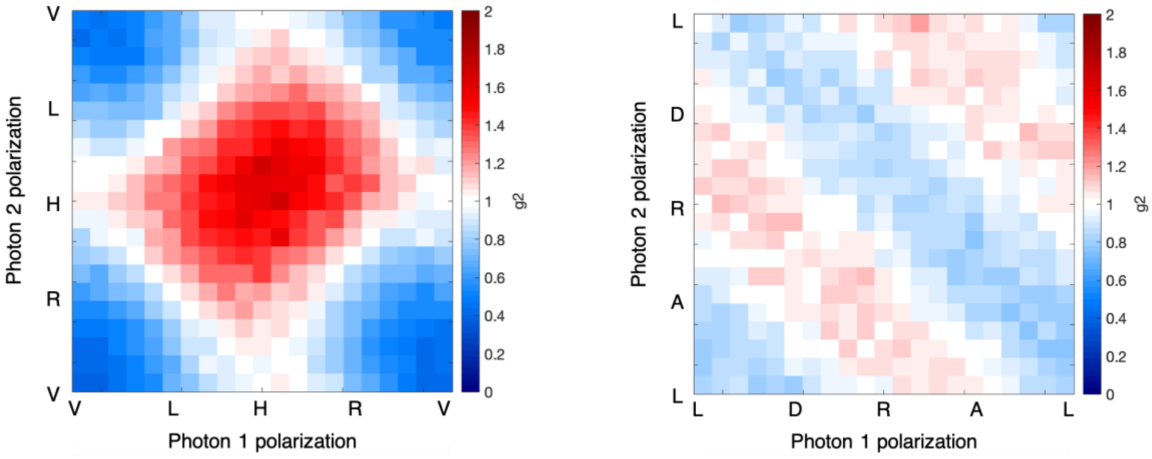

Figure 6.6.3 | The generalized TPI at metaBS along other circles on the Bloch sphere.

The map in Figure 6.6.2 involves the polarization states along the equator of the Bloch sphere. We also measure the map $g^{(2)}(\Delta\tau = 0, p1, p2)$ along the other two representative circles containing circular polarizations on the Bloch sphere, as shown in Figure 6.6.3. Note that the left map assembles the map in Figure 6.6.2, since it also includes the two eigen operations. In contrast, the right map in

Figure 6.6.3 is different in that it does not includes the eigen operations. Therefore, all the $g^{(2)}$ is essential 1, due to either orthogonal polarizations or balanced superstition of opposite eigen operations.

To gain an overview picture of TPI at metaBS with all possible photon polarizations, we further measure $g^{(2)}(\Delta\tau = 0, p1, p2)$ values as the two photons polarizations are chosen from their Bloch sphere's six representative points, that is, H, V, D, A, L and R (Figure 6.6.4). This represents a variety of quantum interference at metaBS and their superpositions, as well as no interference when photon states are orthogonal.

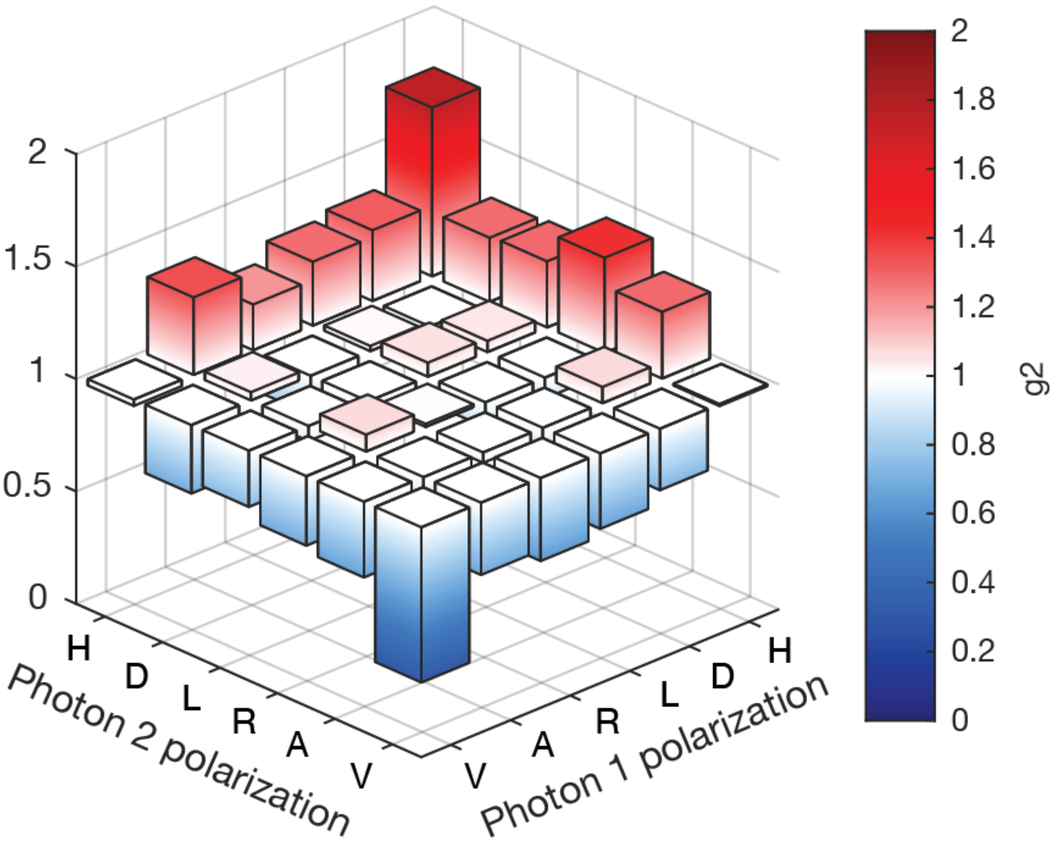

Figure 6.6.4 | The generalized TPI at metaBS for six characteristic photon polarizations.

6.7 Fabrication reliability of the metaBS operation

To further verify the reliability of our metaBS design and fabrication, we fabricated another set of five control metaBSs with varying strip width at a step of 12.5nm around the one presented in previous sections. We then measure the TPI of the two eigen operations at each of those five metaBS. The results show clear trend of varying $g^{(2)}(\Delta\tau = 0)$ values crossing the quantum limits (Figure 6.7.1).

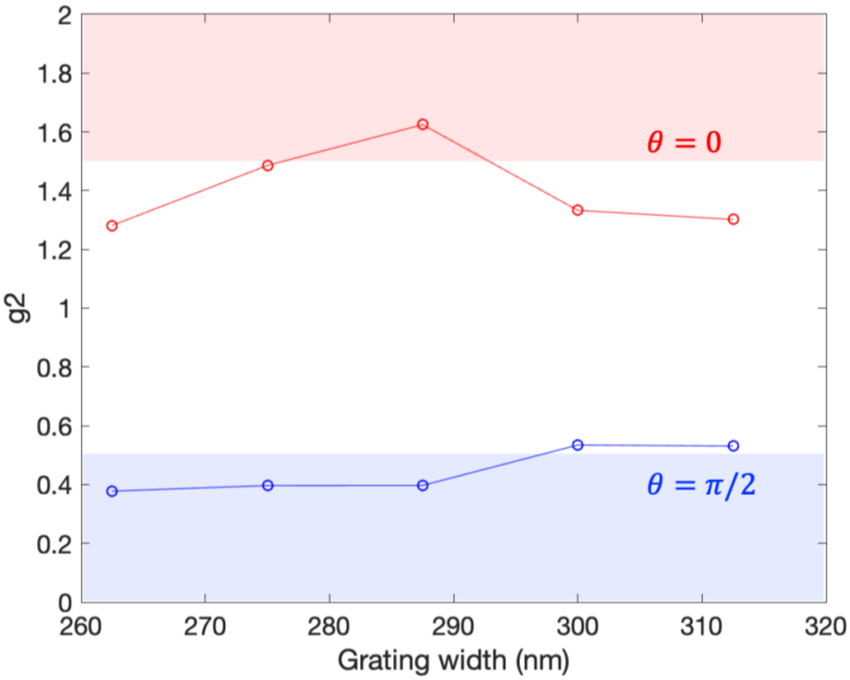

Figure 6.7.1 | TPI at five control metaBSs with varying structure.

6.8 Conclusion and outlook

To conclude, we have demonstrated the first metaBS that brings new quantum operation instead of simply integrating conventional optics. Specifically, our metasurface enables a new rotation DOF in optical quantum interference. Consequently, the two photons behave either boson-like or fermion-like or their arbitrary superpositional anyon-like. Meanwhile, the output state can be controlled to be entangled or disentangled, and the effective photon-photon interaction can be manipulated to be attractive or repulsive. Our work shows the power of metasurface to enable emergent quantum technology.

We note that the full control power of metasurface on electromagnetic wave has not been exploited, and we anticipate that more new quantum operations can be enabled by utilizing more control knobs of metasurface such as spatially temporally gradient or varying responses, as well as controls involving more DOF of photons for instance the angular momentum.

Another direction is scaling up the quantum system. A few of such metaBSs in a large-scale optical network could dramatically change the quantum functionality, in analogy to the tremendous effects created by a few dopants in Si crystal. With metasurface, quantum optical network involving more photons could bring innovative quantum algorithms and quantum computing models.

Remark: Chapter 5 and Chapter 6 include co-authored materials from Quanwei Li, et. al. " Enabling a new dimension in optical quantum interference by metasurface beam-splitter (in preparation)"

Bibliography

1. L. Mandel, E. Wolf, Optical Coherence and Quantum Optics. *Cambridge Core* (1995), , doi:10.1017/CBO9781139644105.

2. M. A. Nielsen, I. L. Chuang, *Quantum computation and quantum information* (Cambridge University Press, Cambridge ; New York, 10th anniversary ed., 2010).

3. J. L. O'Brien, A. Furusawa, J. Vučković, Photonic quantum technologies. *Nature Photonics*. **3**, 687–695 (2009).

4. C. H. Bennett, G. Brassard, Quantum cryptography: Public key distribution and coin tossing. *Proceedings of IEEE International Conference on Computers, Systems and Signal Processing*. **175**, 8 (1984).

5. H. J. Kimble, The quantum internet. *Nature*. **453**, 1023–1030 (2008).

6. J. L. O'Brien, Optical Quantum Computing. *Science*. **318**, 1567–1570 (2007).

7. E. Knill, R. Laflamme, G. J. Milburn, A scheme for efficient quantum computation with linear optics. *nature*. **409**, 46–52 (2001).

8. I. Aharonovich, D. Englund, M. Toth, Solid-state single-photon emitters. *Nat Photon*. **10**, 631–641 (2016).

9. D. E. Chang, V. Vuletić, M. D. Lukin, Quantum nonlinear optics — photon by photon. *Nature Photonics*. **8**, 685–694 (2014).

10. J. Carolan, C. Harrold, C. Sparrow, E. Martín-López, N. J. Russell, J. W. Silverstone, P. J. Shadbolt, N. Matsuda, M. Oguma, M. Itoh, G. D. Marshall, M. G. Thompson, J. C. F. Matthews, T. Hashimoto, J. L. O'Brien, A. Laing, Universal linear optics. *Science*. **349**, 711–716 (2015).

11. Charles Santori, David Fattal, Yoshihisa Yamamoto, *Single-photon devices and applications* (Wiley-VCH, 2010).

12. A. K. Geim, K. S. Novoselov, The rise of graphene. *Nature Materials*. **6**, nmat1849 (2007).

13. F. Xia, H. Wang, D. Xiao, M. Dubey, A. Ramasubramaniam, Two-dimensional material nanophotonics. *Nat Photon*. **8**, 899–907 (2014).

14. A. K. Geim, I. V. Grigorieva, Van der Waals heterostructures. *Nature*. **499**, 419–425 (2013).

15. R. S. Sundaram, M. Engel, A. Lombardo, R. Krupke, A. C. Ferrari, Ph. Avouris, M. Steiner, Electroluminescence in Single Layer MoS2. *Nano Lett.* **13**, 1416–1421 (2013).

16. Y. Ye, H. Zhu, X. Zhang, X. Chen, X. Ni, X. Lu, Y. Wang, Z. J. Wong, Monolayer excitonic laser. *Nature Photonics.* **9**, 733 (2015).

17. M. Liu, B. Geng, E. Ulin-Avila, F. Wang, L. Ju, T. Zentgraf, X. Zhang, X. Yin, A graphene-based broadband optical modulator. *Nature.* **474**, 64 (2011).

18. M. Koperski, K. Nogajewski, A. Arora, V. Cherkez, P. Mallet, J.-Y. Veuillen, J. Marcus, P. Kossacki, M. Potemski, Single photon emitters in exfoliated WSe2 structures. *Nat Nano.* **10**, 503–506 (2015).

19. P. Tonndorf, R. Schmidt, R. Schneider, J. Kern, M. Buscema, G. A. Steele, A. Castellanos-Gomez, H. S. J. van der Zant, S. Michaelis de Vasconcellos, R. Bratschitsch, Single-photon emission from localized excitons in an atomically thin semiconductor. *Optica.* **2**, 347 (2015).

20. A. Srivastava, M. Sidler, A. V. Allain, D. S. Lembke, A. Kis, A. Imamoğlu, Optically active quantum dots in monolayer WSe2. *Nat Nano.* **10**, 491–496 (2015).

21. Y.-M. He, G. Clark, J. R. Schaibley, Y. He, M.-C. Chen, Y.-J. Wei, X. Ding, Q. Zhang, W. Yao, X. Xu, C.-Y. Lu, J.-W. Pan, Single quantum emitters in monolayer semiconductors. *Nat Nano.* **10**, 497–502 (2015).

22. C. Chakraborty, L. Kinnischtzke, K. M. Goodfellow, R. Beams, A. N. Vamivakas, Voltage-controlled quantum light from an atomically thin semiconductor. *Nat Nano.* **10**, 507–511 (2015).

23. C. Palacios-Berraquero, M. Barbone, D. M. Kara, X. Chen, I. Goykhman, D. Yoon, A. K. Ott, J. Beitner, K. Watanabe, T. Taniguchi, A. C. Ferrari, M. Atatüre, Atomically thin quantum light-emitting diodes. *Nature Communications.* **7**, ncomms12978 (2016).

24. T. T. Tran, K. Bray, M. J. Ford, M. Toth, I. Aharonovich, Quantum emission from hexagonal boron nitride monolayers. *Nat Nano.* **11**, 37–41 (2016).

25. A. Pospischil, M. Humer, M. M. Furchi, D. Bachmann, R. Guider, T. Fromherz, T. Mueller, *Nature Photonics*, in press, doi:10.1038/nphoton.2013.240.

26. C. Gerry, P. Knight, Introductory Quantum Optics. *Cambridge Core* (2004), , doi:10.1017/CBO9780511791239.

27. M. Koperski, K. Nogajewski, M. Potemski, Single photon emitters in boron nitride: More than a supplementary material. *Optics Communications.* **411**, 158–165 (2018).

28. R. Geick, C. H. Perry, G. Rupprecht, Normal Modes in Hexagonal Boron Nitride. *Phys. Rev.* **146**, 543–547 (1966).

29. S. Aaronson, A. Arkhipov, in *Proceedings of the Forty-third Annual ACM Symposium on Theory of Computing* (ACM, New York, NY, USA, 2011; http://doi.acm.org/10.1145/1993636.1993682), *STOC '11*, pp. 333–342.

30. I. Aharonovich, D. Englund, M. Toth, Solid-state single-photon emitters. *Nature Photon.* **10**, 631–641 (2016).

31. I. Aharonovich, A. D. Greentree, S. Prawer, Diamond photonics. *Nature Photon.* **5**, 397–405 (2011).

32. R.-J. Shiue, Y. Gao, Y. Wang, C. Peng, A. D. Robertson, D. K. Efetov, S. Assefa, F. H. L. Koppens, J. Hone, D. Englund, High-Responsivity Graphene–Boron Nitride Photodetector and Autocorrelator in a Silicon Photonic Integrated Circuit. *Nano Lett.* **15**, 7288–7293 (2015).

33. R. B. Patel, A. J. Bennett, I. Farrer, C. A. Nicoll, D. A. Ritchie, A. J. Shields, Two-photon interference of the emission from electrically tunable remote quantum dots. *Nature Photon.* **4**, 632–635 (2010).

34. N. Somaschi, V. Giesz, L. D. Santis, J. C. Loredo, M. P. Almeida, G. Hornecker, S. L. Portalupi, T. Grange, C. Antón, J. Demory, C. Gómez, I. Sagnes, N. D. Lanzillotti-Kimura, A. Lemaítre, A. Auffeves, A. G. White, L. Lanco, P. Senellart, Near-optimal single-photon sources in the solid state. *Nat Photon.* **10**, 340–345 (2016).

35. J. Bylander, I. Robert-Philip, I. Abram, Interference and correlation of two independent photons. *Eur. Phys. J. D.* **22**, 295–301 (2003).

36. T. Grange, G. Hornecker, D. Hunger, J.-P. Poizat, J.-M. Gérard, P. Senellart, A. Auffèves, Cavity-Funneled Generation of Indistinguishable Single Photons from Strongly Dissipative Quantum Emitters. *Physical Review Letters.* **114**, 193601 (2015).

37. G. M. Akselrod, C. Argyropoulos, T. B. Hoang, C. Ciracì, C. Fang, J. Huang, D. R. Smith, M. H. Mikkelsen, Probing the mechanisms of large Purcell enhancement in plasmonic nanoantennas. *Nature Photonics.* **8**, 835–840 (2014).

38. N. Q. Dots, Quantum-Confined Stark Effect in Single CdSe. *Science.* **278**, 2114–2114 (1997).

39. J. P. Reithmaier, G. Sęk, A. Löffler, C. Hofmann, S. Kuhn, S. Reitzenstein, L. V. Keldysh, V. D. Kulakovskii, T. L. Reinecke, A. Forchel, Strong coupling in a single quantum dot–semiconductor microcavity system. *Nature.* **432**, 197–200 (2004).

40. E. Flagg, A. Muller, S. Polyakov, A. Ling, A. Migdall, G. Solomon, Interference of Single Photons from Two Separate Semiconductor Quantum Dots. *Physical Review Letters.* **104** (2010), doi:10.1103/PhysRevLett.104.137401.

41. G. Grosso, H. Moon, B. Lienhard, S. Ali, D. K. Efetov, M. M. Furchi, P. Jarillo-Herrero, M. J. Ford, I. Aharonovich, D. Englund, Tunable and high-purity room temperature single-photon emission from atomic defects in hexagonal boron nitride. *Nature Communications*. **8**, 705 (2017).

42. R. M. Stevenson, R. J. Young, P. Atkinson, K. Cooper, D. A. Ritchie, A. J. Shields, A semiconductor source of triggered entangled photon pairs. *Nature*. **439**, 179–182 (2006).

43. C. Chakraborty, K. M. Goodfellow, S. Dhara, A. Yoshimura, V. Meunier, A. N. Vamivakas, Quantum-Confined Stark Effect of Individual Defects in a van der Waals Heterostructure. *Nano Lett.* **17**, 2253–2258 (2017).

44. Ph. Tamarat, T. Gaebel, J. R. Rabeau, M. Khan, A. D. Greentree, H. Wilson, L. C. L. Hollenberg, S. Prawer, P. Hemmer, F. Jelezko, J. Wrachtrup, Stark Shift Control of Single Optical Centers in Diamond. *Phys. Rev. Lett.* **97**, 083002 (2006).

45. L. C. Bassett, F. J. Heremans, C. G. Yale, B. B. Buckley, D. D. Awschalom, Electrical Tuning of Single Nitrogen-Vacancy Center Optical Transitions Enhanced by Photoinduced Fields. *Phys. Rev. Lett.* **107**, 266403 (2011).

46. H. Bernien, L. Childress, L. Robledo, M. Markham, D. Twitchen, R. Hanson, Two-Photon Quantum Interference from Separate Nitrogen Vacancy Centers in Diamond. *Physical Review Letters*. **108** (2012), doi:10.1103/PhysRevLett.108.043604.

47. A. Sipahigil, M. L. Goldman, E. Togan, Y. Chu, M. Markham, D. J. Twitchen, A. S. Zibrov, A. Kubanek, M. D. Lukin, Quantum Interference of Single Photons from Remote Nitrogen-Vacancy Centers in Diamond. *Physical Review Letters*. **108** (2012), doi:10.1103/PhysRevLett.108.143601.

48. R. Lettow, Y. L. A. Rezus, A. Renn, G. Zumofen, E. Ikonen, S. Götzinger, V. Sandoghdar, Quantum Interference of Tunably Indistinguishable Photons from Remote Organic Molecules. *Phys. Rev. Lett.* **104**, 123605 (2010).

49. R. M. Macfarlane, Optical Stark spectroscopy of solids. *Journal of Luminescence*. **125**, 156–174 (2007).

50. Ch. Brunel, Ph. Tamarat, B. Lounis, J. C. Woehl, M. Orrit, Stark Effect on Single Molecules of Dibenzanthanthrene in a Naphthalene Crystal and in a *n*-Hexadecane Shpol'skii Matrix. *The Journal of Physical Chemistry A*. **103**, 2429–2434 (1999).

51. Y. Xia, Q. Li, J. Kim, W. Bao, C. Gong, S. Yang, Y. Wang, X. Zhang, Room-Temperature Giant Stark Effect of Single Photon Emitter in van der Waals Material. *Nano Lett.* **19**, 7100–7105 (2019).

52. H. Deng, Y. Yamamoto, Exciton-polariton Bose-Einstein condensation. *Reviews of Modern Physics*. **82**, 1489–1537 (2010).

53. P. Lodahl, S. Mahmoodian, S. Stobbe, Interfacing single photons and single quantum dots with photonic nanostructures. *Review of Modern Physics*. **87**, 347–400 (2015).

54. H. M. Gibbs, G. Khitrova, S. W. Koch, Exciton-polariton light-semiconductor coupling effects. *Nature Photonics*. **5**, 275–282 (2011).

55. D. Sanvitto, S. Kéna-Cohen, The road towards polaritonic devices. *Nature Materials*. **15**, 1061–1073 (2016).

56. C. Schneider, M. M. Glazov, T. Korn, S. Hö, B. Urbaszek, Two-dimensional semiconductors in the regime of strong light-matter coupling. *Nature Communication*. **9**, 2695 (2018).

57. J. L. Tomaino, A. D. Jameson, Y. Lee, G. Khitrova, H. M. Gibbs, A. C. Klettke, M. Kira, S. W. Koch, Terahertz Excitation of a Coherent Ã -Type Three-Level System of Exciton-Polariton Modes in a Quantum-Well Microcavity. *Physical Review Letters*. **108**, 267402 (2012).

58. N. V. Vitanov, A. A. Rangelov, B. W. Shore, K. Bergmann, Stimulated Raman adiabatic passage in physics, chemistry, and beyond. *Reviews of Modern Physics*. **89**, 015006 (2017).

59. D. D. M. Coles, N. Somaschi, P. Michetti, C. Clark, P. G. Lagoudakis, P. G. Savvidis, D. G. Lidzey, Polariton-mediated energy transfer between organic dyes in a strongly coupled optical microcavity. *Nature materials*. **13**, 712–719 (2014).

60. R. Bose, T. Cai, K. R. Choudhury, G. S. Solomon, E. Waks, All-optical coherent control of vacuum Rabi oscillations. *Nature Photonics*. **8**, 858–864 (2014).

61. J.-M. Ménard, C. Poellmann, M. Porer, U. Leierseder, E. Galopin, A. Lemaître, A. Amo, J. Bloch, R. Huber, Revealing the dark side of a bright exciton-polariton condensate. *Nature communications*. **5**, 4648 (2014).

62. L. Dominici, D. Colas, S. Donati, J. P. Restrepo Cuartas, M. De Giorgi, D. Ballarini, G. Guirales, J. C. López Carreño, A. Bramati, G. Gigli, E. del Valle, F. P. Laussy, D. Sanvitto, Ultrafast Control and Rabi Oscillations of Polaritons. *Physical Review Letters*. **113**, 226401 (2014).

63. W. D. Rice, J. Kono, S. Zybell, S. Winnerl, J. Bhattacharyya, H. Schneider, M. Helm, B. Ewers, A. Chernikov, M. Koch, S. Chatterjee, G. Khitrova, H. M. Gibbs, L. Schneebeli, B. Breddermann, M. Kira, S. W. Koch, Observation of Forbidden Exciton Transitions Mediated by Coulomb Interactions in Photoexcited Semiconductor Quantum Wells. *Physical Review Letters*. **110**, 137404 (2013).

64. J. Xiao, Z. Ye, Y. Wang, H. Zhu, Y. Wang, X. Zhang, Nonlinear optical selection rule based on valley-exciton locking in monolayer WS2. *Light: Science & Applications*. **4**, e366 (2015).

65. D. Xiao, G.-B. Liu, W. Feng, X. Xu, W. Yao, Coupled Spin and Valley Physics in Monolayers of ${\mathrm{MoS}}_{2}$ and Other Group-VI Dichalcogenides. *Phys. Rev. Lett.* **108**, 196802 (2012).

66. X. Liu, T. Galfsky, Z. Sun, F. Xia, E. Lin, Y.-H. Lee, S. Kéna-Cohen, V. M. Menon, Strong light–matter coupling in two-dimensional atomic crystals. *Nature Photonics*. **9**, 30–34 (2015).

67. S. Dufferwiel, S. Schwarz, F. Withers, A. A. P. Trichet, F. Li, M. Sich, O. Del Pozo-Zamudio, C. Clark, A. Nalitov, D. D. Solnyshkov, G. Malpuech, K. S. Novoselov, J. M. Smith, M. S. Skolnick, D. N. Krizhanovskii, A. I. Tartakovskii, Exciton–polaritons in van der Waals heterostructures embedded in tunable microcavities. *Nature Communications*. **6**, 8579 (2015).

68. K. F. Mak, J. Shan, Photonics and optoelectronics of 2D semiconductor transition metal dichalcogenides. *Nature Photonics*. **10**, 216–226 (2016).

69. K. F. Mak, C. Lee, J. Hone, J. Shan, T. F. Heinz, Atomically Thin MoS_{2}: A New Direct-Gap Semiconductor. *Physical Review Letters*. **105**, 136805 (2010).

70. A. Splendiani, L. Sun, Y. Zhang, T. Li, J. Kim, C.-Y. Chim, G. Galli, F. Wang, Emerging Photoluminescence in Monolayer MoS2. *Nano letters*. **10**, 1271–1275 (2010).

71. A. Chernikov, T. C. Berkelbach, H. M. Hill, A. Rigosi, Y. Li, O. B. Aslan, D. R. Reichman, M. S. Hybertsen, T. F. Heinz, Exciton Binding Energy and Nonhydrogenic Rydberg Series in Monolayer WS2. *Physical Review Letters*. **113**, 076802 (2014).

72. Z. Ye, T. Cao, K. O'Brien, H. Zhu, X. Yin, Y. Wang, S. G. Louie, X. Zhang, Probing excitonic dark states in single-layer tungsten disulphide. *Nature*. **513**, 214–218 (2014).

73. T. Cao, G. Wang, W. Han, H. Ye, C. Zhu, J. Shi, Q. Niu, P. Tan, E. Wang, B. Liu, J. Feng, Valley-selective circular dichroism of monolayer molybdenum disulphide. *Nature communications*. **3**, 887 (2012).

74. H. Zeng, J. Dai, W. Yao, D. Xiao, X. Cui, Valley polarization in MoS2 monolayers by optical pumping. *Nature nanotechnology*. **7**, 490–493 (2012).

75. K. F. Mak, K. He, J. Shan, T. F. Heinz, Control of valley polarization in monolayer MoS2 by optical helicity. *Nature nanotechnology*. **7**, 494–498 (2012).

76. Z. Sun, J. Gu, A. Ghazaryan, Z. Shotan, C. R. Considine, M. Dollar, B. Chakraborty, X. Liu, P. Ghaemi, S. Kéna-Cohen, V. M. Menon, Optical control of room-temperature valley polaritons. *Nature Photonics*. **11**, 491–496 (2017).

77. Y.-J. Chen, J. D. Cain, T. K. Stanev, V. P. Dravid, N. P. Stern, Valley-Polarized Exciton-Polaritons in a Monolayer Semiconductor. *Nature Photonics*. **11**, 431–435 (2017).

78. S. Dufferwiel, T. P. Lyons, D. D. Solnyshkov, A. A. P. Trichet, F. Withers, S. Schwarz, G. Malpuech, J. M. Smith, K. S. Novoselov, M. S. Skolnick, D. N. Krizhanovskii, A. I. Tartakovskii, Valley addressable exciton-polaritons in atomically thin semiconductors. *Nature Photonics*. **11**, 497–501 (2017).

79. N. Lundt, S. Stoll, P. Nagler, A. Nalitov, S. Klembt, S. Betzold, J. Goddard, E. Frieling, A. V. Kavokin, C. Schüller, T. Korn, S. Höfling, C. Schneider, Observation of macroscopic valley-polarized monolayer exciton-polaritons at room temperature. *Physical Review B*. **96**, 241403 (2017).

80. G. Wang, X. Marie, I. Gerber, T. Amand, D. Lagarde, L. Bouet, M. Vidal, A. Balocchi, B. Urbaszek, Giant Enhancement of the Optical Second-Harmonic Emission of WSe2 Monolayers by Laser Excitation at Exciton Resonances. *Physical Review Letters*. **114**, 097403 (2015).

81. F. Wang, G. Dukovic, L. E. Brus, T. F. Heinz, The optical resonances in carbon nanotubes arise from excitons. *Science*. **308**, 838–41 (2005).

82. X. Liu, W. Bao, Q. Li, C. Ropp, Y. Wang, X. Zhang, Control of Coherently Coupled Exciton Polaritons in Monolayer Tungsten Disulphide. *Phys. Rev. Lett.* **119**, 027403 (2017).

83. V. Savona, L. C. Andreani, P. Schwendimann, A. Quattropani, QUANTUM WELL EXCITONS IN SEMICONDUCTOR MICROCAVITIES: UNIFIED TREATMENT OF WEAK AND STRONG COUPLING REGIMES. *Solid State Communications*. **93**, 733–739 (1995).

84. X. Liu, W. Bao, Q. Li, C. Ropp, Y. Wang, X. Zhang, Control of coherently coupled exciton-polaritons in monolayer tungsten disulphide. *Physical Review Letters*. **119**, 027403 (2017).

85. B. Zhu, X. Chen, X. Cui, Exciton binding energy of monolayer WS2. *Scientific Reports*. **5** (2015), doi:10.1038/srep09218.

86. K. Lekenta, D. Stephan, K. Nogajewski, M. Potemski, J. Szczytko, M. R. Molas, *arXiv*, in press.

87. K. L. Seyler, J. R. Schaibley, P. Gong, P. Rivera, A. M. Jones, S. Wu, J. Yan, D. G. Mandrus, W. Yao, X. Xu, Electrical control of second-harmonic generation in a WSe2 monolayer transistor. *Nature Nanotechnology*. **10**, 407–411 (2015).

88. J. B. Pendry, Negative Refraction Makes a Perfect Lens. *Physical Review Letters*. **85**, 3966–3969 (2000).

89. R. A. Shelby, Experimental Verification of a Negative Index of Refraction. *Science*. **292**, 77–79 (2001).

90. N. Fang, Sub-Diffraction-Limited Optical Imaging with a Silver Superlens. *Science*. **308**, 534–537 (2005).

91. J. B. Pendry, D. Schurig, D. R. Smith, Controlling Electromagnetic Fields. *Science*. **312**, 1780–1782 (2006).

92. N. Yu, P. Genevet, M. A. Kats, F. Aieta, J.-P. Tetienne, F. Capasso, Z. Gaburro, Light Propagation with Phase Discontinuities: Generalized Laws of Reflection and Refraction. *Science*. **334**, 333–337 (2011).

93. X. Ni, N. K. Emani, A. V. Kildishev, A. Boltasseva, V. M. Shalaev, Broadband Light Bending with Plasmonic Nanoantennas. *Science*. **335**, 427–427 (2012).

94. N. Shitrit, I. Yulevich, E. Maguid, D. Ozeri, D. Veksler, V. Kleiner, E. Hasman, Spin-Optical Metamaterial Route to Spin-Controlled Photonics. *Science*. **340**, 724–726 (2013).

95. D. Lin, P. Fan, E. Hasman, M. L. Brongersma, Dielectric gradient metasurface optical elements. *Science*. **345**, 298–302 (2014).

96. A. Arbabi, Y. Horie, M. Bagheri, A. Faraon, Dielectric metasurfaces for complete control of phase and polarization with subwavelength spatial resolution and high transmission. *Nature Nanotechnology*. **10**, 937–943 (2015).

97. E. Knill, R. Laflamme, G. J. Milburn, A scheme for efficient quantum computation with linear optics. *Nature*. **409**, 46–52 (2001).

98. J. L. O'Brien, A. Furusawa, J. Vučković, Photonic quantum technologies. *Nature Photon.* **3**, 687–695 (2009).

99. A. Aspuru-Guzik, P. Walther, Photonic quantum simulators. *Nature Phys.* **8**, 285–291 (2012).

100. I. A. Walmsley, Quantum optics: Science and technology in a new light. *Science*. **348**, 525–530 (2015).

101. J. Wang, S. Paesani, Y. Ding, R. Santagati, P. Skrzypczyk, A. Salavrakos, J. Tura, R. Augusiak, L. Mančinska, D. Bacco, D. Bonneau, J. W. Silverstone, Q. Gong, A. Acín, K. Rottwitt, L. K. Oxenløwe, J. L. O'Brien, A. Laing, M. G. Thompson, Multidimensional quantum entanglement with large-scale integrated optics. *Science*. **360**, 285–291 (2018).

102. L. M. Procopio, L. A. Rozema, Z. J. Wong, D. R. Hamel, K. O'Brien, X. Zhang, B. Dakić, P. Walther, Single-photon test of hyper-complex quantum theories using a metamaterial. *Nature Communications*. **8** (2017), doi:10.1038/ncomms15044.

103. T. Stav, A. Faerman, E. Maguid, D. Oren, V. Kleiner, E. Hasman, M. Segev, Quantum entanglement of the spin and orbital angular momentum of photons using metamaterials. *Science*. **361**, 1101–1104 (2018).

104. K. Wang, J. G. Titchener, S. S. Kruk, L. Xu, H.-P. Chung, M. Parry, I. I. Kravchenko, Y.-H. Chen, A. S. Solntsev, Y. S. Kivshar, D. N. Neshev, A. A. Sukhorukov, Quantum metasurface for multiphoton interference and state reconstruction. *Science*. **361**, 1104–1108 (2018).

105. P. Georgi, M. Massaro, K.-H. Luo, B. Sain, N. Montaut, H. Herrmann, T. Weiss, G. Li, C. Silberhorn, T. Zentgraf, Metasurface interferometry toward quantum sensors. *Light: Science & Applications*. **8** (2019), doi:10.1038/s41377-019-0182-6.

106. S. Aaronson, A. Arkhipov, in *Proceedings of the Forty-third Annual ACM Symposium on Theory of Computing* (ACM, New York, NY, USA, 2011; http://doi.acm.org/10.1145/1993636.1993682), *STOC '11*, pp. 333–342.

107. J. B. Spring, B. J. Metcalf, P. C. Humphreys, W. S. Kolthammer, X.-M. Jin, M. Barbieri, A. Datta, N. Thomas-Peter, N. K. Langford, D. Kundys, J. C. Gates, B. J. Smith, P. G. R. Smith, I. A. Walmsley, Boson Sampling on a Photonic Chip. *Science*. **339**, 798–801 (2013).

108. H. B. Perets, Y. Lahini, F. Pozzi, M. Sorel, R. Morandotti, Y. Silberberg, Realization of Quantum Walks with Negligible Decoherence in Waveguide Lattices. *Phys. Rev. Lett.* **100**, 170506 (2008).

109. C. K. Hong, Z. Y. Ou, L. Mandel, Measurement of subpicosecond time intervals between two photons by interference. *Physical Review Letters*. **59**, 2044–2046 (1987).

110. R. Loudon, Fermion and boson beam-splitter statistics. *Physical Review A*. **58**, 4904–4909 (1998).

111. A. Zeilinger, General properties of lossless beam splitters in interferometry. *American Journal of Physics*. **49**, 882–883 (1981).

112. P. G. Kwiat, A. M. Steinberg, R. Y. Chiao, Observation of a "'quantum eraser"': A revival of coherence in a two-photon interference experiment. *Physical Review A*. **45**, 7729–7739 (1992).

113. M. Michler, K. Mattle, H. Weinfurter, A. Zeilinger, Interferometric Bell-state analysis. *Physical Review A*. **53**, R1209–R1212 (1996).

114. L. Sansoni, F. Sciarrino, G. Vallone, P. Mataloni, A. Crespi, R. Ramponi, R. Osellame, Two-Particle Bosonic-Fermionic Quantum Walk via Integrated Photonics. *Phys. Rev. Lett.* **108**, 010502 (2012).

115. J. C. F. Matthews, K. Poulios, J. D. A. Meinecke, A. Politi, A. Peruzzo, N. Ismail, K. Wörhoff, M. G. Thompson, J. L. O'Brien, Observing fermionic statistics with photons in arbitrary processes. *Scientific Reports*. **3** (2013), doi:10.1038/srep01539.

116. S. M. Barnett, J. Jeffers, A. Gatti, R. Loudon, Quantum optics of lossy beam splitters. *Physical Review A*. **57**, 2134–2145 (1998).

117. J. Jeffers, Interference and the lossless lossy beam splitter. *Journal of Modern Optics*. **47**, 1819–1824 (2000).

118. H. Defienne, M. Barbieri, I. A. Walmsley, B. J. Smith, S. Gigan, Two-photon quantum walk in a multimode fiber. *Science Advances*. **2**, e1501054 (2016).

119. T. A. W. Wolterink, R. Uppu, G. Ctistis, W. L. Vos, K.-J. Boller, P. W. H. Pinkse, Programmable two-photon quantum interference in 10 3 channels in opaque scattering media. *Physical Review A*. **93** (2016), doi:10.1103/PhysRevA.93.053817.

120. B. Vest, M.-C. Dheur, É. Devaux, A. Baron, E. Rousseau, J.-P. Hugonin, J.-J. Greffet, G. Messin, F. Marquier, Anti-coalescence of bosons on a lossy beam splitter. *Science*. **356**, 1373–1376 (2017).

121. F. Wilczek, Quantum Mechanics of Fractional-Spin Particles. *Phys. Rev. Lett.* **49**, 957–959 (1982).